The Aging of Organic Aerosol in the Atmosphere: Chemical Transformations by Heterogeneous Oxidation

by

Sean Herbert Kessler

B.S. Chemical Engineering, Lehigh University, 2008

Submitted to the Department of Chemical Engineering in Partial Fulfillment of the Requirements for the degree of

DOCTOR OF PHILOSOPHY IN CHEMICAL ENGINEERING

at the

MASSACHUSETTS INSTITUTE OF TECHNOLOGY

June 2013

Signature of Author: _____

Department of Chemical Engineering, May 17, 2013

Certified by: _____

Jesse H. Kroll
Assistant Professor of Chemical Engineering
Assistant Professor of Civil Engineering
Thesis Supervisor

Accepted by: _____

Patrick S. Doyle
Professor of Chemical Engineering
Chairman, Committee for Graduate Students

The Aging of Organic Aerosol in the Atmosphere: Chemical Transformations by Heterogeneous Oxidation

by

Sean Herbert Kessler

Submitted to the Department of Chemical Engineering on 17 May 2013 in Partial Fulfillment of the Requirements for the Degree of Doctor of Philosophy in Chemical Engineering

ABSTRACT

The immense chemical complexity of atmospheric organic particulate matter ("aerosol") has left the general field of condensed-phase atmospheric organic chemistry relatively under-developed when compared with either gas-phase chemistry or the formation of inorganic compounds. In this work, we endeavor to improve the general understanding of the narrow class of oxidation reactions that occur at the interface between the particle surface and the gas-phase.

The heterogeneous oxidation of pure erythritol ($C_4H_{10}O_4$) and levoglucosan ($C_6H_{10}O_5$) particles by hydroxyl radical (OH) was studied first in order to evaluate the effects of atmospheric aging on the mass and chemical composition of atmospheric organic aerosol, particularly that resembling fresh secondary organic aerosol (SOA) and biomass-burning organic aerosol (BBOA). In contrast to what is generally observed for the heterogeneous oxidation of reduced organics, substantial volatilization is observed in both systems. As a continuation of the heterogeneous oxidation experiments, we also measure the kinetics and products of the aging of highly oxidized organic aerosol, in which submicron particles composed of model oxidized organics—1,2,3,4-butanetetracarboxylic acid ($C_8H_{10}O_8$), citric acid ($C_6H_8O_7$), tartaric acid ($C_4H_6O_6$), and Suwannee River fulvic acid—were oxidized by gas-phase OH in the same flow reactor, and the masses and elemental composition of the particles were monitored as a function of OH exposure. In contrast to studies of the less-oxidized model systems, particle mass did not decrease significantly with heterogeneous oxidation, although substantial chemical transformations were observed and characterized.

Lastly, the immense complexity inherent in the formation of SOA—due primarily to the large number of oxidation steps and reaction pathways involved—has limited the detailed understanding of its underlying chemistry. In order to simplify this inherent complexity, we give over the last portion of this thesis to

a novel technique for the formation of SOA through the photolysis of gas-phase alkyl iodides, which generates organic peroxy radicals of known structure. In contrast to standard OH-initiated oxidation experiments, photolytically initiated oxidation forms a limited number of products via a single reactive step. The system in which the photolytic SOA is formed is also repurposed as a generator of organic aerosol for input into a secondary reaction chamber, where the organic particles undergo additional aging by the heterogeneous oxidation mechanism already discussed. Particles exiting this reactor are observed to have become more dramatically oxidized than comparable systems containing SOA formed by gas-phase alkanes undergoing "normal" photo-oxidation by OH, suggesting simultaneously the utility of gas-phase precursor photolysis as an effective experimental platform for studying directly the chemistry involved in atmospheric aerosol formation and also the possibility that heterogeneous processes may play a more significant role in the atmosphere than what is predicted from chamber experiments. Consideration is given for the application of these results to larger-scale experiments, models, and conceptual frameworks.

Thesis Supervisor: Jesse Kroll
Title: Assistant Professor of Chemical Engineering, Assistant Professor of Civil Engineering

Contents

List of Figures

List of Tables

Chapter 1

Introduction

The presence of particulate matter (or "aerosols") in the atmosphere is of special importance due to its impact on both human health [1] and global climate—in the latter case primarily due to both direct radiative forcing and cloud condensation effects [2, 3]. The high degree of uncertainty in predicting these effects underscores the need for both improved understanding of the underlying mechanisms of formation (and transformation) of particles and improved models to estimate both aerosol loading and its attendant influence on the planetary energy balance. Although aerosol particles have been extensively studied from the point of view of their inorganic components, characterization of organic aerosol remains less well understood, in large part because of the chemical complexity inherent in a system containing many diverse compounds. The number of uniquely identified compounds present in the atmosphere has been estimated to be in the tens of thousands [4], and the number of theoretically possible compounds is shown through Figure 1.1 to be several orders of magnitude greater, even in very narrow cases for which several restrictions are placed on the definitions of chemical complexity.

Organic compounds account for anywhere from 20% to 90% of the particulate matter present in the lower troposphere [5, 6], yet the exact chemical composition of these mixtures is difficult to fully characterize. Organic aerosol particles in the atmosphere have two distinct sources. Primary organic aerosols (POA) are emitted directly into the atmosphere, whereas secondary organic aerosols (SOA) are formed from the condensation of lower-volatility oxidation products of volatile and semi-volatile organic compounds (VOCs and SVOCs, respectively) present in the gas phase. SOA has been shown in many studies to contribute a substantial fraction to total organic particulate matter, though most field studies show measured amounts of SOA to be 10–100 times

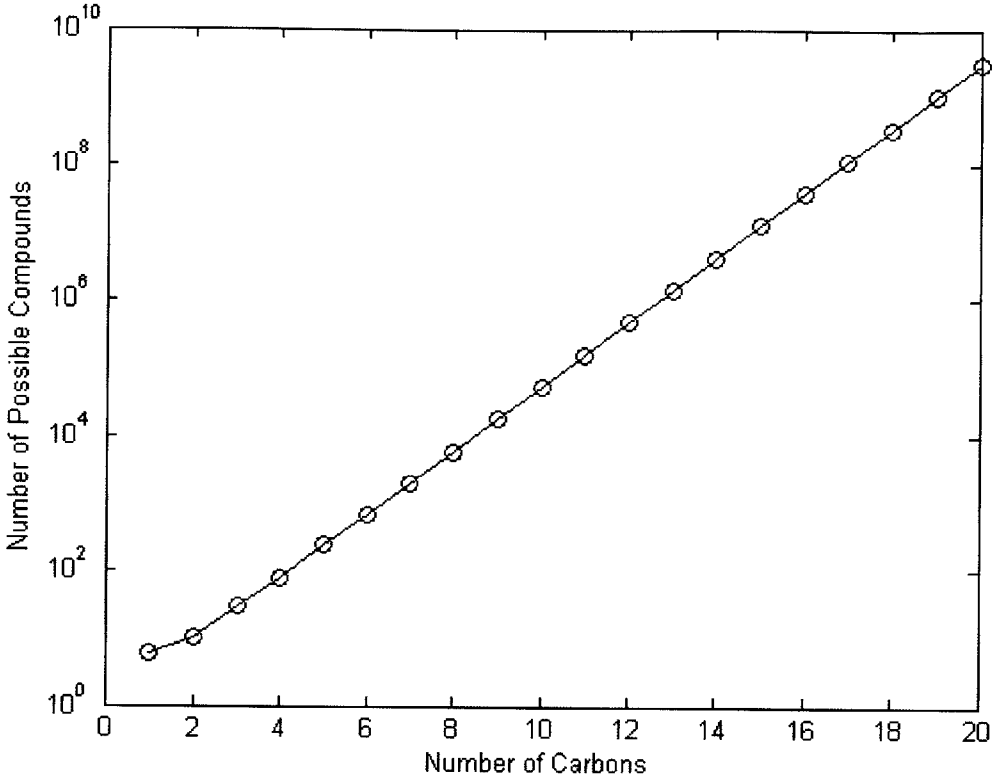

Figure 1.1: Total number of possible oxidized compounds for a given number of carbon atoms, assuming a linear backbone and allowing for hydroxyl, carbonyl, and carboxyl functional groups only.

higher than predicted by current models [7, 8, 9], indicating several as-yet unaccounted-for sources.

In addition, the classification of types of organic aerosol is further complicated by the definitions of various classes of oxidation through positive matrix factorization (PMF), which defines large datasets, containing time series of many mass spectra, in terms of a statistically restricted set of "factors", which are subsequently evaluated and given labels ranging from hydrocarbon-like organic aerosol (HOA, typically the most chemically reduced form) to oxygenated organic aerosol (OOA), biomass-burning organic aerosol (BBOA), and other region-specific factors [10]. Several factors, taken from multiple field campaigns and given the common label of low-volatility OOA (or LV-OOA), have been evaluated by elemental analysis, which is described in greater de-

tail in the next chapter, and are depicted in Figure 1.2 as a Van Krevelen diagram, which plots the hydrogen-to-carbon ratio (H/C) against oxygen-to-carbon (O/C) as a generic description of the chemical character of the organic species. In many cases, this description is sufficient to determine many useful properties of the aerosol as a whole [11, 12]. Even for a class of aerosol components with a common label and interpretation among the atmospheric chemistry community, we can observe a very broad range of values within this Van Krevelen space. The range in question is outlined using a confidence region based on the covariance of the data set itself [12].

The chemical oxidation of organic compounds in the atmosphere may occur in either the gas phase or the condensed phase (in the latter case, most frequently at the surface of a particle, via a heterogeneous mechanism), as indicated by the various mechanisms previously studied and depicted in Figure 1.3 [13, 14]. In many cases, oxidation is initiated by a hydrogen abstraction step, in which a hydroxyl radical (OH·) reacts with the organic compound to form an alkyl radical. The subsequent reaction pathways lead either to addition of functional groups (generally hydroxyl and carbonyl groups) to the carbon backbone of the molecule, which tends to lower the molecule's volatility, or to carbon-carbon bond scission, which frequently increases volatility [15, 16]. Additionally, oxidation of unsaturated hydrocarbons may also occur by an ozonolysis pathway, in which an alkene reacts directly with O_3 to form an ozonide intermediate before forming more heavily oxidized products [16].

Of particular interest in this work is the competition between those reactions that contribute to a net increase in overall oxygen content of organic aerosols (functionalization) and those that contribute to a net decrease in carbon content (fragmentation). Whereas functionalization reactions are likely to decrease the volatility of the organic species, fragmentation reactions typically lead to carbon loss by yielding two separate products, each one more volatile than the parent compound. The most common understanding of oxidation tends to assume that further oxidation generally leads to lowered volatility in almost all cases. Preliminary results observed in the oxidation of squalane, however, have demonstrated that fragmentation pathways are likely to be important even for mildly oxidized components [13].

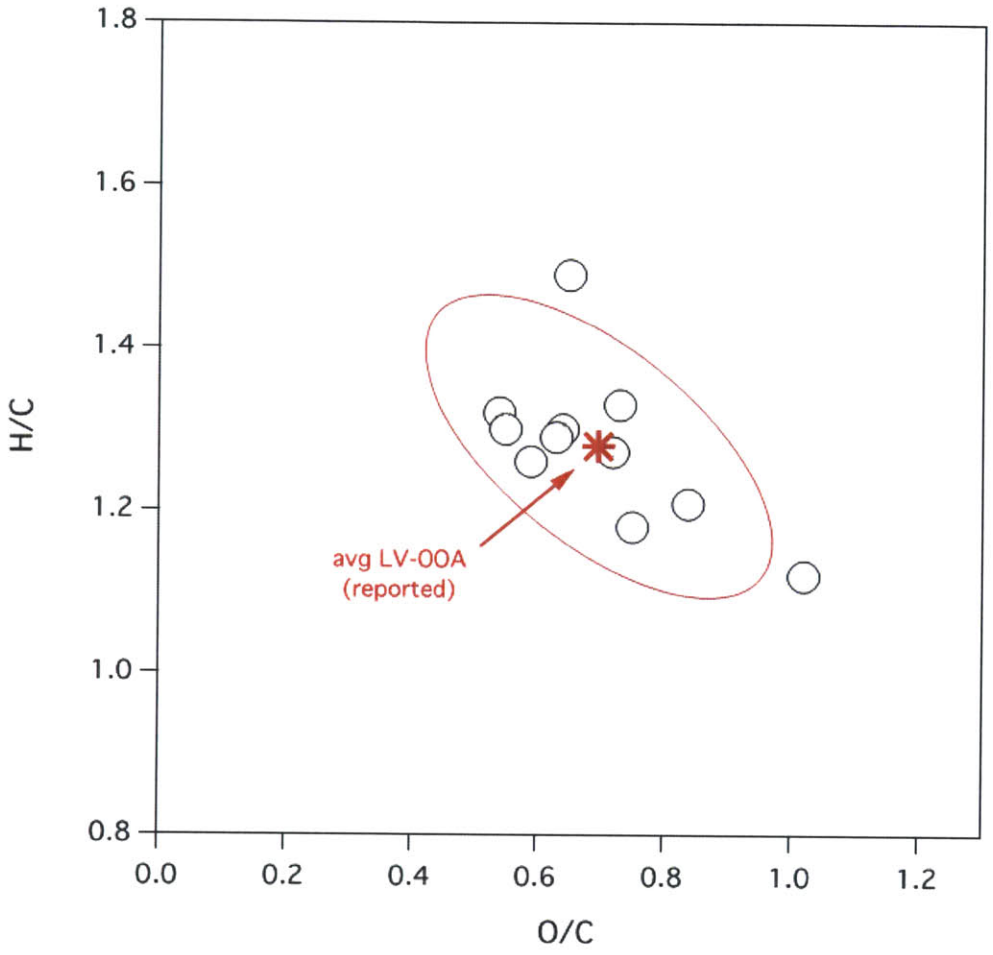

Figure 1.2: Van Krevelen diagram showing the reported elemental ratios of the LV-OOA factors from several HR-AMS field campaigns [12]. The red star denotes the average of all measured elemental ratios, with the ellipse indicating the covariance of the data within 1.96 standard deviations of the uncorrected mean value.

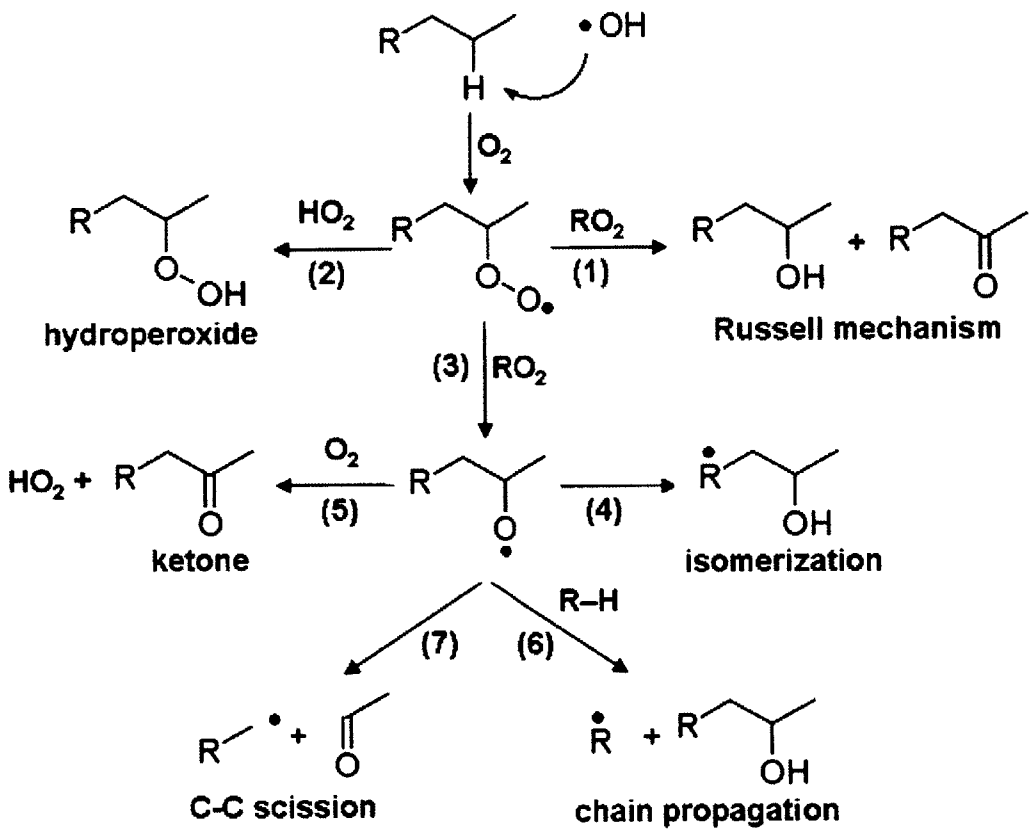

Figure 1.3: A general oxidation scheme for organic compounds in the atmosphere, in both gas and condensed phases, and in the absence of NO_x. All reactions depicted here are initiated by hydrogen abstraction by the hydroxyl radical (OH). Reaction rates and branching ratios between competing mechanisms are heavily influenced by a compound's partitioning between phases.

1.1 Classification of Mixtures

In considering the complexity of organic mixtures in the atmosphere, three classes, or orders, of organic mixture are of special note. The first, as discussed already, is the mixture of different possible reaction products available from a given oxidative step. Competition between fragmentation and functionalization reactions, and variations among numerous functional groups that may be added to a compound, characterize the complexity of this particular class, which grows larger with each successive reaction. The second grouping considers mixtures among different generations of products, as depicted in Figure 1.4. Smith et al. have shown that initial oxidation of a large starting com-

pound (in this case, squalane, a branched C_{30} alkane shown in Figure 1.5) may be represented in a simplified form by a single series reaction in which each generation is treated as a single product [14]:

$$\begin{aligned} Sq + OH &\xrightarrow{k} SqO_1 \\ SqO_n + OH &\xrightarrow{k} SqO_{n+1} \end{aligned} \tag{1.1}$$

If the same rate constant is used in each oxidation step (approximately valid for the first few reactions of a very large compound), the resulting analytical expression for the simplified system is

$$[SqO_n] = [Sq]_0 \left(\frac{\tau^n}{n!}\right) \exp(-\tau) \tag{1.2}$$

where $\tau \equiv k \langle OH \rangle t$ is the number of squalane lifetimes and represents the amount of exposure required to decrease the amount of starting compound by one exponential unit. As demonstrated in Figure 1.4, several generations may co-exist for a given exposure level, thereby adding to the complexity of the system.

Lastly, the degree of oxidant exposure to which a compound is subjected is determined by the amount of time it spends in the system of interest. Therefore, the residence time distribution, which is controlled by transport considerations, dictates variations in the number of average lifetimes a single particle may experience. An understanding of the interplay among all three classes of mixing is important for two reasons. The first is that each level of detail is necessary in order to accurately model the atmospheric behavior of organic species, since a small fraction of highly oxidized compounds may potentially contribute disproportionately to either aerosol mass or additional thermophysical properties of the condensed phase (e.g. cloud condensation activity and human uptake). Additionally, the collection of useful laboratory data requires restriction of higher-order mixing in order to yield useful insights regarding the specific microscopic behavior of the systems in question.

1.2 Modeling of Secondary Organic Aerosols

Most recent treatments of SOA follow the two-product model proposed by Odum [17], in which the fractional aerosol yield is determined from the indi-

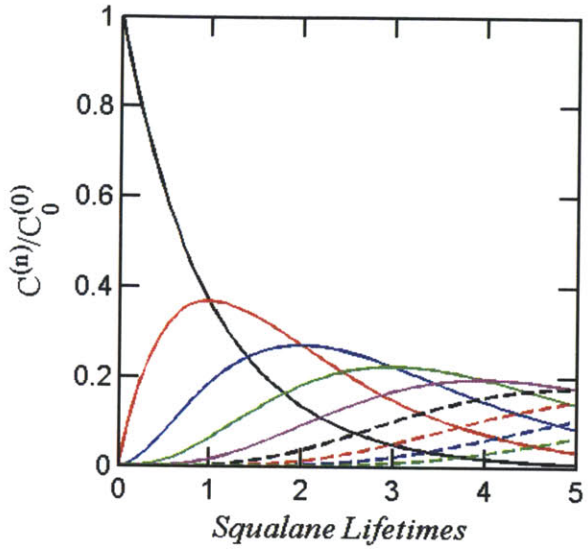

Figure 1.4: Evolution of squalane (black solid line), and the first-, second-, third- (red, blue, and green solid lines, respectively), and higher-generation oxidation products over increasing oxidant exposures.

vidual yields (α_i) and gas-aerosol equilibrium partitioning constants ($K_{om,i}$) of every possible reaction product according to

$$Y = \frac{\Delta C_{OA}}{\Delta C_R} = C_{OA} \sum_i \frac{\alpha_i K_{om,i}}{1 + K_{om,i} C_{OA}} \tag{1.3}$$

where C_{OA} is the mass concentration of organic aerosol present in the system and C_R is the concentration of the reactive species. The two-product model simplifies the above expression by assuming that the sum over all possible products can be represented by two characteristic pseudo-products:

$$Y \approx C_{OA} \left(\frac{\alpha_1 K_{om,1}}{1 + K_{om,1} C_{OA}} + \frac{\alpha_2 K_{om,2}}{1 + K_{om,2} C_{OA}} \right) \tag{1.4}$$

Application of this model to atmospheric systems entails identifying suitable precursors (primarily terpenes and aromatic hydrocarbons), performing chamber oxidation studies to estimate mass yields as a function of aerosol loading, and fitting the data to Equation 1.4 to obtain values of α_1, α_2, $K_{om,1}$,

and $K_{om,2}$ for the compound being studied. Several potentially important precursors have been characterized in this manner [18, 19], but the large number of candidate organic compounds underscores several limitations of the model. Because the model treats precursors on a compound-by-compound basis, it cannot make predictions for compounds that have not been explicitly identified and characterized, and the addition of each new precursor makes the non-linear solution of Equation 1.3 more unwieldy and prone to numerical errors. Additionally, the focus on aerosol production in terms of product yields implies a single-step chemical process, whereas multigenerational reaction kinetics have been demonstrated to act as both significant sources [20] and sinks [21] of SOA.

Another model, proposed by Donahue et al. [22], rewrites Equation 1.3 in terms of the total atmospheric concentration (as opposed to reaction yield) of a given compound:

$$C_{OA} = \sum_i \xi_i C_i; \qquad \xi_i = \left(1 + \frac{C_i^*}{C_{OA}}\right)^{-1} \tag{1.5}$$

where ξ_i is the fraction of the compound present in the condensed phase and C_i^* (which is just the inverse of $K_{om,i}$ as shown above) is the compound's saturation concentration in the gas phase, determined from the compound's vapor pressure, temperature, and activity coefficient in the condensed phase, as well as the average molecular weight of the aerosol mixture:

$$C_i^* = M_{OA}\gamma_i \frac{p_i^*}{RT} \tag{1.6}$$

In the Donahue model, the values of C_i^* are fixed (eschewing the assumption of a limited number of possible products), and all compounds of approximately the same volatility are grouped into bins. One practical benefit of grouping different molecules according to volatility is that if the total concentration C_i in each bin is known, the solution for organic aerosol mass requires only 6-7 terms and becomes relatively easy to solve numerically.

At the same time, grouping compounds by their partitioning constants at 25 °C is likely not to be sufficient to describe a given system completely. Different compounds with the same gas-phase saturation concentration are likely to have different reactivities or cloud condensing properties, and differences in heats of vaporization can change the volatility distribution significantly over the range of temperatures encountered within the troposphere (-60 to 30 °C).

Donahue et al. suggest the introduction of additional bins to describe chemical functionality, degree of oxidation, or elemental ratios as a means of capturing enough information to fully characterize a model system [22].

1.3 Overview of Heterogeneous Oxidation Experiments

The overarching goal of this work is to establish a useful set of rules for predicting the chemical behavior of organic aerosol systems undergoing aging via heterogeneous oxidation, which is considered as one narrow subset of all possible oxidation pathways in the atmosphere (including bulk condensed-organic-phase oxidation, gas-phase reactions, and aqueous chemistry). In order to sample from a sufficiently broad range of possible organic aerosol types, we choose to use a set of model compounds that represent several different relative levels of oxidation and have a wide array of functional groups. Figure 1.5 displays the major compounds studied in this thesis, each of which is introduced separately to a flow tube reactor (described in this section and in subsequent chapters, where relevant) and subjected to reaction with hydroxyl radicals (OH). These compounds include hydrocarbons (squalane, $C_{30}H_{62}$), poly-ols (erythritol and levoglucosan), and highly oxygenated acids, the last of which are used as representatives for OOA, which is otherwise very difficult to reproduce in a laboratory setting [23, 24, 25].

The reactor that is used to oxidize the compounds of interest is depicted in Figure 1.6. Briefly, compounds are introduced, already in the condensed phase as sub-micrometer particles, along with a mixture of hexane, ozone, oxygen, nitrogen, and water vapor. The ozone, in the presence of 254-nm light, rapidly photolyzes and reacts with water vapor to form hydroxyl radicals, which are the primary oxidants in this system. The exiting particle flow is monitored by several conventional (and commercially available) instruments, as well as the Aerosol Mass Spectrometer, which is discussed in greater detail in the next chapter.

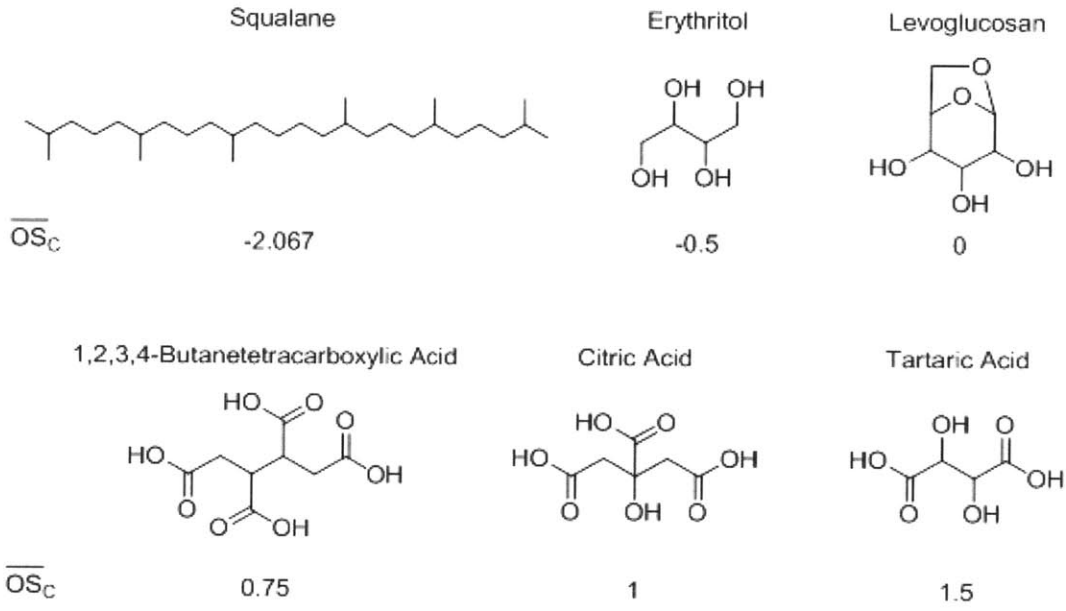

Figure 1.5: Chemical structures of the model compounds to be used in this work. Squalane [13]; erythritol and levoglucosan [26]; and tartaric, citric, and 1,2,3,4-butanetetracarboxylic acids [27] are all introduced separately into a flow tube reactor (by various methods described for each experiment) and subjected to reaction with high concentrations of the hydroxyl radical, OH.

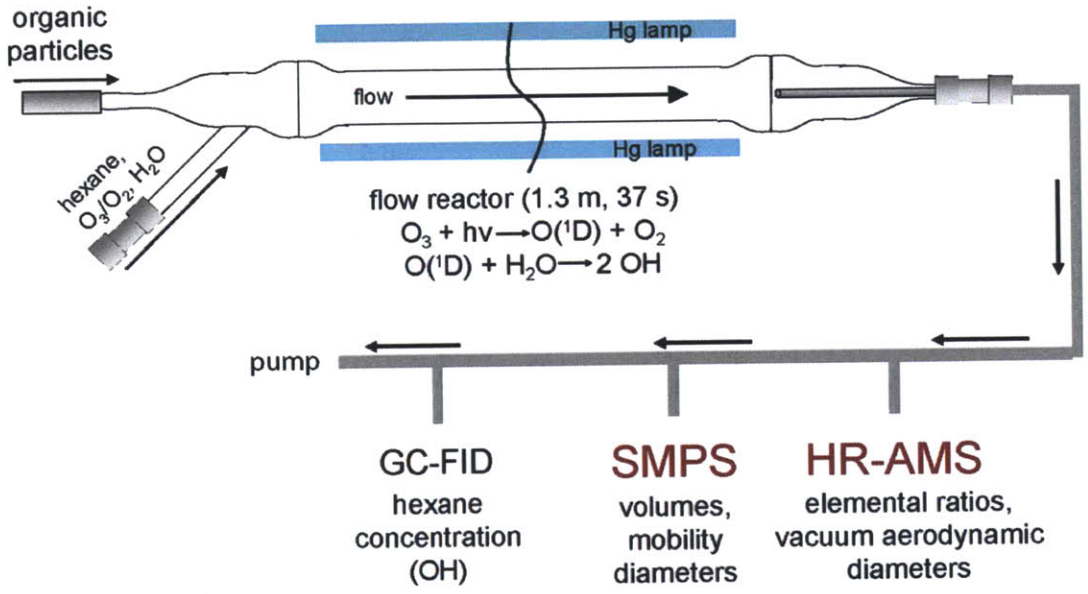

Figure 1.6: Diagram of the flow-tube reactor to be used in this work.

Chapter 2

Analysis of High-Resolution Aerosol Mass Spectrometry Data

Analysis of the composition of aerosols exiting our reacting systems was performed using a High-Resolution Time-of-Flight Aerosol Mass Spectrometer (HR-ToF-AMS, Aerodyne Research Inc., depicted in Figure 2.1) and has been extensively characterized [Jimenez 2003, Canagaratna 2007]. The front end consists of a sampling chamber in which the particle flow is sampled through a 100-μm critical orifice at a flow rate of $\sim$0.1 L min^{-1} and is focused through an aerodynamic lens at a pressure of $\sim$2 mmHg into a beam approximately 1 mm in diameter. The particle beam then passes to the ionization and subsequent detection region for mass spectral analysis of the entire condensed phase. Alternatively, if the instrument is set to "PToF" (Particle Time-of-Flight) mode, the beam is interrupted by a chopper so that aerosols enter a sizing chamber in small pulses. Individual particles are separated according to their vacuum aerodynamic diameter so that they enter the detection region at different times, thereby enabling the evaluation of a size-based distribution of mass spectra.

Mass spectra of the compounds and mixtures that pass through the selected front end instrument are analyzed via a time-of-flight mass spectrometer provided by Tofwerk AG. The main advantage afforded by this device is the use of high-resolution ($\sim$5000) data gathering to differentiate between fragment ions having the same nominal mass (e.g. CO_2^+, with a mass of 43.990, and $C_2H_4O^+$, with a mass of 44.026 amu, as illustrated in Figure 2.2 below). A common application of high-resolution mass spectral analysis is the evaluation

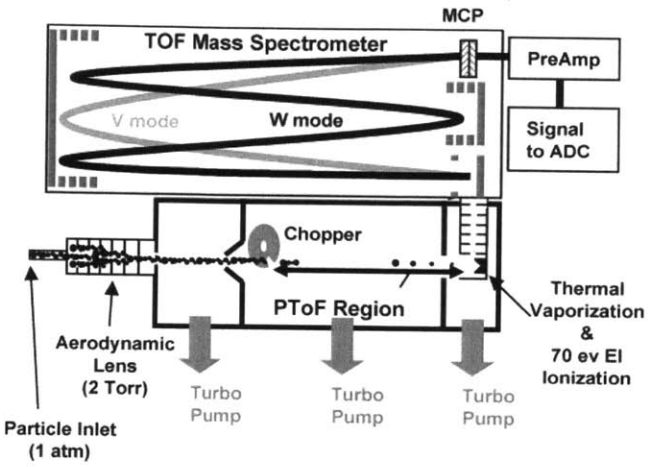

Figure 2.1: Aerosol Mass Spectrometer set-up. Particles are sampled at the inlet of the AMS front end, pass through a chopper and PToF chamber for sizing, and then enter the ionization region, where they are vaporized, ionized, and analyzed by time-of-flight mass spectrometry [28].

of elemental composition, as described below for systems using electron impact (EI) ionization [29, 30]. The utility of separating ion fragments shall be further illustrated in Section 3.2, which contains profiles of the two ions mentioned above for a system in which erythritol particles undergo oxidation in a flow reactor as described above. Although the unit-mass peak at $m/z = 44$ is frequently used as a marker for the degree of oxidation of a system [30], the case presented here shows that even as the system becomes more heavily oxidized (as indicated by the rising CO_2^+ peak), the unit-mass peak appears to decrease.

2.1 Ionization Techniques

The most common ionization method used in the commercial AMS is the well-characterized electron impact (EI) method, whereby molecules are bombarded by electrons from a tungsten filament at an electrical potential difference of 70 V. This process tends to lead to substantial fragmentation of organic molecules, so that there is frequently little to no trace of the original parent ion detected. Although this fragmentation precludes the identification of individual compounds within a mixture, the reduction of the mixture to a set of fragments, most with masses of no more than 100 amu, enables the unambiguous identification of many individual fragments, thereby allowing for the measurement

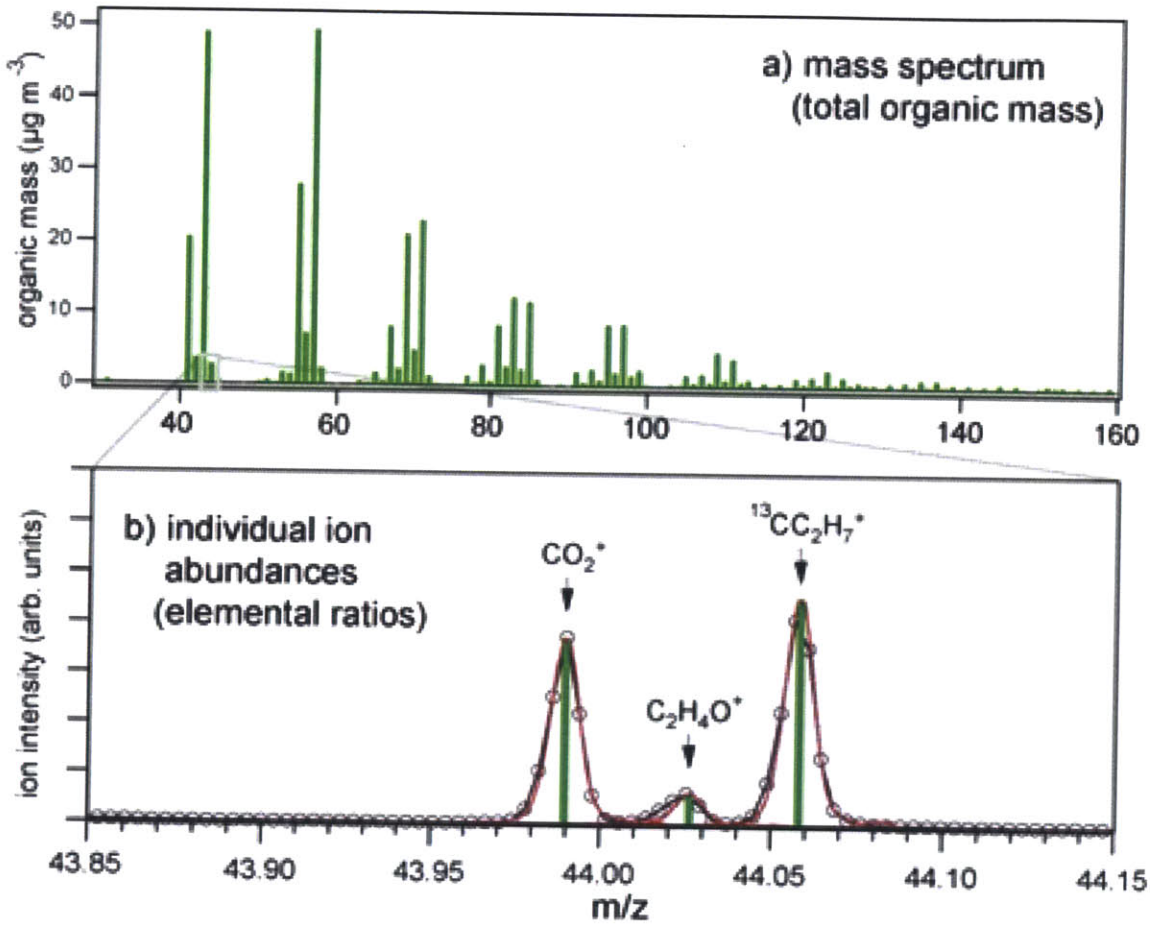

Figure 2.2: (Above) Unit mass resolution spectrum of a typical organic aerosol. (Below) High-resolution spectrum of the same organic aerosol at a nominal $m/z = 44$. Individual ions are differentiated by small deviations in mass.

of elemental ratios (oxygen to carbon, hydrogen to carbon, etc.) within the mixture [29, 30].

An alternative method of ionizing compounds, compared with EI as described above, is vacuum-ultraviolet single-photon ionization (VUV-SPI), a "soft" technique that avoids excessive fragmentation of analyte ions. Photon energies employed are within 10–12 eV, just above the ionization energy of typical organic compounds (8-11 eV). The ultraviolet light required can be generated from a krypton lamp mounted inside the AMS, with a plurality of emitted photons at energies of 10 and 10.6 eV [31], or from a synchrotron radiation source. Because the latter option affords the advantages of a much greater level of radiation intensity and a highly tunable photon energy output (to within 0.1 eV over a range of 5–20 eV), synchrotron radiation was employed for the entirety of this project through continuing collaboration with Aerodyne Research, Inc. and Lawrence Berkeley National Laboratory (LBNL).

The utility of VUV ionization is demonstrated in Figure 2.3 below, in which a highly branched alkane (molecular weight 422 amu) is introduced in aerosolized form to the AMS. Whereas EI ionization reduces the mixture to a series of fragments for which $m/z < 100$ (useful for bulk composition studies), VUV photoionization yields a predominant molecular peak and select few fragment peaks. When the particles are oxidized in a flow tube as described previously, several individual oxidation products can be identified and monitored with changing oxidant exposure in order to develop a working model for the kinetics of their time evolution [14].

2.2 Dimensionality Reduction of Aerosol Mass Spectra

Dimensionality reduction in the AMS has frequently been used as a means of extracting physically relatable information from complicated mass spectra. The most often-employed techniques include the calculation of total aerosol mass; the fractional presence of the marker peaks at $m/z = 43$ and $m/z = 44$, used respectively to identify moderately- and highly-oxidized OA [32]; elemental ratios H/C, O/C, and N/C [29, 30]; and positive matrix factorization (PMF), which identifies the reduced and oxidized portions of organic aerosol, in addition to specific sources from unique events (e.g. biomass burning), via statistical speciation of large amounts of time-resolved AMS data [10].

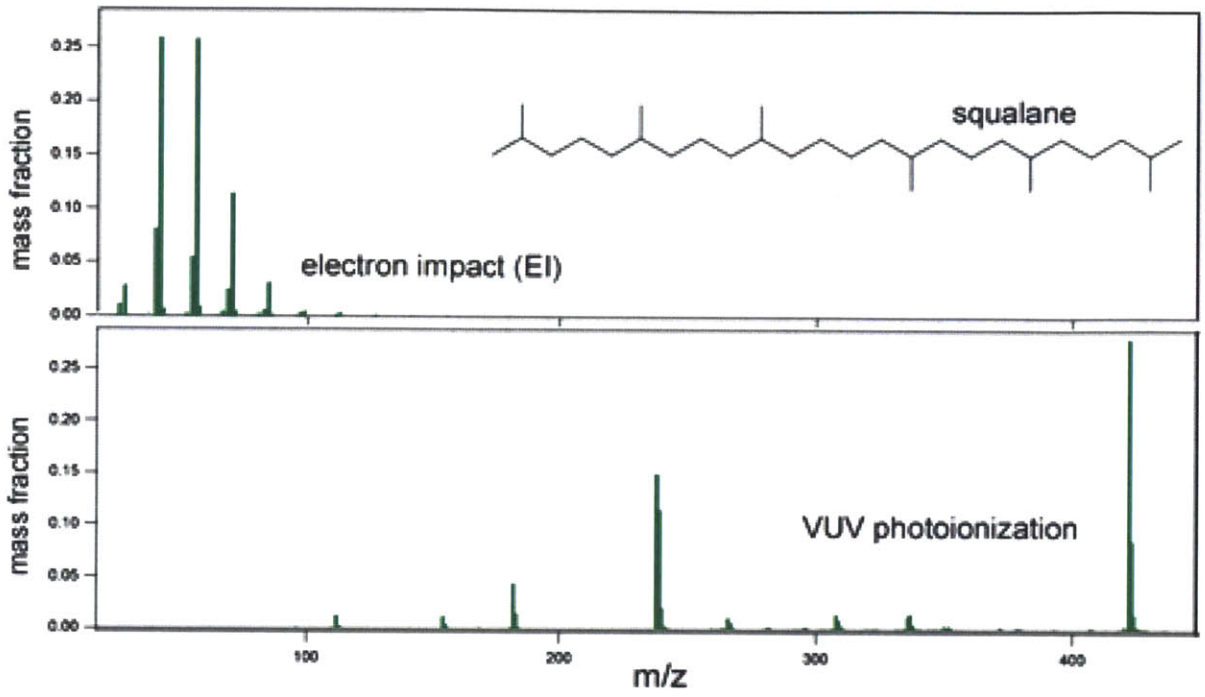

Figure 2.3: Mass spectra of squalane (branched C30 alkane, structure shown inset) generated using electron impact ionization and vacuum-ultraviolet photoionization. The "soft" ionization technique yields a molecular peak not otherwise seen in most EI-AMS studies, with only very mild fragmentation observed.

Each of these dimensionality reduction techniques is capable of providing highly useful chemical and/or physical information about the unresolved complex mixture of organic species that is typically found in ambient aerosol (e.g. by gas chromatography studies). However, by simplifying a high-resolution mass spectrum to only a handful of variables, we risk discarding additional information by over-simplifying. We therefore seek a means of consolidating the full mass spectrum in a manner that is physically descriptive, retains a substantial amount of chemical information from the original spectrum, and relies on a very small number of variables in the final output. To this end, we introduce the concept of an oxidation-state distribution of carbon atoms, which can be applied to a single molecule or to large complex mixtures of many molecules.

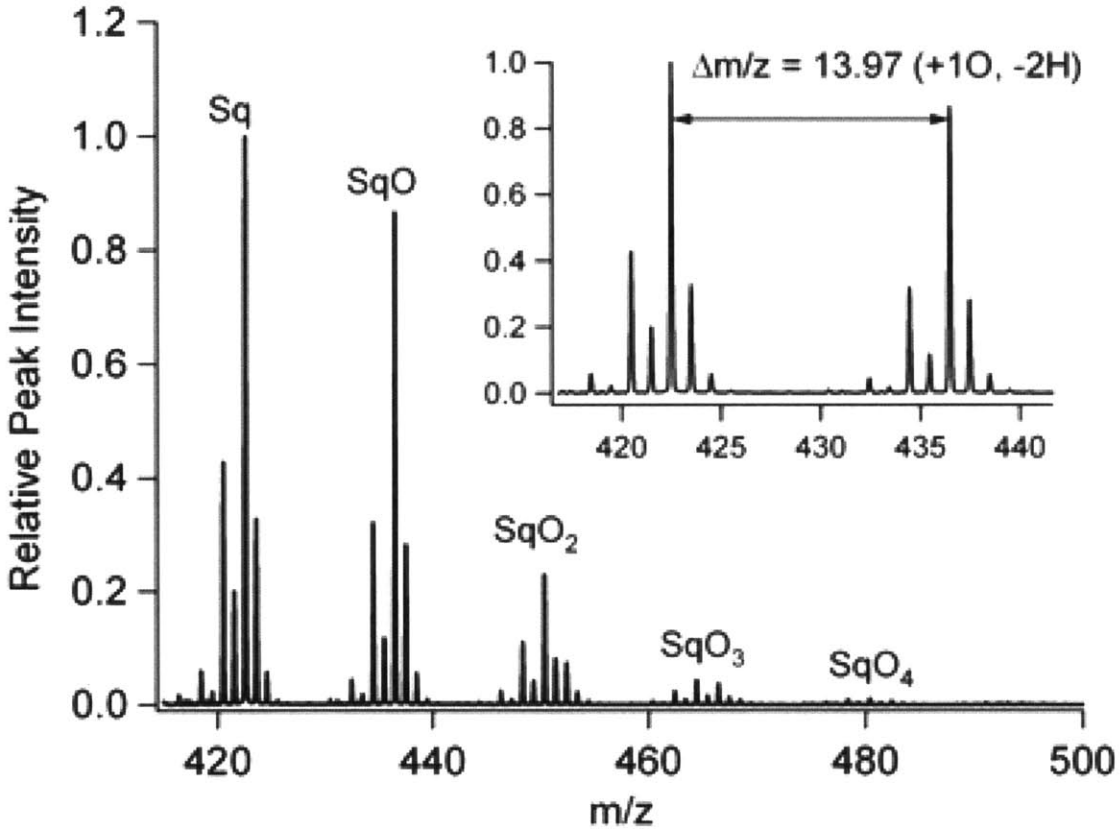

Figure 2.4: Mass spectrum of a multigenerational mixture of oxidized squalane particles, with different generations identified by the mass of the molecular peak.

The oxidation-state distribution, which we display here as a frequency histogram, identifies the fraction of total carbon at each possible oxidation state (which, for molecules with more than one carbon atom, ranges from -3 for the most reduced carbon, CH_3, to +3 for fully oxidized carbon, COOH). By subdividing total carbon in this way, we are able to present a picture of organic aerosol as a dynamic mixture of reduced and oxidized carbon in a manner that allows for both greater conceptual understanding of mass spectra and a potentially improved analysis of key physicochemical properties of the organic mixture (e.g. reactivity, hygroscopicity, refractive index [11, 33, 34, 2, 35]).

2.3 Discussion

Construction of an oxidation-state distribution for a single molecule is relatively straightforward. With very few exceptions (e.g. molecules containing a single carbon atom), the oxidation state of carbon atoms within a molecule typically take on integer values between -3 and +3. By counting the number of atoms at each possible state, we can construct a histogram depicting the relative frequency of each level of oxidation. One such sample histogram is depicted in Figure 2.5a, for pure citric acid, which contains two reduced secondary carbon atoms, a hydroxyl group on a tertiary carbon, and three carboxyl groups.

A similar approach is undertaken in constructing carbon oxidation distributions from mass spectra of unresolved OA mixtures. The AMS does not provide direct information about the degree of oxidation of each individual carbon atom. However, the high degree of fragmentation caused by electron impact (EI) ionization within the instrument ensures that a majority of the ion signal in the mass spectra comes from fragments containing three or fewer carbon atoms. As a result, the estimate of each fragment's average carbon oxidation state,

$$\overline{OS}_C \approx 2\frac{O}{C} - \frac{H}{C}, \tag{2.1}$$

will result in only modest errors compared with carefully reporting the oxidation state of each constituent atom. Different ion fragments with the same approximate $\overline{OS}_C$ are grouped together, and the carbon contribution from each one is tallied in order to produce a frequency plot, as illustrated in Figure 2.5b for atomized citric acid. The non-integer values depicted in the distributions are the result of taking the average oxidation state for fragments with multiple carbon atoms. Note that because the formal positive charge associated with each ion is a product of the ionization process, and not an intrinsic characteristic of the organic aerosol, it is ignored for the purpose of our analysis.

Additionally, an alternative method (for which the relevant code is provided in the Appendix) simplifies the distribution—as calculated from the AMS data—to integer values of OS_C in order to attempt an estimate of the "true" oxidation state distribution. The method by which this calculation is carried out involves first an empirical estimate of the relationship between the fraction of signal at $m/z = 44$ (specifically, the fraction of the ion CO_2^+) and

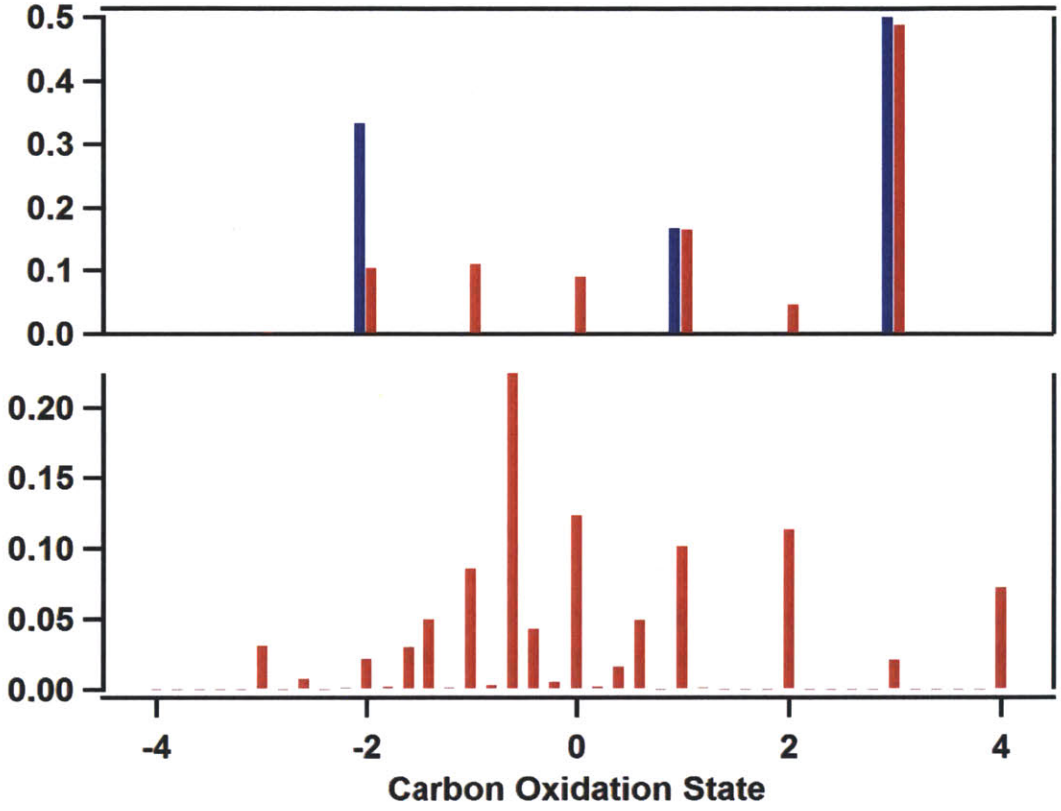

Figure 2.5: (Top, Blue) Oxidation state distribution of pure citric acid. (Top, Red) Inferred oxidation state distribution of citric acid obtained from manipulation of the mass spectra. (Bottom) Distribution of average carbon oxidation state of AMS fragments, weighted by carbon abundance.

the known fractional presence of carbon with an oxidation state of +3 in a given training set [29]. From there, the oxygen on remaining fragment ions is apportioned to values of -1 through +2 according to the relative degree of saturation (determined by the hydrogen content of the same fragments), and the remaining (non-oxidized) carbon in each fragment is apportioned to the reduced (-3 through 0) values of OS_C. Fragments with no oxygen content at all are apportioned to the values of -3 through 0 in the same manner, with non-integer values of $\overline{OS}_C$ determining the division of carbon between the two nearest integer values.

Such distributions are intended to provide a generic picture of reduced and oxidized OA that has greater physical significance beyond the simple MS-based picture, which typically must be interpreted by expert methods. Additionally, such distributions may avoid the potential danger in PMF studies of conflating the various factors (e.g. hydrocarbon-like OA and oxidized OA) with fixed classes of molecules. Because the oxidation state distribution is only concerned with the degree of oxidation of carbon atoms, there is no danger of conflation of the atomic information with molecular information.

In order to demonstrate the potential value of these oxidation-state distributions, Figure 2.6 provides distributions for the factors obtained by positive matrix factorization (PMF) from the CARES field campaign [36]. Each of the factors depicted has already been identified, on the basis of analysis of the high-resolution mass spectra, according to the relative levels of oxygenation observed. However, by simply processing the spectra individually, the degrees of oxidation can be depicted directly for ready analysis.

Additionally, Figure 2.7 depicts the oxidation state distributions at several different levels of oxidation in the heterogeneous aging of Squalane [13], ranging from unoxidized to several weeks' worth of OH exposure. Once again, the gradual increase in average oxidation state—and, as importantly, the broadening of the distribution to include a wider array of values—is depicted cleanly and directly. The distribution begins tightly centered about $OS_C = 2$, as is expected of typical alkanes. As particles become oxidized, the distribution becomes broader and shifts to higher oxidation states on average. We can also note that there is still some "reduced" carbon left in the mixture, even after heavy oxidation in the flow reactor.

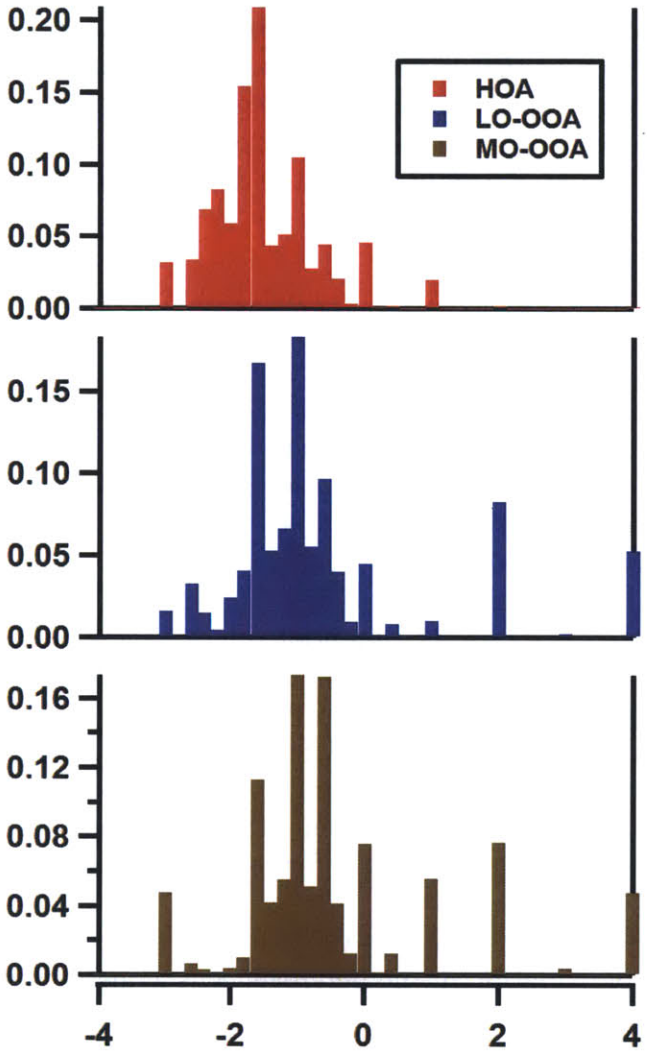

Figure 2.6: Distributions for three factors obtained by PMF from the CARES campaign. (Top, red) Hydrocarbon-like Organic Aerosol, HOA. (Middle, blue) Less-oxidized Oxygenated Organic Aerosol, LO-OOA. (Bottom, brown) More-oxidized Oxygenated Organic Aerosol, MO-OOA. The average of the distribution is observed to be higher for the factors identified as more-oxidized.

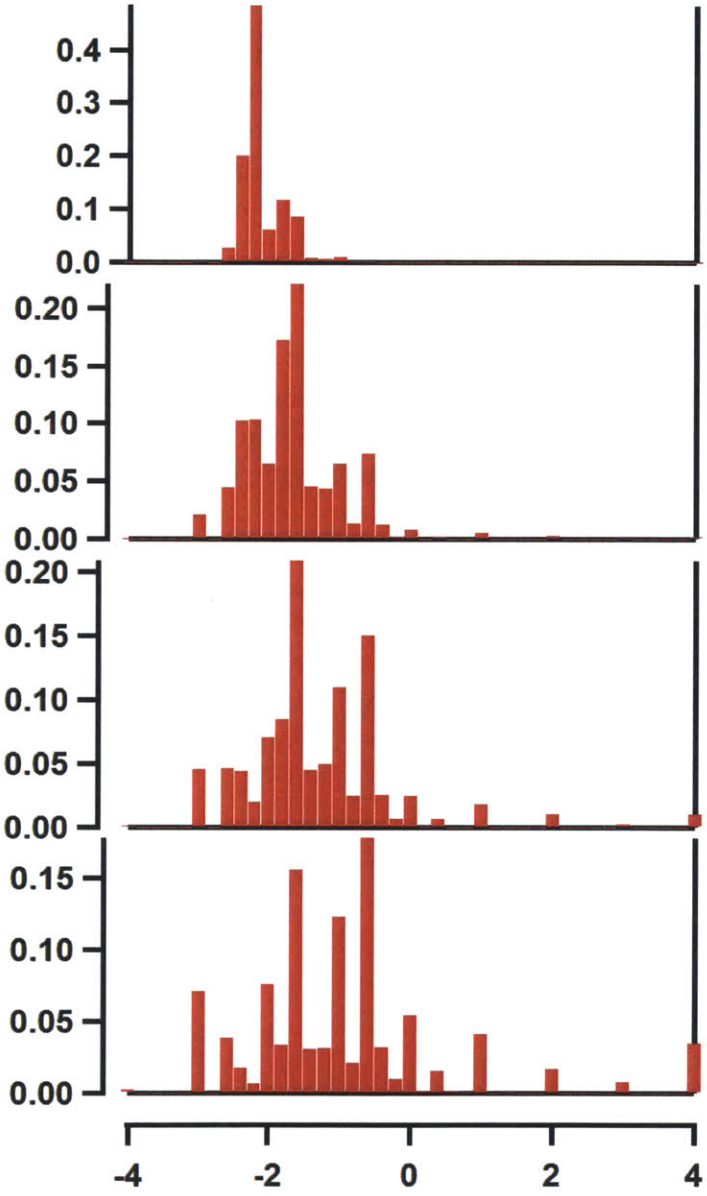

Figure 2.7: Distribution of the squalane OA oxidation state distribution at four different degrees of oxidant exposure.

2.4 Implications

We have introduced in this chapter a method for interpreting aerosol mass spectra that eschews the frequent view of OA as a sum of "factors". Rather, the distributions described herein approach the aerosol simply as a sum of many carbon atoms of varying oxidation states, in keeping with the traditional difficulty of obtaining any greater molecular information from the high-fragmentation EI mass spectra [28]. This view of OA as a distribution of components, rather than as specific molecules, allows us to examine with greater clarity how oxidation changes affect the mixture as a whole, with a gradual alteration of the distribution's shape indicative of the chemical transformations occurring within the particle phase.

In the future, we might consider using such distributions in the context of low-variable-number models of the kinetics of atmospheric oxidation, in order to better capture the nature of oxidative aging of OA. By using a universally-applied method of characterizing the aerosol components, a parameterization for the kinetics of oxidation may be introduced for the purpose of allowing comparisons among the many different classes of organic compound and aerosol type that are included in this thesis. Future work on this project should focus on creating a generalized framework for describing all of these classes in a single model, such that the evolution of novel systems can be accurately predicted prior to carrying out the relevant experiments.

Chapter 3

Heterogeneous Oxidation of Poly-Alcohols: Erythritol and Levoglucosan

The bulk of the work performed in this thesis focuses on experiments concerning oxygenated organic compounds, considering the many studies that have already been undertaken with respect to heterogeneous aging of reduced species and various types of chamber-generated secondary organic aerosol (SOA). Several of these studies [23, 37, 14] have previously found that substantial oxidation of reduced organic species, as well as loss of OA mass, occurs only at very high oxidant exposures, beyond what most particles will experience in their atmospheric lifetimes. Nonetheless, our work suggests that oxidized organic compounds may be susceptible to volatilization reactions; these may be atmospherically important given the abundance of oxidized compounds in OA [2].

In this chapter we investigate the kinetics and products of the heterogeneous oxidation of oxygenated (polyhydroxylated) species by exposure to hydroxyl (OH) radicals. We focus on two model organic systems, chosen both for their high degree of oxidation and for their importance as surrogate or tracer species in OA. Erythritol, $C_4H_{10}O_4$, is an analog of 2-methyl erythritol, a tracer species for isoprene SOA [38, 39]. Levoglucosan, $C_6H_{10}O_5$, is a known product of cellulose pyrolysis and is frequently used as a tracer for biomass burning OA (BBOA) [40]. Although the role of these compounds in atmospheric chemistry differs greatly, they are functionally similar, with low carbon numbers, several hydroxyl groups, and a relatively high degree of oxygenation (oxygen-to-carbon ratios of 0.8 to 1.0). The rates of oxidation of both species may strongly affect their efficacy as tracers in determining rel-

ative amounts of SOA and BBOA [41, 42, 43, 44]. More generally, the goal of this work is to investigate the possibility that oxidative aging of organic aerosol may serve as a chemical sink of atmospheric particulate matter (PM) via formation of volatile products [45].

3.1 Experimental Methods

The flow reactor used to study the heterogeneous oxidation of particles has been described in detail previously [13, 14] and is discussed briefly here. The reactor is made up of type-219 quartz, with a length of 130 cm, inner diameter of 2.5 cm, and residence time of ~37 s. Carrier flow consists of an O_2/N_2 mixture (in a 5/95 volume ratio), humidified to 30% RH. Organic aerosol is generated by sending an aqueous solution of each organic through either a constant-output atomizer (erythritol, 99% purity, Aldrich) [46] or a commercial nebulizer (levoglucosan, 99% purity, Aldrich) [47], and the resulting particles (surface-weighted mean diameter of ~270-305 nm) are drawn through a diffusion drier and into the flow reactor at loadings of ~500-750 μg m^{-3}. Such loadings are sufficiently high to ensure that more than 95% of the erythritol and 99% of the levoglucosan, respectively, is present in the condensed phase at equilibrium. Because non-equilibrium aerosol mixtures tend to favor the condensed phase due to slow evaporation rates [48], we are confident that heterogeneous oxidation reactions will dominate under these conditions.

Ozone is produced by either a mercury pen-ray lamp (1–10 ppm) or a commercial corona discharge ozone generator (10–200 ppm, OzoneLab Instruments). O_3 concentrations, which determine the level of OH exposure within the reactor are determined using an ozone monitor (2B Technologies Inc.). Within the flow reactor (temperature: 35 °C), ozone is photolyzed by UV light at 254 nm from two mercury lamps positioned immediately outside the quartz tube. $O(^1D)$ generated by ozone photolysis subsequently reacts with water vapor to form a pair of hydroxyl radicals (OH), which initiate oxidation of the particles. The water vapor concentration is maintained at a sufficiently high level to ensure that direct oxidation of particles by $O(^1D)$ is negligible, as determined previously [14]. Hexane (~100 ppb) added to the tube is monitored by GC-FID to quantify OH concentration. This technique has been used to correctly predict rate constants in the reaction of OH with other selected gas-phase hydrocarbons [13, 14]; OH concentrations, which are changed by varying O_3, range from 10^9 to 2×10^{11} molecule cm^{-3}. Such concentrations

correspond to approximate atmospheric exposures of one day to four weeks, assuming an average ambient OH concentration of 3×10^6 molecule cm^{-3}. It should be cautioned that these high OH concentrations may lead to significant secondary chemical effects, which would make linear extrapolation to ambient levels highly uncertain. Examination of these secondary effects by comparison of low- and high-concentration experiments at varying residence times is therefore an important topic for future research.

Particles exiting the flow reactor are sampled into a scanning mobility particle sizer (SMPS, TSI, Inc.), for the measurement of particle mobility diameters, and a high-resolution time-of-flight aerosol mass spectrometer (HR-ToF-AMS, Aerodyne Research, Inc.), for the measurement of particle composition (operating in "W-mode") and vacuum aerodynamic diameter ("V-mode"). Particle mass is obtained from combined SMPS measurements and AMS particle-time-of-flight (PToF) data, by multiplying average particle volume (from the SMPS) by the effective particle density (Figure 3.1). The effective density is calculated from the mobility diameter, D_m (SMPS), the vacuum aerodynamic diameter, D_{va} (PToF), and the standard density, ρ_0 (1 g cm^{-3}, used in calibration of the instrument), using the equation:

$$\rho_{eff} = \frac{D_{va}}{D_m}\rho_0 \tag{3.1}$$

Although this equation is strictly valid only for spherical particles, minor variations in particle shape will result in only small errors in measured mass, less than 10% [49].

Pure particles of levoglucosan and erythtritol did not change in composition or mass when the UV lights were turned on but no ozone was added, verifying both that the parent organic compounds studied are not directly photolyzed, and that UV-generation of condensed-phase oxidants is negligible. Significant gas-phase oxidation of the semivolatile compounds studied here is also highly unlikely, due to their strong partitioning into the particle phase and the short residence time in the flow reactor. Thus any oxidative changes to the mass or composition of the particles result from heterogeneous oxidation of particulate species by gas-phase OH radicals.

The amount of starting compound (levoglucosan or erythritol) lost by reaction is quantified by selecting a marker peak from the high-resolution mass

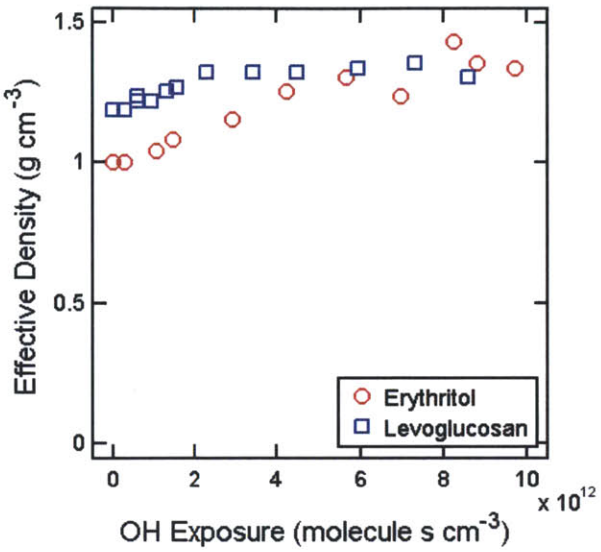

Figure 3.1: Measured effective density of particles for oxidized erythritol (red circles) and levoglucosan (blue squares). Actual densities of pure crystalline compounds are 1.45 and 1.5 g cm^{-3}, respectively. Discrepancies between real and measured values are likely to be caused by morphological effects and errors in PToF calibration, though these are not expected to affect our results (Figure 3.6).

spectrum and computing its fractional contribution to total AMS mass:

$$m_j = \frac{i_j}{i_{total}} m_{OA} \tag{3.2}$$

where i_j is the peak signal of the fragment ion selected to represent compound j, i_{total} is the sum of all organic peak signals from the AMS, and m_{OA} is the OA mass, normalized by particle number in order to account for wall losses (assuming that dilution has no effect on other particles), small atomizer fluctuations, and changes in collection efficiency of the AMS. This method assumes that the chosen marker peak does not constitute a significant portion of the individual mass spectra of the oxidation products, so that the peak represents only the compound of interest. This approach has recently been shown to compare very well with offline techniques for quantifying levoglucosan [41].

The peak used to track the mass loss of erythritol is chosen to be $C_4H_8O_3^+$

($m/z = 104.047$), which is formed by the neutral loss of H_2O from the molecular ion ($M - 18$). Likewise, the selected marker peak for levoglucosan is $C_6H_8O_4^+$ ($m/z = 144.042$), also obtained by the loss of H_2O. Both peaks were observed to be the fragments of highest mass in the pure compound spectra for which the AMS signal-to-noise ratio was suitably large. It is unlikely that any oxidation products would contribute significantly to the selected peaks, since they are expected to be of lower mass (aside from oligomerization products, which are not strongly represented in these AMS spectra) and have fewer hydrogen atoms than the parent compound.

The effects of oxidation by OH exposure may vary widely, depending on the nature of the organic compound being oxidized. It is therefore useful to introduce the mass loss ratio (MLR), defined as the ratio of the change in particle mass to the change in mass of the reacting species. For a given particle mass m_{OA}, reactive species mass m_R, and particles initially composed of the pure reactive species, such that $m_{OA}(0) = m_R(0)$, one may write:

$$MLR = \frac{\Delta m_{OA}}{\Delta m_R} = \frac{m_{OA} - m_{OA}(0)}{m_R - m_R(0)} = \frac{1 - \mu_{OA}}{1 - \mu_R} \tag{3.3}$$

where μ is the mass fraction remaining of either total aerosol or the reactive species. For our purposes, we assume that $\mu_R = m_j/m_j(0)$, where m_j is the mass of the selected AMS peak as computed in Equation 3.2. The MLR therefore describes the approximate yield of gas-phase products upon oxidation. Values of the MLR are determined by averaging all data points for which the total particle mass loss is greater than 20%, since values computed at low-oxidation conditions are subject to substantial numerical errors, while values computed at high-oxidation conditions did not appear to vary significantly.

We characterize the chemical changes to the reacting systems in terms of changes to the overall elemental composition of the organic mixture in the condensed phase. In particular, the oxygen-to-carbon ratio (O/C) and hydrogen-to-carbon ratio (H/C) are combined to estimate the overall degree of oxidation of OA particles and the relative contributions of key functional groups. The method for calculating elemental ratios from high-resolution AMS data is described in detail by Aiken et al. [29, 30]. This approach requires a set of factors to correct measured values for biases in ion fragmentation. Such factors are expected to be most accurate for complex organic mixtures, such as are found in ambient OA. As noted by Aiken et al. [29, 30], these standard correction factors (0.75 for O/C and 0.91 for H/C), are not as accurate for the measurement of individual organic species, such as those studied in the

present experiments. We therefore use system-specific correction factors for these studies in order to ensure that the elemental ratios of pure compounds are reported as their known values. The correction factors used are 0.44 for O/C and 0.82 for H/C for erythritol, and 0.50 for O/C and 1.1 for H/C for levoglucosan, which is similar to the correction for pure levoglucosan reported previously [29]. Regardless of the correction factor used, the overall conclusions reached with respect to the oxidative mechanism described below remain unchanged.

3.2 Fragment Ions at $m/z = 44$

While most studies have in the past used the unit-mass resolution peak at $m/z = 44$ in order to quantify the presence of highly-oxidized compounds [30], we have in this case focused specifically on the CO_2^+ peak. For both pure erythritol and levoglucosan, the CO_2^+ signal is negligible, and the $C_2H_4O^+$ peak dominates the total $m/z = 44$ signal (Figure 3.2). As oxidation continues (Figure 3.3), the dynamic shifts to favor the presence of CO_2^+, so that the fractional contribution of $C_2H_4O^+$ may be used as a tracer for compounds closely resembling erythritol and other tetrols. The lack of a strong $C_2H_4O^+$ presence in some atmospheric measurements [50] may suggest that isoprene-derived tetrols contribute only weakly to the total sampled OA in several regions and points to a useful avenue of inquiry in future field studies.

3.3 Kinetic Model and Fitting

Traces used in Figure 3.6b and 3.6e are obtained from a fit to the model described herein. By designating the initial compound (erythritol or levoglucosan) as P_0, first-generation condensed-phase products as P_1, and volatilized products as V, we can write a simplified mechanism as:

$$\begin{aligned} P_0 + OH &\xrightarrow{\phi k_1} P_1 \\ P_0 + OH &\xrightarrow{(1-\phi)k_1} V \\ P_1 + OH &\xrightarrow{k_2} \text{Products} \end{aligned} \tag{3.4}$$

where k_1 is the decay rate coefficient of initial component, k_2 is the decay rate of first-generation products, and ϕ is the fraction of first-step reactions

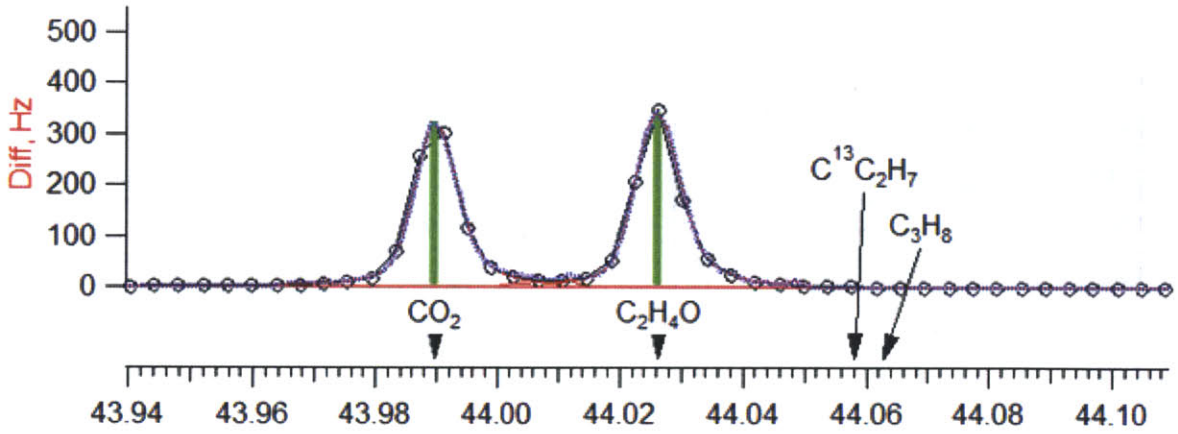

Figure 3.2: High-resolution AMS spectrum of highly oxidized erythritol, at nominal mass-to-charge ratio of 44. The separation of the CO_2^+ and $C_2H_4O^+$ peaks is clear and unambiguous, allowing for the calculation of elemental ratios [29, 30] and the monitoring of changes in specific fragment ions during the oxidation process.

that lead to production of low-volatility first-generation oxidized compounds. For small variations in the concentration of OH, the reaction scheme in equation 3.4 can be solved analytically to yield the concentrations of each species:

$$\begin{aligned} C_{P_0} &= C_{P_0}(0)\exp\left(-k_1\tau\right) \\ C_{P_1} &= \frac{\phi k_1 C_{P_0}(0)}{k_1 - k_2}\left[\exp\left(-k_2\tau\right) - \exp\left(-k_1\tau\right)\right] \end{aligned} \tag{3.5}$$

where $\tau = \langle OH \rangle \Delta t$ is the average OH exposure, as measured by the observed decomposition of hexane.

Non-linear exponential fits of concentration versus τ was performed for the initial slope of erythritol and levoglucosan, using the first line of equation 3.5, over the first e-fold in the data in order to determine the value of k_1, as depicted in Figure 3.4. This value was then inserted into the second line and combined with a non-linear fit of first-generation measurements in order to then determine k_2.

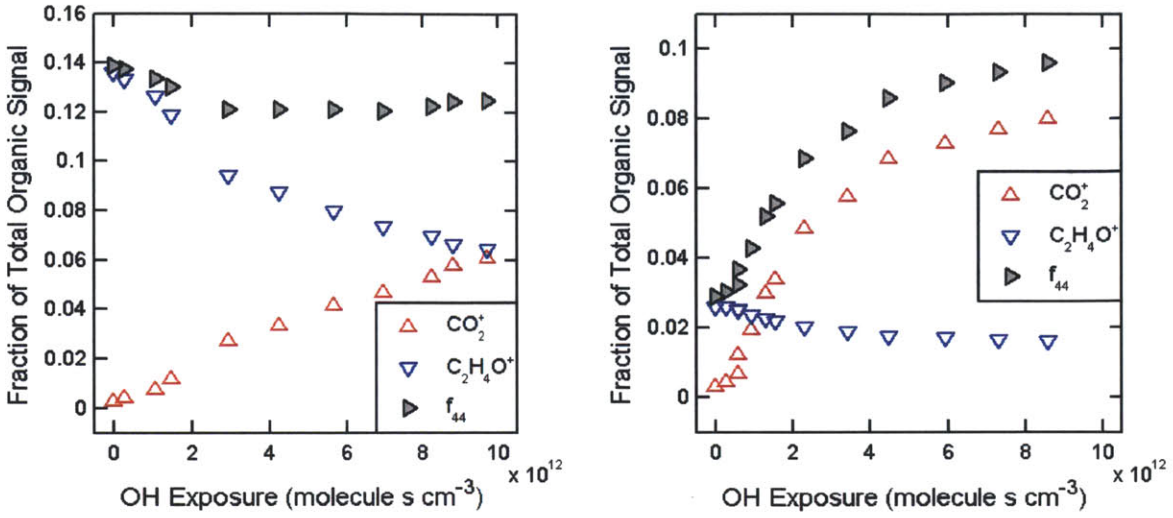

Figure 3.3: Fractional contribution of CO_2^+ (red) and $C_2H_4O^+$ (blue) to organic signal in the erythritol system, along with the combined signal at $m/z = 44$ (gray).

3.4 Results

3.4.1 Erythritol

Figure 3.6a depicts the decay rates of both erythritol and total particle mass for the heterogeneous oxidation of pure erythritol particles (surface-weighted mean diameter: 270.5 nm). The exponential decay of erythritol is consistent with a pseudo-first-order approximation of the second-order reaction of organic compounds with OH, although the chosen marker peak ($C_4H_8O_3^+$) does not appear to decay to zero. Possible reasons for this apparent offset include unreacted erythritol in the core of the particles (with a slow mass transfer rate) and signal interference from product compounds at the marker peak. A fit over the range of 0–4 $\times$ 10^{12} molecule s cm^{-3} is therefore used (Figure 3.4) to obtain a rate constant of $(2.54 \pm 0.22) \times 10^{-13}$ cm^3 $molecule^{-1}$ s^{-1}. The mass loss ratio, as a measure of the formation of gas- versus particle-phase reaction products (Equation 3.3), is computed to be 0.75 ± 0.04. Thus the heterogeneous oxidation of erythritol leads primarily to the formation of volatile products (~75% yield), which escape into the gas phase. Reported errors reflect uncertainty in the AMS peak calculation, SMPS mass, and fluctuations in the atomizer flow

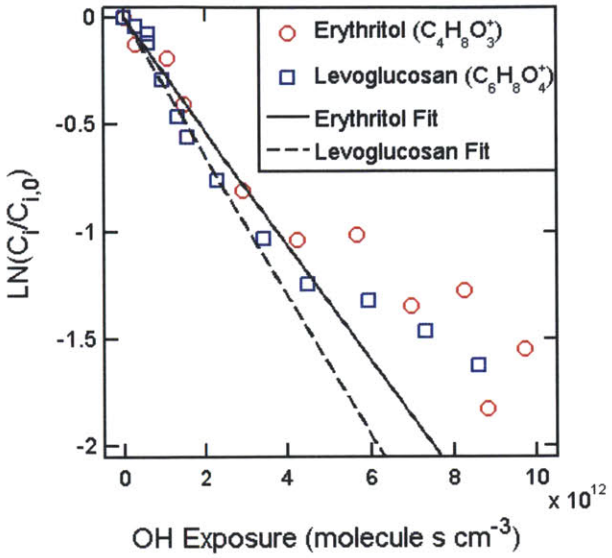

Figure 3.4: Exponential fits performed on measured erythritol (red circles) and levoglucosan (blue squares), presented on a logarithmic scale.

and OH concentration within the reactor.

Heterogeneous oxidation kinetics can be described in terms of the effective uptake coefficient $\gamma_{i,OH}$, defined as the ratio of the number of reactive collisions between OH and the compound of interest to the total number of collisions [14]. The uptake coefficient may be calculated from the determined second-order rate constant $k_{i,OH}$ according to

$$\gamma_{i,OH} = \frac{2D_0\rho_i N_A}{3\bar{c}_{OH}M_i}\chi(D_0)k_{i,OH} \tag{3.6}$$

where D_0 is the surface-weighted average particle diameter at the start of the experiment, ρ_i is the density of the organic compound, N_A is Avogadro's number, $\bar{c}_{OH}$ is the average speed of hydroxyl radicals in the gas phase, and M_i is the molecular weight of the compound. The uptake coefficient calculated by this method for erythritol, after correcting for diffusion limitations (which account for approximately a 40% difference in the final value, using a diffusion constant of OH in air of 0.217 $cm^2\ s^{-1}$) [14, 51], is 0.85 ± 0.12. Equation 3.6 is exact for spherical particles and may slightly overestimate $\gamma_{i,OH}$ for particles with higher ratios of surface area to volume.

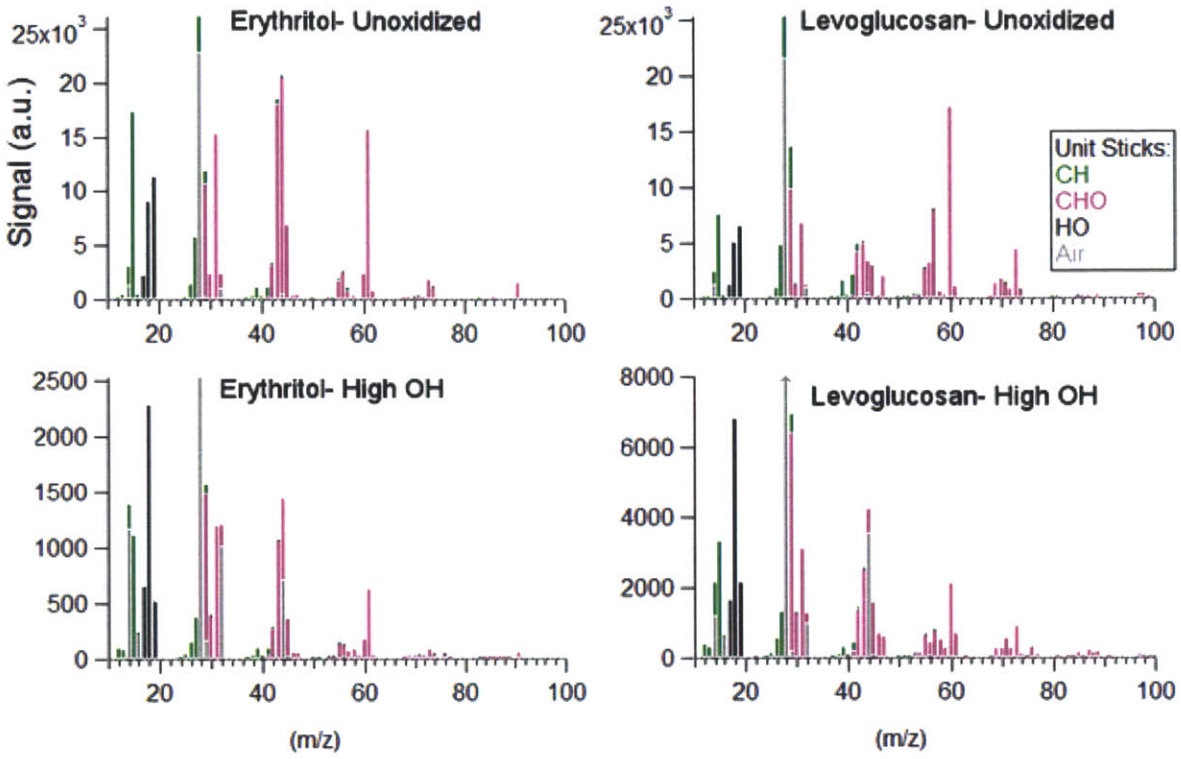

Figure 3.5: Representative AMS spectra of erythritol and levoglucosan, at zero OH exposure and at $\sim 8 \times 10^{12}$ molecule s cm^{-3}. Note the change in scale between unoxidized and oxidized spectra (a factor of $\sim$10 in the case of erythritol and $\sim$3 for levoglucosan), indicating a significant decrease in the total ion current observed by the AMS.

Figure 3.6b shows the evolution of three selected fragment ion signals from the AMS (each normalized to its maximum value for the sake of showing all fragments on the same scale) with increasing oxidant exposure. As in Figure 3.6a, the amount of erythritol remaining is represented by its marker ion, $C_4H_8O_3^+$. Additionally, we use $C_4H_7O_3^+$ ($m/z = 103$, $M - 19$) as a marker for first-generation oxidation products; the signal from this ion is negligible for pure erythritol compared with its observed rise in the reacting system. While the choice of marker peak is determined on a largely empirical basis, it should be noted that if we assume that each oxidation reaction involves the formation of a carbonyl, either by addition or by conversion of a hydroxyl group and

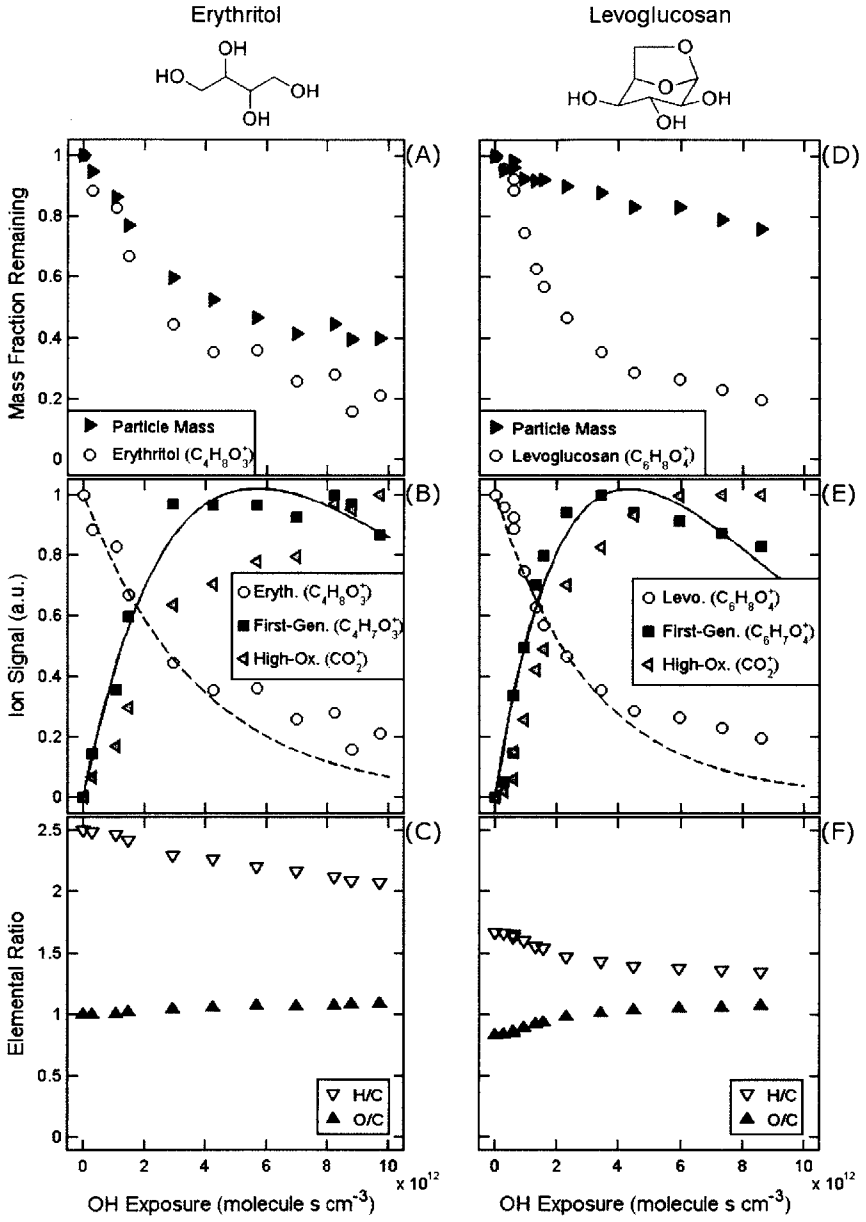

Figure 3.6: (A) Decay curves of pure erythritol (open circles) and total particle mass (filled triangles) over increasing oxidant exposures. (B) Mass contributions of selected marker peaks, used to represent erythritol (circles), first-generation products (squares), and heavily-oxidized products (triangles). Solid and dashed curves denote non-linear fits to Equation 3.5. (C) Hydrogen-to-carbon (H/C, open triangles) and oxygen-to-carbon (O/C, filled triangles) ratios of reacted erythritol system. (D-F) Structure and evolving characteristics of levoglucosan system, as compared to erythritol.

requiring the loss of two hydrogen atoms (as discussed in the next section), higher-generation products would necessarily have 6 or fewer hydrogen atoms and would therefore be unable to form the $C_4H_7O_3^+$ fragment ion. We are therefore confident that the selected ion peak serves as a useful metric for the formation of first-generation products.

The rate coefficient computed for the decay of erythritol is combined with a simplified two-step oxidation model (described in detail in Section 3.3) in order to estimate a rate coefficient for the decay of first-generation products, with the fit trace shown in Figure 3.6b. The resulting effective uptake coefficient is calculated by equation 3.6 as 0.28 ± 0.03, significantly less than that of its parent compound, erythritol. Although the model fits performed for these compounds (and for the levoglucosan system, discussed in the following part) tend to under-predict the amount of compound at high exposures, they provide a useful look at uptake rates for lower concentrations of oxidant (closer to atmospheric conditions) and give a conservative lower-bound estimate for the reaction rates of the compounds in question.

Lastly, CO_2^+ ($m/z = 44$) is taken to be representative of the most highly oxidized compounds present in the mixture, likely indicating the presence of carboxylic acid groups in product molecules; additional discussion of changes in the CO2+ presence may be found in Section 3.2. The calculated decay of first-generation products and apparent subsequent growth of more oxidized compounds together indicate that heterogeneous oxidation is a multigenerational process, in accord with previous results [14], and points to the continually evolving chemical nature of OA, which is consistent with a recent study of the heterogeneous oxidation of SOA [52].

The elemental ratios O/C and H/C for the particulate products of the reaction of OH with erythritol, as shown in Figure 3.6c, undergo the most rapid change during the initial stages of oxidation. Although the relative amount of oxygen in erythritol particles rises only slightly, the hydrogen content drops by a significant degree over the course of the reaction, suggesting that the dominant reactions that yield condensed-phase products are likely to involve the conversion of hydroxyl groups to carbonyl groups. The slight increase in O/C can be accounted for in part by the growing CO_2^+ signal (to a maximum of $\sim$6% of the AMS organic signal), which suggests the increased importance of carboxylic acid functional groups as well.

3.4.2 Levoglucosan

The levoglucosan oxidation experiments were analyzed using the same approach as used for erythritol, described above; results are presented in the right half of Figure 3.6. Figure 3.6d depicts the decay rates of both levoglucosan mass and total particle mass in a system initially containing pure levoglucosan particles (surface-weighted mean diameter: 304.3 nm). The exponential decay is again consistent with a second-order reaction model and has a corresponding rate constant of $(3.09 \pm 0.18) \times 10^{-13}$ cm^3 molecule^{-1} s^{-1}, with a diffusion-corrected effective uptake coefficient of 1.05 ± 0.11. Although this computed value is greater than unity (although within the calculated uncertainty), errors caused by under-estimating the average particle surface area using the mobility diameter may lower the actual value. The mass loss ratio, determined by equation 3.3, is 0.23 ± 0.04, significantly lower than what was observed for erythritol. This indicates that the majority of the products of levoglucosan oxidation remain in the particle phase. Hennigan et al. have reported a similar effect, whereby mass loss of biomass-burning organic aerosol upon oxidation is much slower than the loss rate of levoglucosan [41].

As with erythritol, we can measure the progression of selected marker ion peaks in the levoglucosan system with increasing oxidant exposure (Figure 3.6e). Initial levoglucosan is represented by $C_6H_8O_4^+$, first-generation products are denoted by $C_6H_7O_4^+$ (m/z = 143, $M - 19$), and the most highly oxidized compounds are monitored by CO_2^+. The selection of these three ion peaks follows the same process as described for erythritol in Figure 3.6b. Again, the growth and subsequent decay of first-generation products, coupled with the later rise in CO_2^+ signal, presents evidence of significant multigenerational chemistry on atmospherically relevant oxidation timescales. The effective uptake coefficient for product decay is calculated to be 0.39 ± 0.05, a similar effect to the one observed in the erythritol oxidation system, and fit traces for both levoglucosan and its products, described by Equation 3.5, are indicated in Figure 3.6e as well.

Levoglucosan undergoes a drop in H/C similar to erythritol, as shown in Figure 3.6f, but the larger rise in O/C suggests that oxidation reactions also involve the addition of new functional groups, such as hydroxyl, carbonyl, and carboxylic acid groups (CO_2^+ signal reaches ~8% of the total AMS organic signal), instead of solely the conversion of alcohols to carbonyls. As oxidant exposure increases, the values of O/C of both systems begin to converge to an upper bound of ~1.1.

3.5 Discussion

3.5.1 Oxidative mechanisms & Structural effects

In marked contrast to the heterogeneous oxidation of reduced particulate organic compounds [23, 37, 14], the heterogeneous oxidation of erythritol and levoglucosan leads to a substantial loss of OA mass via volatilization reactions. The differences in the mass loss plots of erythritol and levoglucosan (Figures 3.6a and 3.6d, respectively) indicate that the effects of oxidation on aerosol loadings are highly dependent on the chemical structure of the organic species in the aerosol. Although the two compounds decay at very similar rates—the effective uptake coefficients γ agree to within experimental uncertainty—the total particle mass follows this decay much more closely for erythritol than it does for levoglucosan. This discrepancy likely arises from differences in the chemical mechanisms leading to volatility changes.

These differences can be understood in terms of the mechanism of the oxidation of polyols, depicted in Figure 3.7 [53]. In pathway A, abstraction of a hydrogen atom from a carbon bonded to a hydroxyl group, followed by reaction with O_2, leads to the direct formation of a carbonyl without the cleavage of a C-C bond. In pathway B, the hydrogen atom is instead abstracted from the hydroxyl group directly. The resulting α-hydroxy alkoxy radical rapidly decomposes by C-C bond scission. While the former case raises product vapor pressure by approximately one order of magnitude [15], the latter may raise volatility by a much larger degree by decreasing the carbon number of each product molecule. However, in the case of cyclic molecules, "tethering" of the R groups allow for the cleavage of a C-C bond with no change to the carbon number. Levoglucosan, which has two cyclic moieties, can therefore undergo up to two cleavage reactions without dissociating to two separate molecules and so will not experience as dramatic an increase in vapor pressure as erythritol. The rate of mass loss relative to oxidation is therefore lower, suggesting that compounds with ring structures and higher molecular weights are likely to contribute to longer-lived organic aerosol.

Because both compounds are polyhydroxylated, similar pathways to those discussed above are possible for successive generations of oxidative reactions. The low decay rate of first-generation products in both systems-relative to the

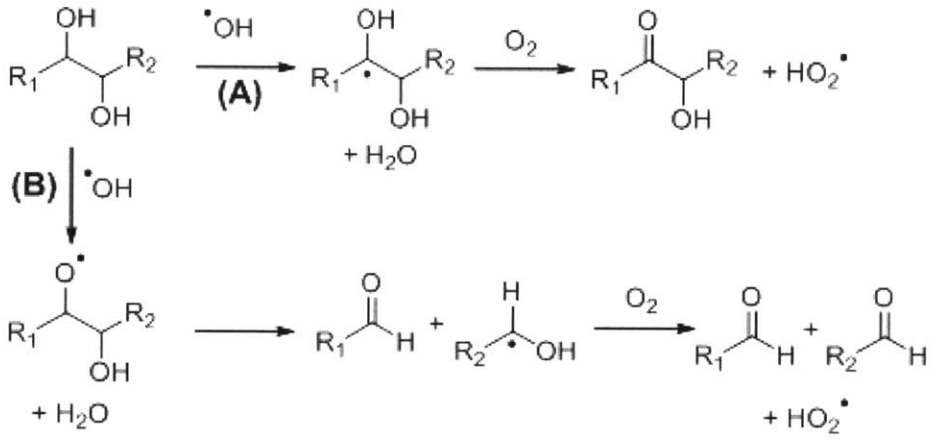

Figure 3.7: Two possible reaction pathways in the oxidation of erythritol and levoglucosan, adapted from Bethel et al. [53]. The functionalization pathway (A) leads to a higher degree of oxidation without resulting in the loss of carbon, but the conversion of a hydroxyl group to a carbonyl group results in a product of higher volatility. The fragmentation pathway (B) leads to degradation of C-C bonds and strongly increases overall particle volatility. If the two R groups are connected to each other, however, the molecular backbone will remain intact, and volatilization will be suppressed.

decay rate of initial compound-indicates, however, that the reaction process is demonstrably slowed, in part by the loss of hydrogen atoms needed for abstraction in the first step of oxidation. Although some degree of the difference in reaction rates can be explained by the changing sphericity of particles with increasing oxidation, conservative estimates of the uptake coefficient still yield significant discrepancies between the decay rates of initial compounds and the decay of first-generation products. Additionally, the growing presence of the CO_2^+ ion in both systems points to the likely production of carboxylic acid groups upon later generations of oxidation; this is consistent with our recent evidence that carboxylic acid addition becomes increasingly important with fragmentation reactions [13], although the detailed mechanisms are not yet well understood.

3.5.2 Van Krevelen Analysis

A "van Krevelen diagram" (a plot of H/C vs O/C) [54, 55] is introduced to make a direct comparison of elemental ratios independent of time or of oxidant

exposure (Figure 3.8). Heald et al. recently showed that for many ambient measurements of OA, as well as for several laboratory oxidation studies, elemental ratio data tend to fall along a line passing through (0,2) and with a slope of about -1 in this space, consistent with an approximately equal mixture of carbonyl- and hydroxyl-forming reactions during oxidative aging [54]. As shown in Figure 3.8, erythritol and levoglucosan are located at points far away from this line. As the particles are exposed to larger amounts of OH, the condensed-phase oxidation trajectory tends strongly downwards, with an approximate slope of -4.6 for erythritol and -1.3 for levoglucosan. The steeper slope for erythritol is a result of the conversion of hydroxyl groups to carbonyl groups. Both systems are moving towards similar C/H/O relationships, consistent with previous observations that oxidative aging of widely varying organic species tends to form products with similar chemical properties [2].

The chemical information supplied by a system's coordinates on a van Krevelen diagram is sufficient to estimate the minimum number of carbon atoms that a compound must have to be found predominantly in the particle phase at a given loading. These are determined by assuming that compounds are composed solely of contiguous saturated carbon chains and have only hydroxyl and carbonyl (and, by extension, carboxylic acid) functional groups. Volatilities are calculated using the group contribution method of Pankow and Asher [15], and the carbon number represents the minimum number of carbon atoms required to ensure that the compound will partition by at least one-half into the condensed phase [22]. A more complete discussion of the process of estimating the connection between n_C, O/C, H/C, and C^* may be found in the Appendix and will be used in subsequent chapters.

The shaded regions in Figure 3.8a represent the minimum carbon number calculated over the entire range of realistic O/C and H/C values for a system in which the aerosol loading is 700 μg m^{-3}, the approximate loading in the present experiments. The data for both erythritol (four carbon atoms) and levoglucosan (six carbon atoms) remain within the prescribed limits for condensed-phase elemental composition, indicating consistency between the estimated volatilities of organic compounds and the present measurements. However, because each point on the diagram represents an average in terms of the elemental composition of the system, individual products may be further removed from the observed data, leading to significant phase partitioning of some highly oxidized compounds.

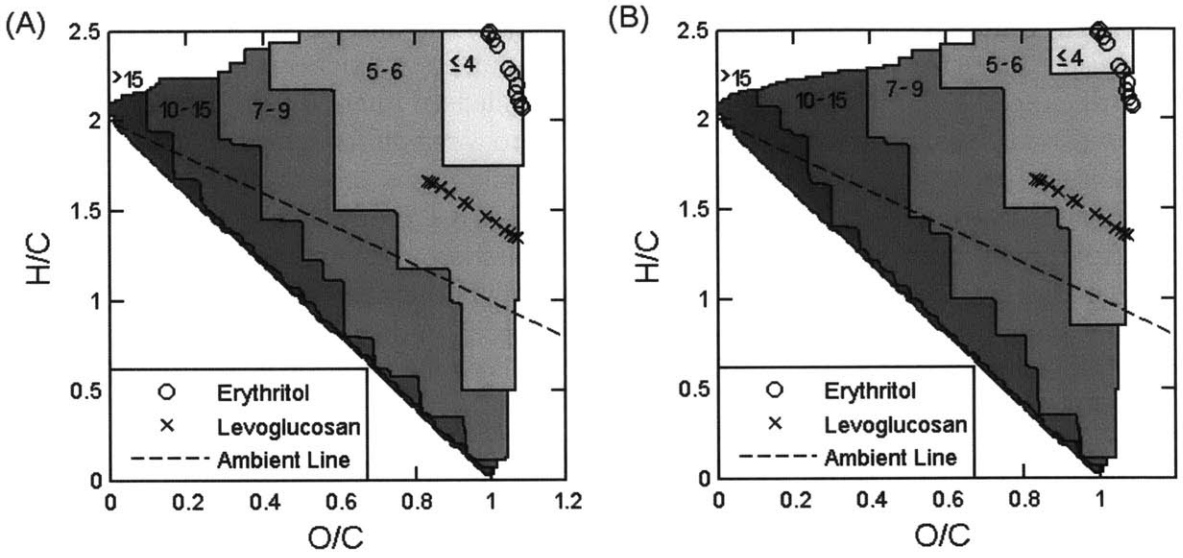

Figure 3.8: (A) Van Krevelen plot of H/C versus O/C for the erythritol (circles) and levoglucosan ('x') reacting systems. The direction of oxidation is downward and to the right for each system. Dashed line depicts the "ambient" line ($H/C = 2 - O/C$), which is the average of many measurements [54]. Shaded regions represent the approximate minimum number of carbon atoms per molecule required in order for the compounds to have a saturation concentration less than 700 μg m-3, the approximate mass loading of the systems considered herein. Blank spaces represent regions for which the calculated minimum carbon number, along with the represented hydrogen and oxygen numbers, result in chemically infeasible combinations in the absence of carbon-carbon double bonds. (B) The same Van Krevelen plot, with shaded regions adjusted to the more atmospherically-relevant loading of 10 μg m-3. The erythritol system average moves out of the "4-carbon" region at an OH exposure of 4×10^{12} molecule s cm^{-3}, corresponding to ~15.4 days of oxidation in the atmosphere.

3.5.3 Atmospheric Implications

Although Figure 3.8a is sufficient to describe the phase partitioning behavior of compounds in the present experiments, the aerosol loadings studied are 1-3 orders of magnitude greater than typical ambient loadings [2]. We correct for this in Figure 3.8b, which adjusts the contours to correspond to a loading of 10 μg m^{-3}. In this case, levoglucosan and its immediate oxidation products are still expected to remain largely within the condensed phase during aging. The erythritol system, however, moves rapidly into a region for which four carbon units is insufficient to ensure that oxidation products will be present primarily in the particle phase. Many of the condensed-phase products observed in this experiment are therefore likely to become even more strongly volatilized in the atmosphere, so that the mass loss ratio is likely to increase as the atmospheric OA loading becomes more dilute; this observation underscores the importance of volatility changes arising from interconversion of functional groups upon oxidation.

The effective uptake coefficient can be combined with estimates of particle size and atmospheric oxidant concentration in order to determine a pseudo-first-order rate coefficient for the compound of interest and, by extension, the compound's atmospheric lifetime. Assuming a mean diameter of ~200 nm and OH concentration of 3×10^6 molecule cm^{-3}, erythritol would have a heterogeneous oxidation lifetime of about 12.7 days, while levoglucosan would have a lifetime of about 9.6 days, both of which are very near the estimated depositional lifetimes (~10 days) of similarly-sized particles [5]. Whereas previous studies have suggested that heterogeneous oxidation of reduced organic species (i.e. hydrocarbons) [23, 37, 14] and some SOA systems [34] does not significantly affect aerosol mass on atmospherically relevant timescales, the much lower lifetimes determined here for levoglucosan and erythritol suggest that mass changes from heterogeneous reactions may be more significant for compounds that are already more oxidized and have low molecular weights, which is consistent with our recent results [13]. Additional studies have shown that in aqueous droplets and environments with high relative humidity, the lifetimes of both compounds are decreased to less than a day [41, 42, 43]. It should also be noted that because erythritol is semi-volatile, gas-phase oxidation reactions are likely to represent an even larger atmospheric sink for the compound in regions with low-to-moderate OA loadings; this may partially explain previous observations of a decrease in isoprene SOA mass by further aging [21].

The chemical lifetimes of OA mass contributed by these compounds—comprising the initial compound and its condensed-phase oxidation products-may be estimated approximately by dividing the product lifetime by its mass loss ratio. Since the mass loss ratio of erythritol approaches unity at atmospheric conditions, its OA lifetime will be about the same as that of erythritol ($\sim$12.7 days), suggesting oxidative aging could in fact be an important sink of polyhydroxylated (and possibly other oxidized) components of OA, though the secondary effects of more complex aerosol mixtures on oxidation remains an important topic for further research. The low observed MLR of levoglucosan, by contrast, implies longer-lived particle-phase products, on the order of several weeks, although OA continues to be slowly volatilized during this time. We therefore demonstrate that oxidized organic compounds found in both SOA and BBOA—which make up a large fraction of total aerosol loading [2]—are susceptible to further heterogeneous oxidation reactions and that these reactions are capable of significantly altering both the chemical composition and the mass of the oxidized OA.

Chapter 4

Heterogeneous Oxidation of Aged Organic Aerosol

One large source of the uncertainty in the prediction of the climate and health effects of fine atmospheric particulate matter is the extent to which organic particles may undergo physical and/or chemical changes over their atmospheric lifetimes [2]. Oxidized organic aerosol (OOA) has been difficult to accurately model in the oxidation of reduced species in the atmosphere, with respect to the rates, products, and effects on aerosol properties of the aging reactions involved. Detailed studies of such effects have been impaired by the difficulty of reproducing the atmospheric formation of highly oxidized aerosol in the laboratory [23, 24, 25] and the very high chemical complexity of such aerosol.

With a continuing focus on the heterogeneous oxidation of organic particles by gas-phase hydroxyl radicals (OH) [23, 34, 52, 26, 13, 14, 56, 37], the work up until this point has indicated that as particles are progressively aged, the degree of oxidation of the particulate carbon increases. Moreover, volatilization processes become increasingly dominant at these higher levels of oxidation, leading to significant decreases in aerosol loading (as discussed in Chapter 3).

Similar studies by other groups [23, 52, 13, 14, 26, 57] focused on the oxidation of relatively reduced organic aerosol, with average carbon oxidation states [58] of 0 or lower. Ambient measurements have shown that a large fraction of atmospheric organic aerosol is substantially more oxidized than this, with average carbon oxidation states as high as +1 [2, 58]. However, the reactivity (oxidation kinetics and products) of this oxidized organic aerosol is almost completely unconstrained at present; this limits our ability to accu-

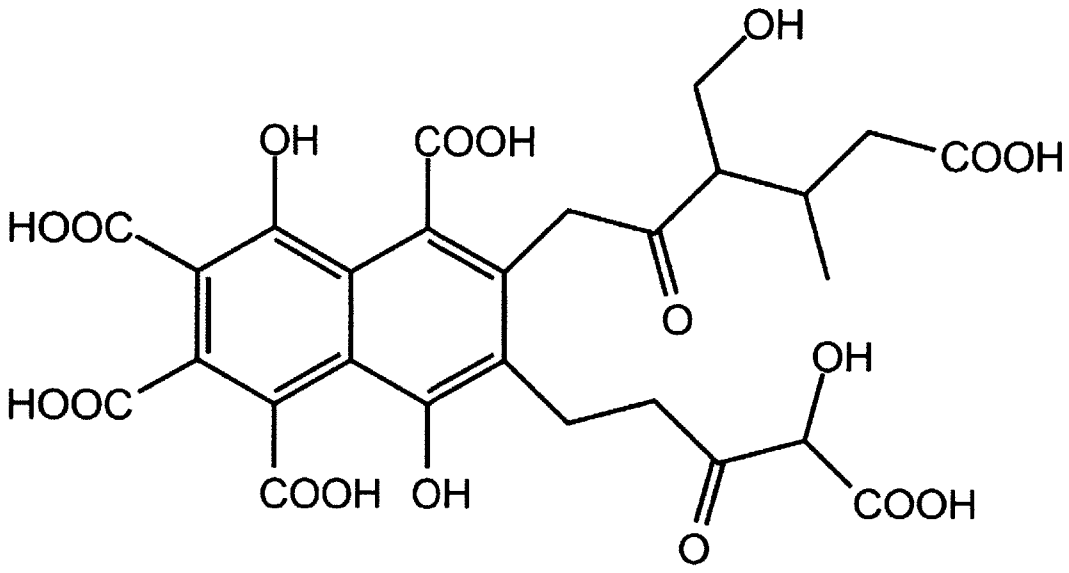

Figure 4.1: An assumed representative structure of an aquatic fulvic acid, based on fractionation and chemical analysis of samples [62].

rately model the evolution and fate of atmospheric organic aerosol. The goal of this part of the thesis is thus to study the oxidative aging chemistry of this already highly-oxidized aerosol in the laboratory. Because of the very low volatility of the constituent molecules [59, 60, 61], their fraction present in the gas phase is expected to be negligible, so that their oxidation must necessarily occur in the condensed phase. Therefore the aging mechanism probed in these experiments-heterogeneous oxidation by OH-is likely to be important in the atmospheric evolution of this class of organic aerosol.

4.1 Methods

As in our previous studies of less-oxidized species, the aging kinetics and chemistry of the aerosol are probed by studying the heterogeneous oxidation of simpler, more chemically tractable model systems. The surrogate organic species used in this study, chosen for their high oxidation states and low vapor pressures, are citric acid ($C_6H_8O_7$; Aldrich, 99.5%), L-(+)-tartaric acid ($C_4H_6O_6$; Aldrich, 99.5%), and 1,2,3,4-butanetetracarboxylic acid (BTA, $C_8H_{10}O_8$; Aldrich, 99%). Molecular structures and average carbon oxidation state ($\overline{OS}_C$) [58] of these model compounds and the three compounds from our

previous studies [13, 26] are provided in Figure 1.5. Additionally, the aging of a more complex organic mixture, Suwannee River fulvic acid (SRFA, obtained from IHSS) is also examined. SRFA has an $\overline{OS}_C$ that lies between 0.2 and 0.3 and is commonly used as a surrogate for highly oxidized organic aerosol in order to study laboratory techniques [63, 64].

Heterogeneous oxidation experiments are carried out in the same flow reactor used in our prior studies, which enables us to combine high OH concentrations and low residence times in order to quickly simulate multiple weeks of oxidation under ambient conditions. Again, the reactor is made up of type-219 quartz, with a length of 130 cm, inner diameter of 2.5 cm, and residence time of ~37 s. Carrier flow consists of 5% O_2 in N_2, at 30% relative humidity. Particles are generated by atomizing and subsequently drying aqueous solutions of each of the starting compounds; the resulting particles, which have surface-weighted mean diameters of ~130-145 nm, are drawn into the flow reactor at loadings of ~500-650 μg m^{-3}. These loadings are sufficiently high to ensure that at equilibrium well over 99% of the starting compound is present in the condensed phase, so that even for the most volatile compounds, gas-phase reactions will account for a very small fraction (less than 5%) of the total oxidation, assuming typical rates of hydrogen abstraction by OH [65].

Ozone is produced by either a mercury pen-ray lamp or a commercial corona discharge ozone generator (OzoneLab Instruments). O_3 concentrations, which control the level of OH exposure within the reactor, are measured using an ozone monitor (2B Technologies Inc.). Within the flow reactor (temperature: 35 °C), ozone is photolyzed by UV light at 254 nm from two mercury lamps positioned immediately outside the quartz tube. $O(^1D)$ generated by ozone photolysis reacts with water vapor to form a pair of hydroxyl radicals (OH), which initiate oxidation of the particles. The relative humidity in the flow tube, maintained at 30%, is sufficiently high to ensure that direct oxidation of particles by $O(^1D)$ is negligible, as determined previously [14], while also small enough to inhibit hygroscopic growth (~5% for organic acids) and the subsequent formation of an aqueous phase [64, 66, 67, 68, 69]. Hexane (~100 ppb) added to the tube is monitored by GC-FID to quantify OH concentration. This technique has been used to correctly predict rate constants in the reaction of OH with other selected gas-phase species [13, 14]; OH concentrations, which are changed by varying O_3, range from 1×10^9 to 3×10^{11} molecule cm^{-3}. These concentrations correspond to atmospheric OH exposures of approximately one day to four weeks, assuming an average ambient OH concentration of 3×10^6 molecule cm^{-3}.

Particles exiting the flow reactor are sampled into a scanning mobility particle sizer (SMPS, TSI, Inc.), for the measurement of particle mobility diameters, and a high-resolution time-of-flight aerosol mass spectrometer (HR-ToF-AMS, Aerodyne Research, Inc.), for the measurement of particle composition and vacuum aerodynamic diameter. Particle mass is determined by multiplying average particle volume (from the SMPS) by the effective particle density, which is in turn calculated from the ratio of the vacuum aerodynamic diameter (obtained from the AMS) to the mobility diameter (obtained from the SMPS) [49]. Although this method is strictly valid only for spherical particles, minor variations in particle shape will result in only small errors (less than 10%) in measured mass [49]. Measured effective densities (mostly in the range of 1.3–1.5 g cm^{-3}) do not vary significantly during the course of the experiments.

Particles of pure components do not change in composition or mass when the UV lights were turned on with no ozone added, verifying both that the parent organic compounds studied are not directly photolyzed, and that UV-generation of condensed-phase oxidants is negligible. Likewise, there are no compositional changes observed in the presence of ozone and absence of light, suggesting that direct reaction of the particles with ozone is negligible. Significant gas-phase oxidation of the compounds studied here is also highly unlikely, due to the strong partitioning into the particle phase, as previously mentioned, and to the short residence time in the flow reactor.

We characterize the chemical changes to the reacting systems in terms of changes to the overall elemental composition of the organic condensed phase. In particular, the oxygen-to-carbon ratio (O/C) and hydrogen-to-carbon ratio (H/C) are combined to estimate the overall degree of oxidation of the organic particles and the relative contributions of key functional groups. The method for calculating elemental ratios from high-resolution AMS data is described in detail by Aiken et al. [29, 30].

4.2 Results and Discussion

4.2.1 Oxidation Kinetics

The rate of heterogeneous oxidation was quantified by measuring the decay of the parent compound, as estimated by a selected marker ion. The marker ion

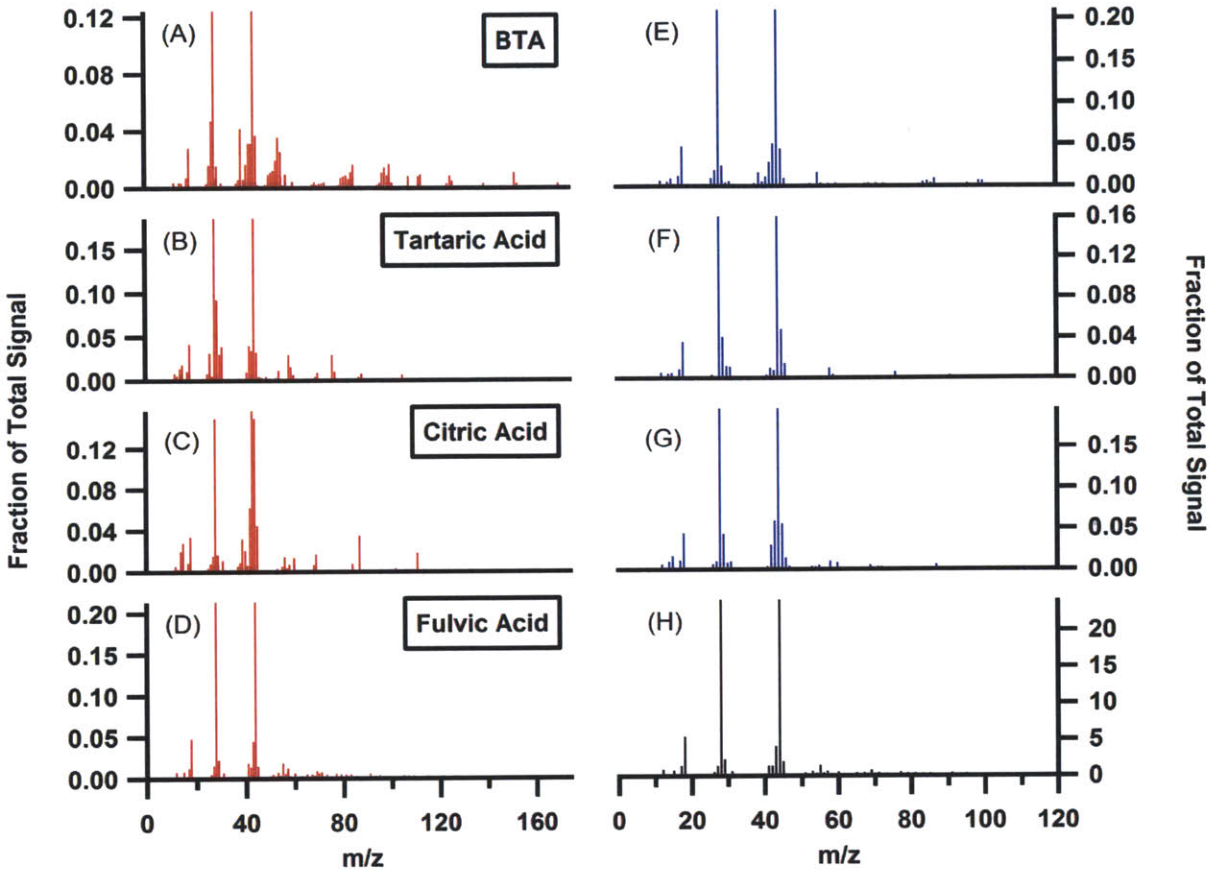

Figure 4.2: Aerosol mass spectra of reactants and products, with each mass spectrum normalized to the sum of its components. In all cases, peaks with $m/z > 120$ did not contribute significantly to the total spectrum. (A,C,E,G) Mass spectra of unoxidized BTA, citric acid, tartaric acid, and fulvic acid, respectively. The spectra of the single-component systems (panels A, C, and E) contain several high-mass ion fragments, which are used to identify the relative amount of the starting compound left in the mixture at a given level of oxidation. (B,D,F) Product mass spectra of the oxidation of BTA, citric acid, and tartaric acid, respectively, determined by spectral subtraction of the unoxidized spectra from the most oxidized spectra. (H) Mass spectrum of oxidized fulvic acid at the highest OH exposure. Residual spectra, and the mass spectrum of unoxidized fulvic acid, are dominated by low-mass oxygenated ion fragments, consistent with ambient measurements of oxidized organic aerosol.

selected for each experiment was identified by spectral subtraction. The mass spectrum of the pure component in each system was scaled and subtracted from the average spectrum at every subsequent oxidant exposure level, so that the resulting residual spectrum contained no negative peaks beyond a specified tolerance (peaks contributing less than 0.1% of the total mass were ignored in order to avoid confounding effects of a small background signal). The ion that most frequently disappeared first in each system was chosen as the marker ion: $C_4H_2O_3^+$ ($m/z = 98$) for tartaric acid, $C_4H_4O^+$ ($m/z = 68$) for citric acid, and $C_8H_8O_3^+$ ($m/z = 152$) for BTA. Mass spectra of the three single-component systems and residual spectra from the highest level of oxidation are provided in Figure 4.2. In all cases, the residual spectra—which represent oxidation products—are dominated by low-mass fragment ions such as m/z 44 (CO_2^+) and so do not provide suitable marker ions for the study of subsequent generations of oxidation. The mass spectrum of unoxidized fulvic acid is also shown in Figure 4.2; because it is a mixture of many compounds and does not exhibit any distinct marker ions, its kinetic behavior could not be determined.

Second-order rate constants for the reaction of the particulate organic species with OH, using the plotted intensity of the selected marker ions versus OH exposure (Figure 4.3), are estimated from an exponential fit using initial slopes, using only values corresponding to OH exposures below 2×10^{12} molecule s cm^{-3}, the range over which the parent organic species decays exponentially (in this and the previous chapter). The leveling-off observed for the marker ions at high OH exposures may be a result of a mass transfer limitation, possibly caused by changes in phase or viscosity as the particles evolve from a single-component to a multi-component system [70, 71]. This effect may prevent the oxidation of all of the parent species over the short timescale of the experiment (~37s). The kinetic model also assumes that the level of oxidation in the reactor varies only as the product of average OH concentration times the residence time. Secondary processes that do not vary linearly with the amount of oxidant present are more likely to have a strong effect at very high concentrations [56, 72], above the limit of 2×10^{12} molecule s cm^{-3} that we have set. Rate constants, determined for each single-component aerosol type, are listed in Table 4.1.

From the second-order rate coefficients and other known parameters of the system, we also calculate the effective reactive uptake coefficient, defined as the ratio of the initial rate of reactive loss of the parent species to the OH collision rate with the particle surface [14]. The uptake coefficient is calculated from the rate constant according to Equation 3.6 as discussed previously. Ap-

	BTA	Citric Acid	Tartaric Acid	Fulvic Acid
$k_i \times 10^{13}$	(7.6 ± 2.4)	(4.3 ± 0.8)	(3.3 ± 0.9)	N.D.
$\gamma_{i,OH}$	0.51 ± 0.19	0.37 ± 0.08	0.40 ± 0.13	N.D.
Atmospheric Lifetime	8 days	13	17	N.D.
Van Krevelen Slope	-0.31 ± 0.02	-0.33 ± 0.01	-0.60 ± 0.02	-0.59 ± 0.05

Table 4.1: Uptake Coefficients, Atmospheric Lifetime, and Van Krevelen Slope of Model Systems

plication of the diffusion correction discussed previously [51] accounts for a 15–30% increase in the calculated uptake coefficients. Uptake coefficients for the three single-component systems are listed in Table 4.1, with values ranging from 0.37 to 0.51. Such high values suggest that heterogeneous uptake in this experiment may be aided by the adsorption of OH to the particle surface prior to reaction with particulate organic molecules (or by adsorption of ozone and water, which can form OH directly at the surface), such that the radical has more time to abstract a hydrogen atom before diffusing away from the particle [52, 73]. Moreover, these values lie between the coefficient that we previously reported for squalane [14] and those of erythritol and levoglucosan [26]—all of which is consistent with the assumption that oxygen addition aids the stabilization of radicals during further oxidation while hydrogen loss tends to inhibit abstraction rates [74]—so we once again expect that heterogeneous oxidation will occur on atmospherically relevant timescales. Indeed, the lifetime against reaction with OH, estimated for particles with a diameter of 200 nm and an average OH concentration of 3×10^6 molecule cm^{-3}, ranges from 8 to 17 days (see Table 4.1), as compared with a depositional lifetime of $\sim$10 days for similarly sized particles [5].

4.2.2 Elemental Analysis

The oxidation trajectories of each of the four systems studied in terms of the hydrogen-to-carbon (H/C) and oxygen-to-carbon (O/C) ratios are presented in Figure 4.4. In order to compare the results with similar studies of ambient organic aerosol [54, 75], we calculate elemental ratios by modifying measured ratios by the empirical correction factor determined by Aiken et al. [29, 30]. The measured H/C and O/C values of the pure compounds tend to be lower than their exact values-an effect that has been previously reported for pure

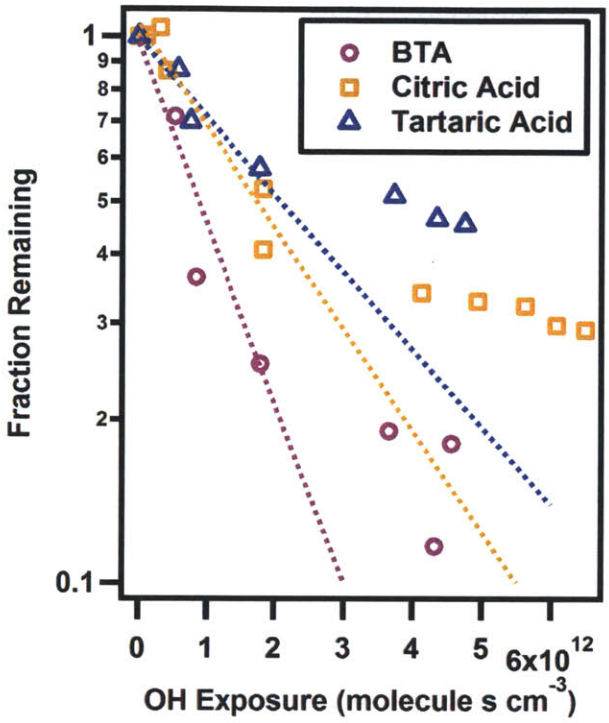

Figure 4.3: Mass fraction remaining of key ions in the oxidation of the single-component systems. $C_8H_8O_3^+$ ($m/z = 152$) is used for BTA, $C_4H_4O^+$ ($m/z = 68$) for citric acid, and $C_4H_2O_3^+$ ($m/z = 98$) for tartaric acid. An initial-slope exponential fit, which only includes ions at exposures up to 2×10^{12} molecule s cm^{-3}, is used to estimate the effective second-order rate coefficient for reaction with OH. The fitted trace is displayed over the data.

compounds using this technique [29]. However, the overall trends observed in the trajectories remain unchanged, regardless of the correction factor used. The slope of the trajectory is indicative of the average chemical transformation of particulate species [54]. For example, a slope of 0 corresponds to the addition of hydroxyl groups (oxygen addition with no net hydrogen loss), -2 corresponds to carbonyl addition, and steeper slopes denote the conversion of functional groups (e.g. hydroxyl to carbonyl, which involves a loss of hydrogen with no oxygen addition). On the other hand, if the oxidation reaction involves fragmentation-the cleavage of C-C bonds-and subsequent loss of carbon to the gas phase, then the resulting slope can take on a range of different values, depending on the chemical characteristics of the volatilized fragment. While previous studies have observed that measured ratios and trajectories

of reduced and lightly oxidized organic aerosol follow a line with a slope of -1 [54], the data presented here have slopes ranging from -0.6 to -0.3 (Table 4.1). This tendency of more highly oxidized systems to acquire oxygen with a smaller net loss of hydrogen is consistent with recent studies of the aging of oxidized organic aerosol [75].

One possible reason for the shift in slopes may be that at higher oxidation levels, reactions leading only to oxygen addition, such as the formation of hydroxyl groups, are more strongly favored [75]. However, the volatility of oxidation products likely also plays an important role, since the elemental ratios describe only those compounds of sufficiently low volatility to be present in the particle phase. This effect is illustrated in Figure 4.4, which relates elemental ratios (position in van Krevelen space), vapor pressure, and carbon number. The contours show the carbon number required for an organic compound to be present (at least 50%) in the particle phase under the conditions of the present experiments (i.e. where saturation vapor concentration equals aerosol loading [17, 22], $\sim$500 μg m^{-3}). These contours were determined by relating each point in van Krevelen space to a functional group distribution, assuming only hydroxyl, carbonyl, and carboxylic acid functionalities and estimating vapor pressures for a given number of carbon atoms using the SIMPOL group additivity method [15] and the steps outlined in the Appendix. Organic species with high O/C and H/C values (the upper-right of the van Krevelen plot) are the lowest in volatility and can therefore have a lower carbon number while remaining in the condensed phase, due to the increased possibility of strong hydrogen-bonding interactions. Therefore, as oxidation proceeds, and as fragmentation (C-C cleavage) reactions become increasingly important [13, 76], particulate products are more likely to be found in this area of the van Krevelen plot. This effect may explain the shallower slopes associated with the oxidation of highly oxidized species.

The particulate mass fraction remaining and the relative abundances of carbon and oxygen atoms in each of the systems studied is plotted against OH exposure (Figure 4.5). The exposure levels are adjusted to account for differences in particle size among experiments; the values presented are the estimated equivalent exposures for a particle with a surface-area-weighted mean diameter of 200 nm, using the relationship between rate coefficient and diameter presented in Equation 3.6. The slight increase in mass for the BTA and citric acid systems at the highest OH exposure level is attributed to fluctuation in the atomizer output, which causes the particle distribution to shift to larger diameters, rather than to a physical or chemical effect within the reactor. For

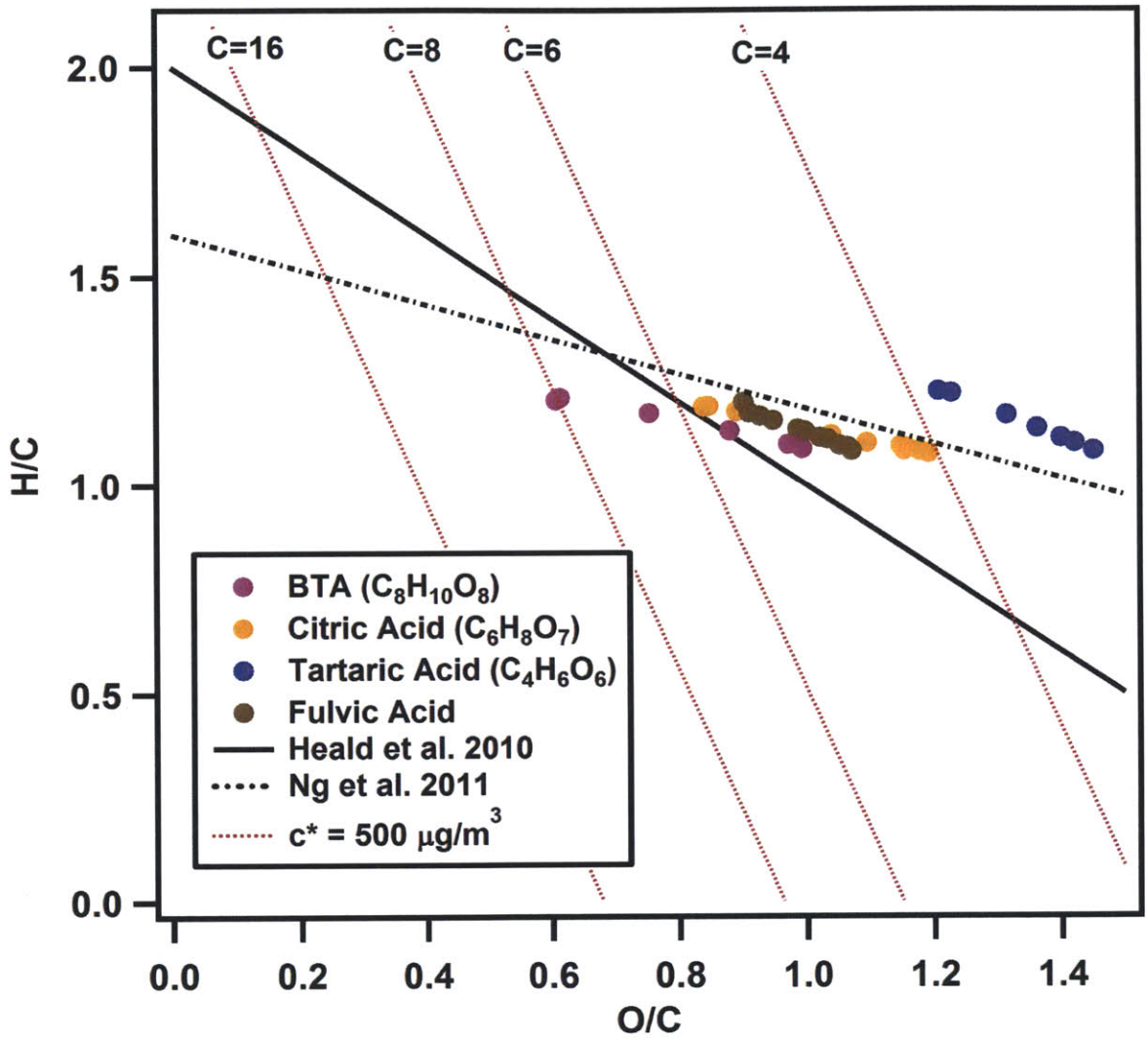

Figure 4.4: Van Krevelen diagram showing the elemental hydrogen-to-carbon (H/C) ratio vs. oxygen-to-carbon (O/C) at all points during the oxidation of the four systems in this study. The solid black line represents observations of ambient aerosol at moderate levels of oxidation [54]. The dashed black line represents measurements of ambient organic aerosol at higher oxidation levels [75]. Red contours represent lines of constant volatility-the approximate number of carbon atoms a molecule must have at a given elemental composition in order to retain a saturation concentration of 500 μg m^{-3}. As compounds become more oxidized, a shallower slope leads them more quickly to a region that allows a lower carbon content for the same volatility (or, conversely, lowers the volatility for a fixed number of carbon atoms).

each of the three pure-component systems, the loss of carbon by volatilization processes—principally fragmentation during oxidation—is offset by the addition of oxygen atoms, so that the total particle mass remains approximately constant. As a result, the primary effect of heterogeneous oxidation is to change particle composition (and therefore physicochemical properties), but not total mass. While there might be a mass transfer barrier that could prevent us from observing some eventual mass loss [77], our previous studies on more reduced systems have demonstrated our capability for observing more significant mass changes on similar timescales [26]. Moreover, our observation that the particles do not experience a significant change in mass upon aging is consistent with results from recent field measurements, which find that particle O/C, but not mass, increases with photochemical age [78, 79, 80].

4.3 Conclusions

The key changes to particles upon heterogeneous oxidation are examined in Figure 4.6 for all of the systems studied here, as well as those from our previous work (squalane, erythritol, and levoglucosan) [13, 26]. Figure 4.6a shows the overall degree of oxidation of the condensed phase species, as described by the average carbon oxidation state, approximated by the equation $\overline{OS}_C \approx 2\frac{O}{C} - \frac{H}{C}$ [58]. Regardless of the initial system chosen, there is invariably a marked increase in the level of oxidation upon exposure to OH. Furthermore, analysis of the atmospheric lifetimes of these compounds indicates that such chemical transformation by heterogeneous oxidation occurs on timescales commensurate with particle loss by deposition [5]. This is of particular significance for the lowest-volatility fraction of the oxidized organic aerosol, which is unlikely to be found in the gas phase and thus must undergo oxidation in the condensed phase-either by heterogeneous reaction with OH or via aqueous-phase chemistry [81].

Additionally, we can observe changes in the relative carbon content of each system as a function of OH exposure, which serves as a useful proxy for volatilization of the particulate organic species (Figure 4.6b); all systems exhibit some carbon loss, indicating that heterogeneous oxidation leads to the formation of oxidized species not only in the particle phase but in the gas phase as well. While the degree of carbon loss exhibits a good deal of variability from species to species, likely due to differences in carbon number and molecular structure, general trends with oxidation state are apparent. The

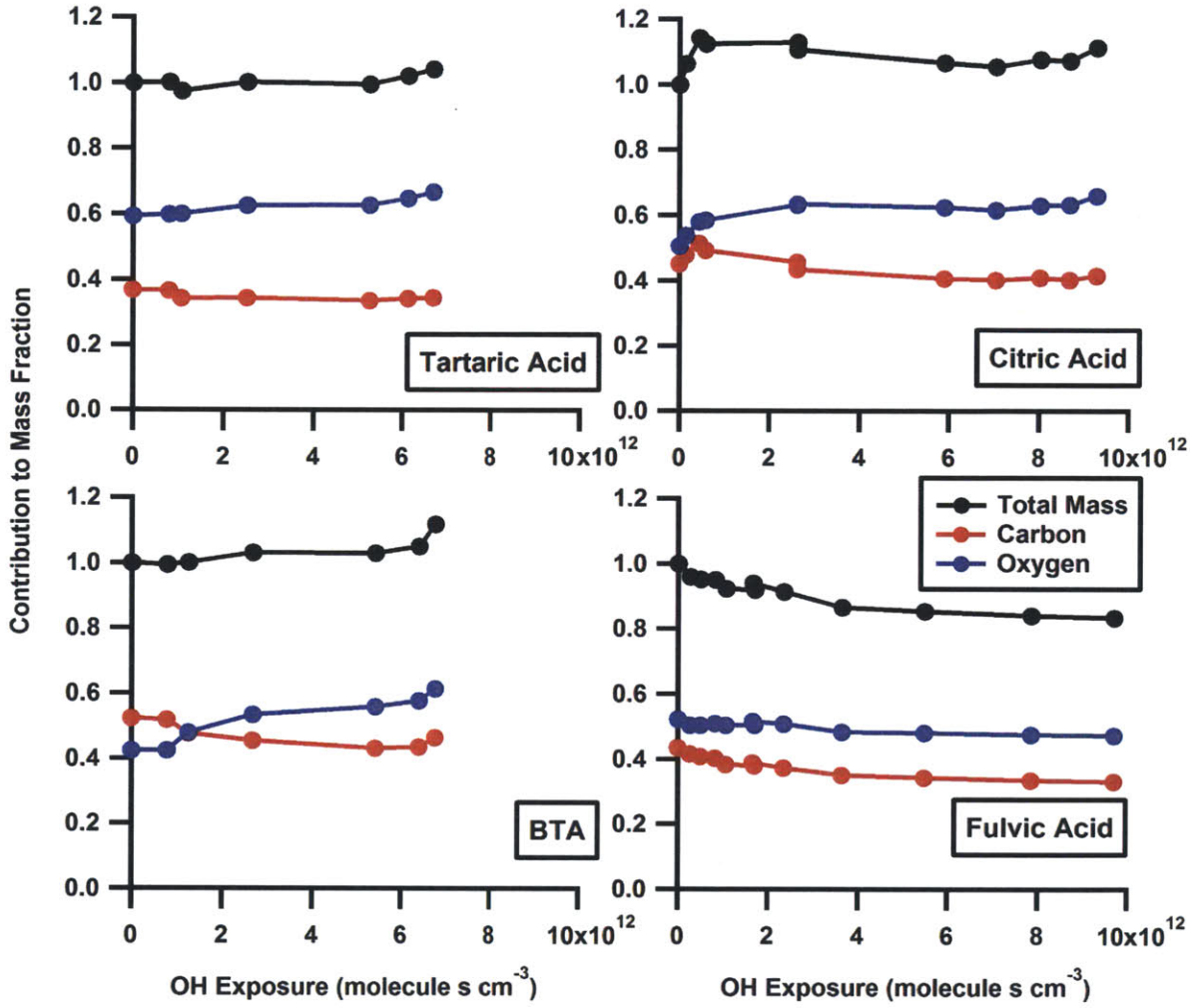

Figure 4.5: Fractional mass contribution of carbon (red) and oxygen (blue), and total mass fraction remaining per particle (black) for each of the four systems over the course of oxidation. The x-axis in each plot is an effective OH exposure, adjusting to a mean particle diameter of 200 nm in each system. Total mass in each pure component system (not counting the fulvic acid mixture) remains unchanged within observation error, as the loss of carbon is offset by an approximately equivalent increase in oxygen.

least oxidized species (squalane, a saturated alkane) initially does not undergo any volatilization upon oxidation, due to the dominance of functionalization over fragmentation reactions [13]. As it gets more oxidized, however, further oxidation leads to significant loss of carbon (and total particle mass). This trend is also seen for the moderately oxidized species, erythritol and levoglucosan, which exhibit the most rapid volatilization. However, for the most oxidized species (the polycarboxylic acids examined in this work), carbon loss is restricted over the course of the experiment to no more than $\sim$20%. This may be because fragmentation processes which otherwise contribute strongly to volatilization [13] either are less favored during oxidation or, more likely, produce fragments that are sufficiently low in volatility that they remain in the condensed phase. Furthermore, the loss of carbon for the most oxidized species is typically offset by an equivalent increase in oxygen, so that the overall process approximately conserves particle mass. Atmospheric oxidation of the most oxidized organic aerosol is therefore unlikely to be a significant sink of aerosol mass, though it is still capable of transforming the chemical composition—and therefore key properties such as hygroscopicity [11, 33, 34, 2, 35] and refractive index [11]—of the particles over their atmospheric lifetimes.

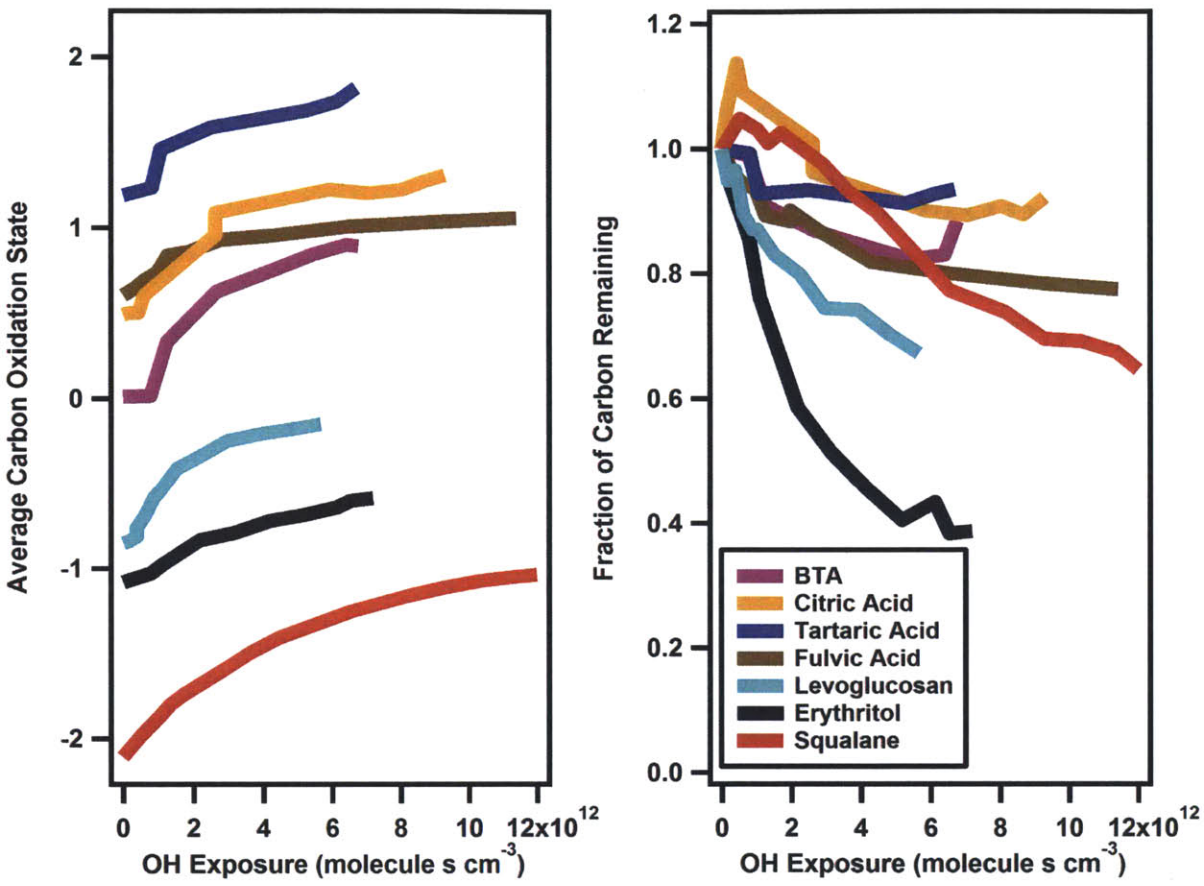

Figure 4.6: Summary of heterogeneous oxidation experiments. (A) Average carbon oxidation state as estimated from AMS elemental analysis [58] during the course of oxidation for squalane, erythritol, levoglucosan, and the systems introduced in this work. For consistency the same elemental analysis correction factors [29] are applied in all cases, and OH exposure is adjusted for a particle diameter of 200 nm (as in Figure 4.5). In general, there is an initial increase in oxidation state, at approximately the same rate, regardless of the system studied. (B) Estimated carbon loss, which serves as a measure of volatilization, for the same seven systems. Squalane, a reduced compound, undergoes moderate carbon loss. The moderately oxidized species, erythritol and levoglucosan, lose a much larger proportion of initial carbon to the gas phase, probably due to increased fragmentation reactions. On the other hand, the most oxidized species (the acids examined in the present study) experience only mild volatilization, possibly because fragmentation products are so low in volatility that they remain in the condensed phase.

Chapter 5

Formation of Secondary Organic Aerosol by Direct Photolysis of Gas-Phase Iodide Species

In this work so far, we have made a point of underscoring the chemical complexity inherent in reacting systems, but we have not yet addressed the oxidative mechanisms that give rise to such complexity in the atmosphere. Most experimental studies of the products of atmospheric organic reactions, including secondary organic aerosol (SOA) and the experiments outlined in Chapters 3 and 4, involve the oxidation of a single model compound or mixture of compounds by exposure to an atmospheric oxidant over some amount of time [18, 23, 14, 26, 27], in each of these cases by the hydroxyl radical (OH). However, the high reactivity of OH can confound laboratory studies of chemical mechanisms, since multiple and sequential oxidative steps are possible during a single experiment. Presented in this chapter is an experimental system designed to limit oxidation processes to a single generation of products formed from a single radical precursor. In lieu of the abstraction of a hydrogen atom by OH, we use a photolabile precursor to generate SOA. Although this technique is commonly employed to study the kinetics and products of simple gas-phase reactions, e.g. [82], to our knowledge it has not been used in the explicit study of SOA formation chemistry.

The immediate product of the reaction of a hydrocarbon with OH is typically an alkyl radical, which in turn reacts rapidly with ambient oxygen to form the peroxy radical, RO_2 [76]. Peroxy radicals may subsequently react with NO or with other peroxy species to yield a distribution of products, each of which is free to react again with OH and form a new set of products. By

using photolabile compounds-in this case, a series of n-alkyl iodides-the bimolecular hydrogen abstraction step is bypassed during the formation of the initial alkyl radical, as demonstrated in Figure 5.1. In this manner, a single radical species is formed, in marked contrast to reactions that are initiated by reaction with OH. Secondary organic chemistry involving the iodine photofragment is predicted to be minimal, as the C-I and H-I bonds are weak enough to make their formation energetically unfavorable [16, 83].

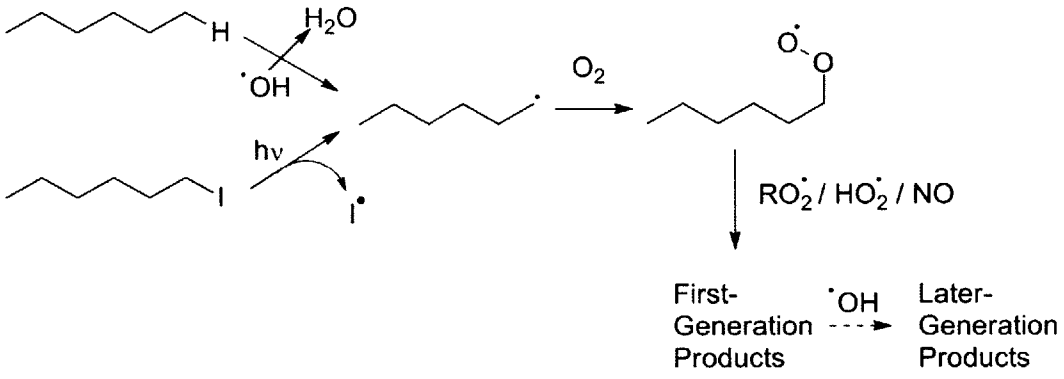

Figure 5.1: Simplified mechanism of alkane oxidation chemistry. In the atmosphere-and in most experimental studies-alkyl radicals are formed by abstraction of a hydrogen atom from any site on the carbon backbone by OH (top pathway); in this study, radicals are instead formed in a more controlled manner and at a determined site on the carbon backbone by the photolysis of alkyl iodides (bottom pathway). First-generation oxidation products will react further in the presence of OH, whereas stable products of the photolysis pathway are less likely to react further.

5.1 Methods

In the experiments presented here, gas-phase 1-octyl, 1-decyl, or 1-dodecyl iodides (98% purity, Sigma-Aldrich Co.; hereafter referred to as the C_8, C_{10}, and C_{12} systems, respectively) were introduced to a flow tube reactor, with a carrier flow of synthetic air. Oxidation was initiated by irradiation by 254-nm light (which is near the absorption maximum for alkyl iodides [84]). In the absence of either light or gas-phase alkyl iodides, no particle formation is observed. However, when the precursor species is introduced to the irradiated

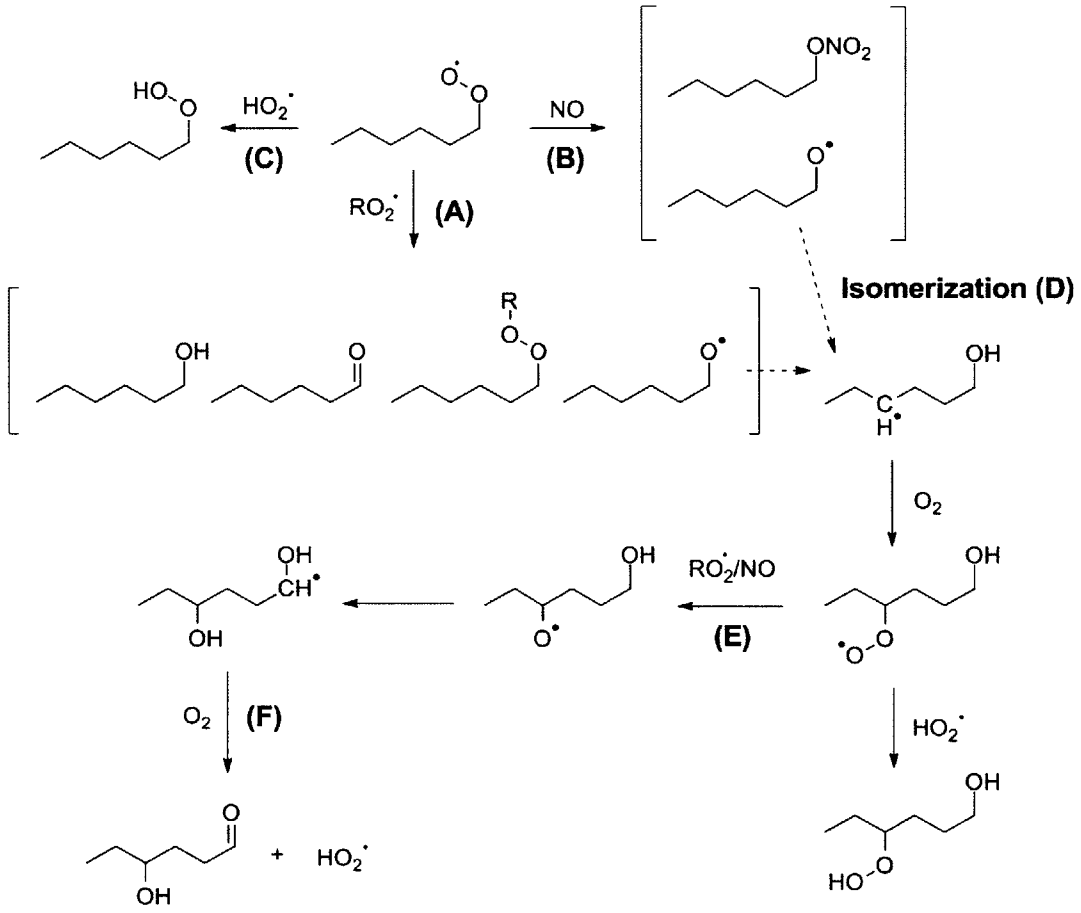

Figure 5.2: Common reaction pathways of alkylperoxy radicals under atmospheric conditions.

tube, particle formation and growth is observed to occur rapidly.

Experiments were carried out in a flow reactor, which has been described previously in detail [13, 14, 26, 27] and is modified for oxidant-less reactions in this case. The reactor is made up of type-219 quartz, with a length of 130 cm and inner diameter of 2.5 cm. The effective residence time—defined by the section of the reactor exposed to 254-nm UV light from the pair of external mercury lamps—is ~37 s. Four streams were mixed before entering the flow tube reactor: 1) 200 sccm pure O_2, 2) 30 sccm hexane (5 ppm) in N_2, 3) a variable flow rate of N_2, which is passed through a bubbler containing liquid organic iodide (98% purity, Sigma-Aldrich Co.), and 4) a makeup flow of dry N_2, such that the total flow rate in the reactor is 1 slm. Concentrations of alkyl iodides are not measured directly, but are instead estimated from known vapor pressures [85], assuming the air from the bubbler is saturated in iodine species. Concentrations range from 240 ppb to 120 ppm. The hexane is used as a tracer for OH; concentrations did not change when the lights were turned on, indicating negligible OH-initiated secondary chemistry. Approximately 97% of the precursor is assumed to be photolyzed in the reactor, based on estimates of the photolysis rate constant from an absorption cross-section of 10–18 cm^2 and a photon flux of 8×10^{-4} W cm^{-2}. The quantum yield is assumed to be unity for the sake of a conservative estimate. Particle formation occurs spontaneously within the reactor, with no need for added seed nuclei.

5.2 Discussion

As with standard chamber experiments regarding SOA generation, aerosol growth is dependent on total aerosol loading, indicating that particulate organic species are semi-volatile. Following Odum et al. [17] and Donahue et al. [22], the partitioning of the product mixture was modeled using a set of representative semi-volatile products of varying volatility:

$$Y = \frac{\Delta C_{OA}}{\Delta C_R} = \sum_i \alpha_i \left(1 + \frac{C_i^*}{C_{OA}}\right)^{-1} \tag{5.1}$$

where Y is the organic aerosol mass yield, C_{OA} is the mass concentration of particulate organics, ΔC_R is the decrease in mass concentration of the gas-phase reactive species, and α_i and C_i^* are, respectively, the product yield and saturation concentration of product "i."

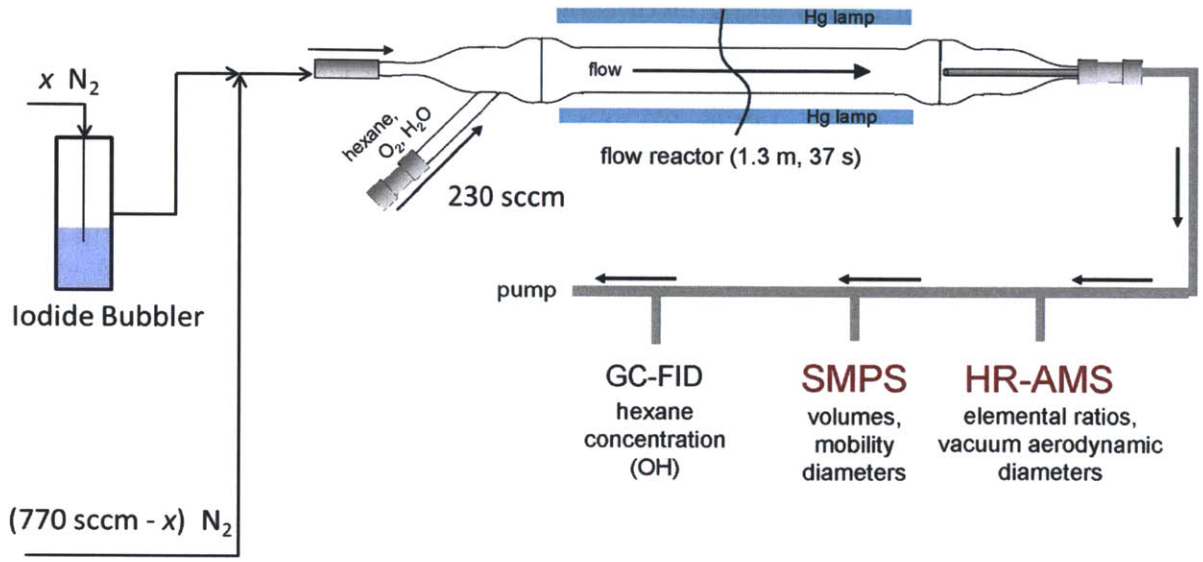

Figure 5.3: Experimental setup for iodide photolysis and secondary organic aerosol generation. Nitrogen is bubbled through liquid alkyl iodide, such that the exiting gas is saturated in organic compound before being diluted by the makeup gas and entering the flow reactor.

The mass yield of organic aerosol is calculated relative to the concentration of the precursor species after subtracting the mass of the iodide atom. This subtraction is performed in order to facilitate comparison of the observed aerosol yields with those reported for oxidation of n-alkanes [86]. This value is plotted against the total aerosol mass loading for the C_8, C_{10}, and C_{12} systems in Figure 5.4. As expected, the precursor species with higher molecular weights exhibit increased aerosol yields, due to the lower volatility of the oxidation products. The data in each set is fitted to the volatility basis set (Equation 5.1) using two volatility bins ($C_1^* = 100$ μg m^{-3} and $C_2^* = 1000$ μg m^{-3}) for the range of C_{OA} studied [22]. Fits using a larger number of bins gave values of α_i that were statistically insignificant (i.e. indistinguishable from zero) or unphysical (negative). Fitted product yields are shown in Table 5.1 for each of the three systems. Most of the product mass is observed in the higher-volatility bin, such that a single generation of oxidation is unlikely to produce SOA in significant yields at atmospherically relevant aerosol loadings. This is consistent with previous studies that indicate the importance of multiple oxidation generations in the formation of SOA from alkanes, especially for shorter hydrocarbon chains [86, 87]. Additionally, the yields observed here are

approximately one-half of those previously observed in chamber experiments of comparable alkane oxidation systems [86]. This lower yield is indicative of higher overall volatility among oxidation products; this may result from the limited number of allowed reactions, differences in RO_2 chemistry (e.g. RO_2+RO_2 vs. RO_2+NO reactions), or possible differences between the chemistry of primary alkylperoxy radicals (used here) and secondary radicals (which are more commonly encountered in normal alkane oxidation by OH).

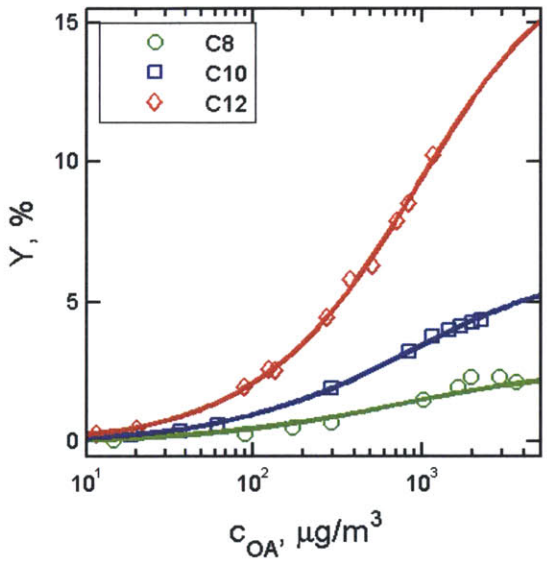

Figure 5.4: Adjusted organic aerosol mass yields versus total particle mass loading for the C_8, C_{10}, and C_{12} systems. Trend lines are generated using a two-parameter fit to a volatility basis set, as shown in Equation 5.1 and Table 5.1.

Chemical characterization of product aerosol mixtures was obtained from a high-resolution Aerosol Mass Spectrometer (AMS, Aerodyne Inc.), which was operated alternately in electron impact (EI) mode (with the vaporizer set at 600 °C) or in vacuum-ultraviolet single-photon ionization (VUV-SPI) mode, operating at 10.5 eV and with the vaporizer set at 100 °C [14].

The high resolution of the mass spectrometer and high degree of fragmentation in EI mode enable the estimation of elemental ratios of hydrogen to

Reactive Species	$C_8H_{17}I$	$C_{10}H_{21}I$	$C_{12}H_{25}I$
α_1, %; ($C_1^* = 100\mu$g m^{-3})	0.6 ± 0.5	1.0 ± 0.3	1.1 ± 0.5
α_2, %; ($C_2^* = 1000\mu$g m^{-3})	1.9 ± 0.6	5.1 ± 0.5	16.8 ± 1.2
O/C range	0.12 to 0.13	0.083 to 0.10	0.07 to 0.10
H/C range	1.92 to 1.94	1.97 to 2.02	1.85 to 2.05
# Oxygen per carbon chain	0.99 to 1.07	0.83 to 1.0	0.80 to 1.2

Table 5.1: Product yields from a two-parameter fit to Equation 5.1, using the two indicated values of C_i^* to define the volatility bins, and ranges of calculated elemental ratios (oxygen-to-carbon, O:C, and hydrogen-to-carbon, H:C) for all samples with a mass loading of at least 1 μg m^{-3}. The number of oxygen atoms per contiguous carbon chain is also estimated as the value of O:C times the number of carbon atoms in the parent molecule. Elemental ratios given are expected to have a 95% confidence interval of ±30% of the given value for O:C and ±10% for H:C [29].

carbon atoms (H/C) and oxygen to carbon atoms (O/C), which are summarized in Table 5.1, using the method described by Aiken et al. [29, 30]. Figure 5.5 shows a sample EI mass spectrum for each of the C_8, C_{10}, and C_{12}-derived aerosol mixtures. Mass spectra are dominated by ions of the form $C_xH_y^+$, though oxygenated fragments ($C_xH_yO_z^+$, $z = 1, 2$) are also present. The relative presence of oxygenated fragments declines as the precursor molecular weight increases, due to an increase in the total number of carbon atoms per molecule. A small amount of particle-phase iodide (I^+ and HI^+) also appears in this spectrum (accounting for less than 2% of the total ion signal in all systems), although there are no peaks of the form $C_xH_yO_zI^+$. This suggests that the observed iodine presence comes from inorganic products (e.g. I_xO_y crystals), which have been observed in similar systems [88]. We therefore conclude that the organic aerosol formed is primarily due to chemistry of the alkyl photofragment, with little to no influence from subsequent iodine chemistry.

The measured O/C values of the aerosol (Table 5.1) are lower than those measured in chamber studies of SOA from the OH-initiated oxidation of alkanes [86], again suggesting the importance of multiple generations of oxidation in those systems. The number of oxygen atoms per contiguous carbon chain, determined by multiplying O/C by the number of carbon atoms in the precursor molecule (and assuming no reactions break or form C-C bonds), indicate that, on average, only one O atom is added per contiguous carbon chain. While such a low degree of oxidation is expected, as only one oxidation step is accessed in these experiments, the identity of the low-volatility species observed

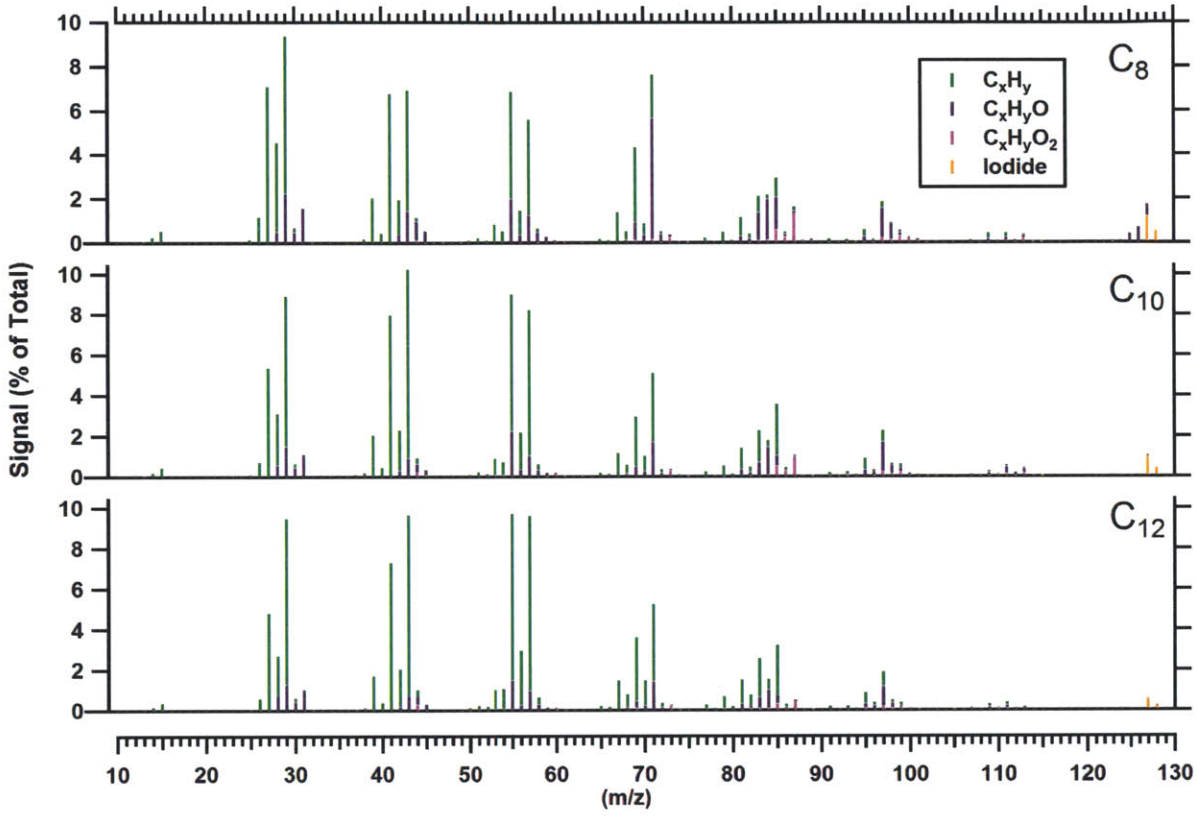

Figure 5.5: Sample electron-impact mass spectra of C_8, C_{10}, and C_{12} aerosol, taken from the highest range of concentrations in each experiment and normalized by the total signal. Sticks are colored according to oxygen content of fragments as measured by high-resolution peak-fitting. Fragments at $m/z = 127$ and $m/z = 128$ are I^+ and HI^+, respectively. Peaks with $m/z > 130$ account for a very minor fraction (less than 4%) of the total organic AMS signal.

must be reconciled with the apparently low number of polar functional groups. For example, even for dodecanol—one of the lowest-volatility C_{12} compounds to have only one oxygen—the expected saturation concentration is $\sim 10^4$ μg m^{-3}, at least an order of magnitude greater than what is needed to produce the mass yields observed here [89]. It therefore appears that a significant fraction of the aerosol is composed of compounds of higher molecular weight, possibly formed by oligomerization processes. For instance, a $C_{12}OOC_{12}$ peroxide (formed by combination of two dodecyl peroxy radicals) has an expected saturation concentration of $\sim$50 μg m^{-3}, which is sufficient to contribute to SOA in the yields observed. Other potential formation mechanisms of low-volatility, slightly oxidized species are described below. It should be noted that the actual oxygen content might be somewhat greater than what is estimated here, due to uncertainties in the O/C parameterization; such uncertainties may be especially large in this case because the measured product mixture is limited to a small number of individual species [29].

AMS measurements were also carried out using VUV-SPI, a "soft" ionization technique involving a lower degree of fragmentation than in EI and therefore improved determination of molecular species. Figure 5.6 shows representative VUV mass spectra from the C_8, C_{10}, and C_{12} experiments, with the dominant peaks occurring at higher values of m/z than in the EI spectra. The spectra are reasonably complex and are dominated by ions with odd-numbered masses, indicative of molecular fragments. This is not typical of VUV spectra of organic aerosol, which tend to show molecular (even-mass) peaks [14, 90, 91]. This suggests that the present chemical system may contain weakly-bound and/or easily photoionized species, such as organic peroxides [92].

Major peaks in each VUV mass spectrum are clustered about $m/z = 127$ ($C_8H_{15}O^+$), 155 ($C_{10}H_{19}O^+$), and 183 ($C_{12}H_{23}O^+$), respectively, which correspond to the mass of the main carbon chain, with one oxygen atom added and two hydrogen atoms lost (in addition to the loss of the iodine; high-resolution analysis confirms these assignments, as the I^+ ion contributes less than 1% to the total ion signal at $m/z = 127$). The mass differences ($\Delta(m/z) = 28$) between these peaks are consistent with the differences between the molecular weight of the precursor species. Other significant peaks at ± 2 amu may indicate various degrees of (un)saturation of the organic species being observed. The higher-mass clusters correspond to ions with multiple oxygen atoms; these minor species again suggest the presence of isomerization and chain-propagation products.

Shown in Figure 5.7 are the major reactive pathways available to RO_2 radicals formed in the simple chemical system studied here (n-alkyl iodides + 254-nm light + air), with product yields estimated from a simple kinetic model (described in Section 5.3). The initial radical chemistry is straightforward: the alkyl radicals (R) react with oxygen to form alkylperoxy radicals (RO_2), which mostly react with other RO_2 radicals (Reactions of alkyl and alkoxy radicals with other organic species are negligible). RO_2+RO_2 chemistry may lead to the formation of low-volatility peroxides of the form ROOR [93, 94, 95]. Other major RO_2+RO_2 products include alkoxy radicals; these can isomerize to hydroxycarbonyls, which may themselves isomerize and dehydrate to form low-volatility dihydrofuran species [86]. This pathway also generates HO_2, which will react with RO_2 radicals to form hydroperoxide species (accounting for more than 25% of the RO_2 reaction). ROOH species are not low enough in volatility to condense into the particle phase, but they may react with carbonyls to generate low-volatility peroxyhemiacetals [96]. The formation of these various low-volatility species-dialkyl peroxides, dihydrofurans, and peroxyhemiacetals-may explain the formation of aerosol with relatively low oxygen content. Moreover, the formation of these products also may explain the relatively complicated VUV-MS spectra shown in Figure 5.6 simply by providing a larger-than-expected number of products that are capable of fragmentation at lower temperatures and photon energies than the hydrocarbons previously studeid [14]. This observation underscores the substantial chemical complexity of SOA, even when secondary reactions and multigenerational oxidation are heavily suppressed.

Although the chemical complexity of the organic mixture may inhibit identification of individual species by the methods used here, bulk measurements of total aerosol concentration and elemental ratios are nonetheless aided greatly by the resolution of generational complexity provided by direct photolytic initiation of the oxidation step, which can be applied to systems with novel photolabile precursors (which would most likely be synthesized in the laboratory) for more targeted experiments. Also, in the atmosphere, RO_2 will mostly react with NO and HO_2, which may lead to the formation of aerosol with very different loading and composition [86, 21]. Introduction of such species will be the focus of future studies; the distribution of oxidation products may be further simplified in this system as RO_2 self-reaction becomes negligible.

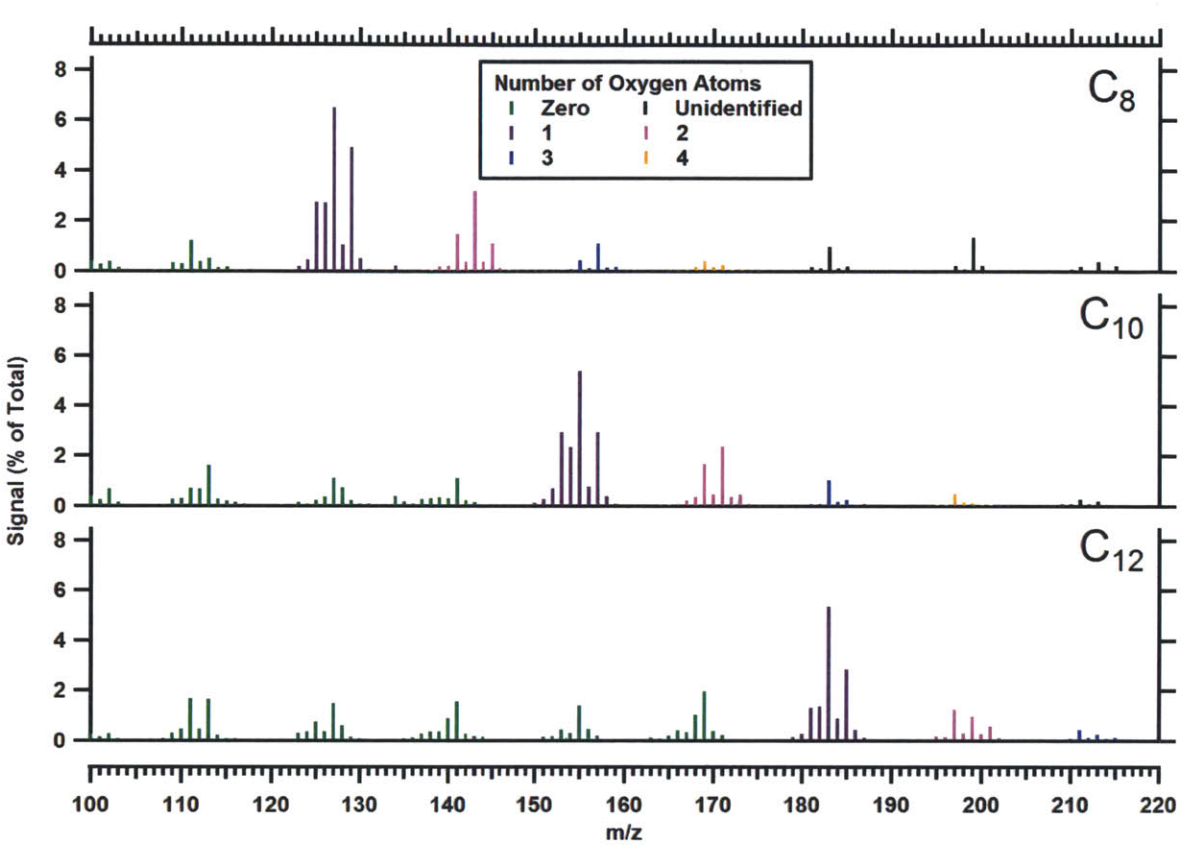

Figure 5.6: VUV mass spectra of the C_8, C_{10}, and C_{12} systems. The principal clusters of peaks in each case correspond to C_xO, with indications of more highly oxidized molecules at higher masses. The number of oxygen atoms in each cluster is confirmed by high-resolution analysis. Other peaks with $m/z > 220$ are measured, though they have not been positively identified; these ions, which presumably correspond to high-molecular-weight species (such as oligomeric peroxides), account for 18–30% of the total ion signal. Peaks with $m/z < 100$, which correspond to fragment ions, account for an additional 30–42% of the total ion signal.

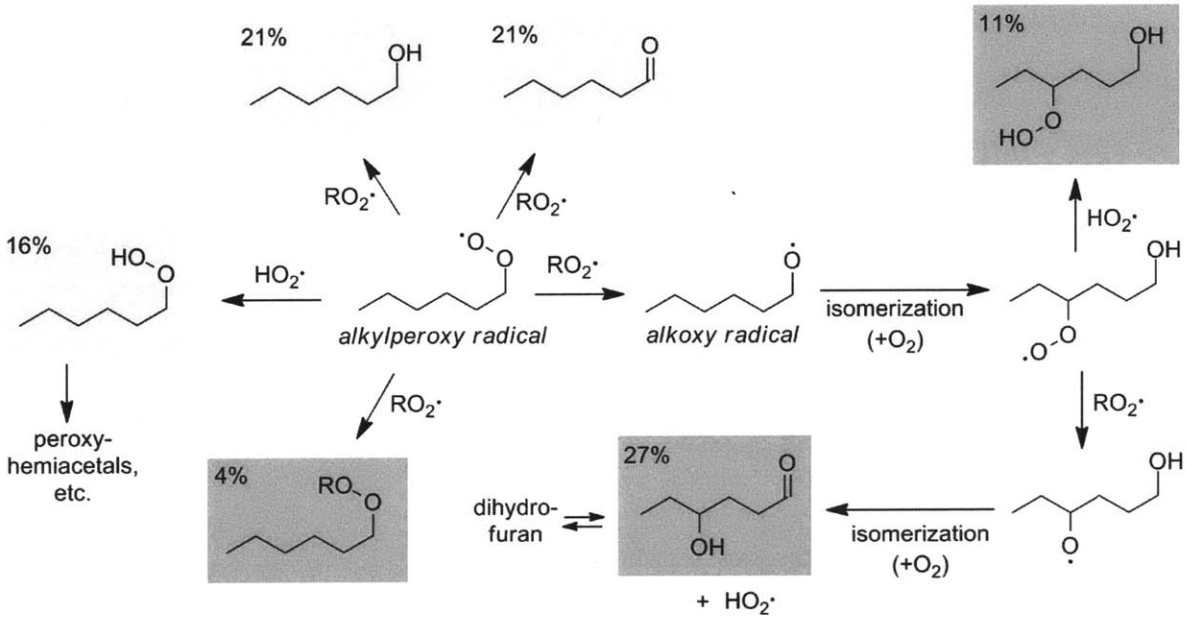

Figure 5.7: Expected reaction pathways for the alkylperoxy radical in this experiment. Although chemistry is initially dominated by RO_2+RO_2 self-reaction, the generation of hydroxycarbonyl species also produces HO_2, which is an important sink for the remaining RO_2. Stable molecules are indicated by shaded boxes, with the more-volatile species against light gray and the less-volatile ones against dark gray. Approximate molar product yields, estimated by a kinetic model (described in Section 5.3), are indicated in each box. Although peroxyhemiacetal and dihydrofuran products are not explicitly modeled, these products are sufficiently low in both volatility and oxygen content to agree qualitatively with the experimental results.

5.3 Kinetic Model of Iodide Photolysis

In order to examine the relative importance of various reaction pathways in the reactive systems studied in this chapter, we have performed a kinetic simulation of such reactions under the relevant experimental conditions. All reactions (and corresponding rate coefficients) used in this kinetic model are listed in Table 5.2. Self-reaction of RO_2 radicals leads to the production of alcohols, carbonyls, peroxides of the form ROOR, and alkoxy radicals (RO·) [14]. The alkoxy radical rapidly isomerizes and reacts with oxygen to form the hydroxy-alkylperoxy radical, which again engages in RO_2 self-reaction [86]. Reaction of the hydroxy-alkoxy radical with oxygen yields a hydroxycarbonyl compound

and HO_2; this radical will react with RO_2 to form hydroperoxides [86].

Secondary reactions, which may complicate the reactions described above, are also included in this kinetic model. These focus on the radical abstraction of the hydrogen atom from the parent iodide compound, RI, by alkyl, alkylperoxy, alkoxy, and hydroxyl radicals. The hydroxyl radical may be formed by the photolysis of either organic hydroperoxides (ROOH) or hydrogen peroxide (H_2O_2). Conservatively high rate coefficients for these side reactions are used as upper limits.

A 37-second simulation of the reactions (consistent with the residence time of the reactor) was performed for an initial concentration of RI of 6×10^{13} molecule cm^{-3} (consistent with the levels used in this experiment for dodecyl iodide), with the final concentrations of stable (non-radical) products given in Table 5.3. Species formed by the RO_2 self-reaction and RO_2+HO_2 channels are present at levels at least two orders of magnitude greater than those formed by reactions of the parent molecule with other radicals, which account for less than 1% of all reactions of RI. We are therefore confident that the observed chemistry arises from the R+O_2 reaction to form RO_2 radicals, followed RO_2+RO_2 and RO_2+HO_2 reactions.

#	Reaction	Rate Coefficient	Source
1	$RI \rightarrow R\cdot + I\cdot$	1.56×10^{-2}	[97, 98]
2	$R\cdot (+O_2) \rightarrow RO_2\cdot$	1.87×10^{4}	[65]
3	$RO_2\cdot + R'O_2\cdot \rightarrow ROOR' + O_2$	3.84×10^{-15}	[65]
4	$RO_2\cdot + RO_2\cdot \rightarrow RO\cdot + RO\cdot + O_2$	3.97×10^{-14}	[65]
5	$RO_2\cdot + RO_2\cdot \rightarrow ROH + R{=}O + O_2$	2.04×10^{-14}	[65]
6	$(\text{H-})RI + R\cdot \rightarrow \cdot RI + RH$	1.5×10^{-13}	[99]
7	$\cdot RI + O_2 \rightarrow RIO_2\cdot$	1.87×10^{4}	[65]
8	$R\cdot + R'\cdot \rightarrow RR'$	5.0×10^{-12}	[100]
9	$RO_2\cdot + (\text{H-})RI \rightarrow ROOH + \cdot RI$	3.90×10^{-19}	[100]
10	$RO\cdot (+O_2) \rightarrow R'(OH)\,R''O_2\cdot$	1.5×10^{7}	[101]
11	$R'(OH)\,R''O\cdot \rightarrow R'(OH)\,R''{=}O + HO_2\cdot$	4.7×10^{4}	[65]
12	$RO_2\cdot + HO_2\cdot \rightarrow ROOH + O_2$	7.7×10^{-12}	[65]
13	$ROOH \rightarrow RO\cdot + \cdot OH$	4.53×10^{-4}	[97, 102]
14	$HO_2\cdot + HO_2\cdot \rightarrow H_2O_2 + O_2$	2.84×10^{-12}	[103]
15	$H_2O_2 \rightarrow 2\cdot OH$	1.16×10^{-3}	[97, 104]
16	$2\,(\cdot OH) \rightarrow H_2O_2$	4.7×10^{-25}	[103]
17	$\cdot OH + HO_2\cdot \rightarrow H_2O + O_2$	1.1×10^{-16}	[103]
18	$\cdot OH + (\text{H-})RI \rightarrow \cdot RI + H_2O$	1.1×10^{-18}	[65]

Table 5.2: Reactions and rate coefficients used in a simplified photolytic oxidation scheme. Pseudo-first-order rate constants (reactions 1, 2, 7, 10, 11, 13, and 15, assuming a constant 20% O_2 presence) are in units of s^{-1}, while all other rate constants have units of cm^3 $molecule^{-1}$ s^{-1}. Photolysis rates are estimated by comparing the absorption cross-sections of ozone (1.13×10^{-17} cm^2 [97]) with those of methyl iodide (1.11×10^{-18} cm^2 [98]), methyl hydroperoxide (3.23×10^{-20} cm^2 [102]), and hydrogen peroxide (6.7×10^{-20} cm^2 [104]), as well as a previously-estimated photolysis rate coefficient of ozone of 0.159 s^{-1} in the flow reactor. Quantum yields in all cases are assumed to be unity in order to provide an upper limit on the reaction rate of RI. Rate coefficients for the self-reaction of alkyl radicals and for H-abstraction by the peroxy radical are estimated from condensed-phase studies [100], adjusted upwards by a factor of 50 in order to provide a credible upper limit for the calculated rate by accounting for the increased collision frequency between dissimilar compounds. The hydroxyalkyl radical formed by isomerization in reaction 10 is assumed to immediately form an alkylperoxy radical by reacting with abundant O_2. Subsequent reactions with other radical species are as described in reactions 3, 4, 5, and 12. Additionally, reaction 11 has O_2 as an implied reactant, which does not affect the pseudo-first-order rate constant.

#	Species	Final Concentration (Fraction of Initial RI)
1	RI	0.011
2	RH	5.4×10^{-12}
3	ROOR'	0.037
4	ROH	0.196
5	R=O	0.196
6	R-R'	2.3×10^{-25}
7	R(OH)R(=O)	0.252
8	ROOH	0.152
9	R(OH)ROOH	0.096
10	H_2O_2	2.8×10^{-4}

Table 5.3: Final concentration values of stable (non-radical) species, as a fraction of the initial concentration of RI, for a simulation of the kinetics described in Table 5.2. The reaction time is estimated to be ~37 s (the residence time of the flow reactor used here), and the initial concentration of species RI is given as 6×10^{13} molecule cm^{-3}. Approximately 5% of the total organic signal is estimated to be in remaining radical (alkylperoxy and alkoxy) species, which are not listed here.

Chapter 6

Aging of Photolytically-Generated Secondary Organic Aerosol

So far, the topics of heterogeneous oxidation of organic aerosol and photolytic chemistry of aerosol-forming species have been approached as two separate subjects. This last unit focuses on a synthesis of the two subjects, with a general objective of demonstrating the potential utility of introducing direct photolytic processes to a wider range of organic aerosol studies and a more particular goal of obtaining evidence for novel chemical reactions and condensed-phase products that are often overlooked by current state-of-the-art atmospheric models.

Several drawbacks exist to the traditional single-component heterogeneous oxidation procedure as outlined in Chapters 3 and 4. Because oxygenated compounds often tend to exist in a cyrstalline phase when not mixed with other organic species, the issue of phase change must be addressed for high levels of oxidant exposure and sufficiently long reaction times [77]. Additionally, there is no guarantee that a given compound (or even group of compounds) will on its own sufficiently encompass the physical and chemical properties of the system we are attempting to study.

In our own experiments, we wish to replicate the atmospheric conditions of SOA formation—including particle size and phase, as well as approximate mixture properties—while at the same time maintaining the relatively tractable small number of starting compounds afforded by pure-species heterogeneous oxidation. For this purpose, the utility of the photolytic SOA experiment described in the previous chapter can be demonstrated most clearly in Figure

6.1, which compares the VUV mass spectrum of dodecyl iodide SOA with that of SOA formed from the reaction of gas-phase dodecane with hydroxyl radicals, OH. Whereas the alkane + OH system yields a busy spectrum with many small fragments (caused either by a wider array of oxidation reaction products or by a higher degree of fragmentation in the AMS for more oxygenated compounds [14]), the spectrum for alkyl iodide photolysis shows just a handful of significant peaks, which correspond generally to identifiable compounds.

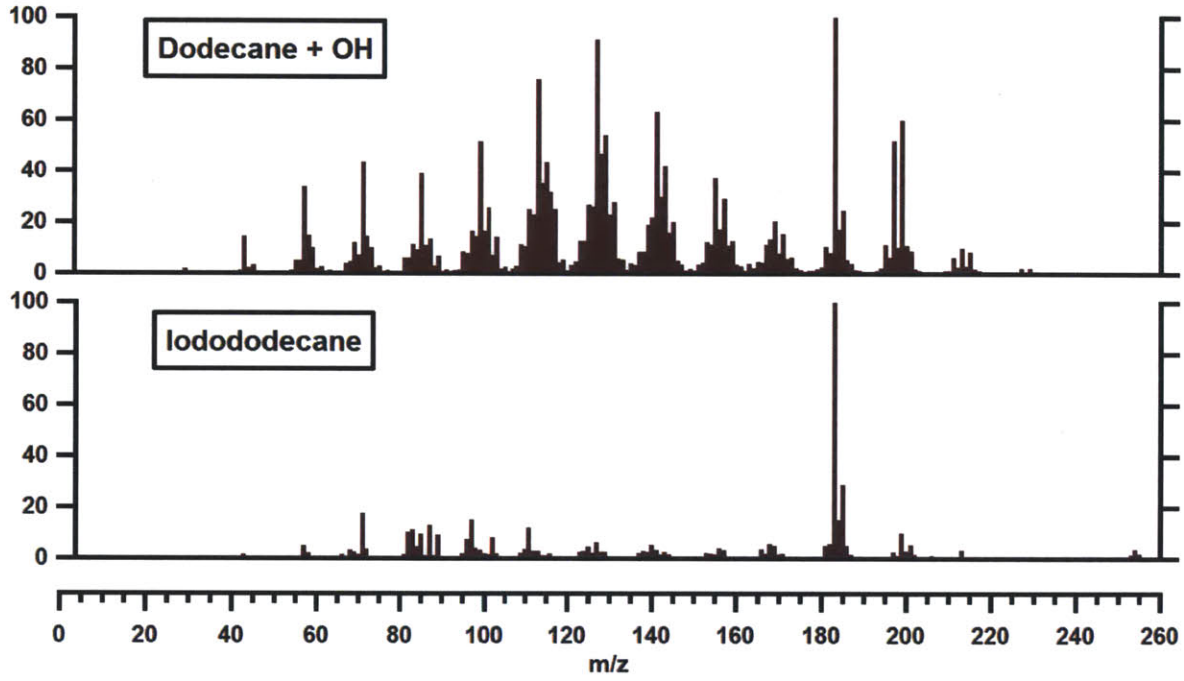

Figure 6.1: (Top) VUV mass spectrum of SOA generated from the exposure of pure dodecane to OH. (Bottom) VUV mass spectrum of SOA generated from the photolysis of dodecyl iodide, with a much smaller degree of fragmentation. Peaks at $m/z = 183$ and $m/z = 185$ correspond to $C_{12}H_{23}O^+$ and $C_{12}H_{25}O^+$, respectively, which may arise from the photolysis of $C_{12}H_{25}OOC_{12}H_{25}$ or from the loss of a hydrogen atom from dodecanal and dodecanol, respectively.

In this work, we examine the aging of the dodecyl iodide SOA system by the heterogeneous oxidation method outlined previously. We then compare the results of this aging process both with the results of the single-component studies and with the further oxidation of the straightforward dodecane + OH SOA system. We intend to show that the results make a strong case for closer

inspection of specific features of typical aging experiments, and we discuss the atmospheric implications of these findings.

6.1 Methods

Photolytic SOA is generated by the method detailed in the previous chapter (and as demonstrated in Figure 6.2), by bubbling N_2 through pure liquid-phase dodecyl iodide, followed by photolysis at 254 nm in a flow tube with a diameter of ~1 in and a residence time of ~37 s. The aerosol mixture exiting the flow tube reactor passes through a charcoal denuder to remove most gas-phase species from the flow, while condensed-phase species evaporate slowly enough to prevent noticeable losses of particles. The flow exiting the denuder is then mixed with ozone and introduced to a second reactor, with the same dimensions as the first, where a second set of 254-nm lights initiates the formation of hydroxyl radicals in the same manner as in our heterogeneous oxidation experiments for single-component systems. Once again, OH exposure is controlled by altering the amount of ozone introduced to the reactor, with the residence time in the reactive region fixed at ~37 s.

In the dodecane + OH system, liquid dodecane is injected by a microliter-scale syringe pump at a rate of 2 μL hr^{-1} into a nitrogen flow prior to entering the flow tube. Hydroxyl radicals are again generated via the photolysis of ozone. Oxidant concentrations are increased to a level comparable with the exposures used in aging the dodecyl iodide SOA, roughly equivalent to 2–3 weeks of aging in the atmosphere.

6.2 Results

The relative presence of carbon remaining in the C_{12} aerosol, plotted against OH exposure (Figure 6.3), shows that the SOA mixture reacts readily with hydroxyl radicals according to the same patterns that were observed for squalane aging [13]. The observation of continuing carbon loss with a plateau in the addition of oxygen is consistent with earlier results observed in the oxidation of squalane as well. The overall mass change is initially small, as the loss of carbon is offset by the addition of new oxygen. Additionally, the rate of reaction is comparable to those earlier systems, and the initial reactants (as detected by VUV-MS) decay more thoroughly, with only ~10% remaining by

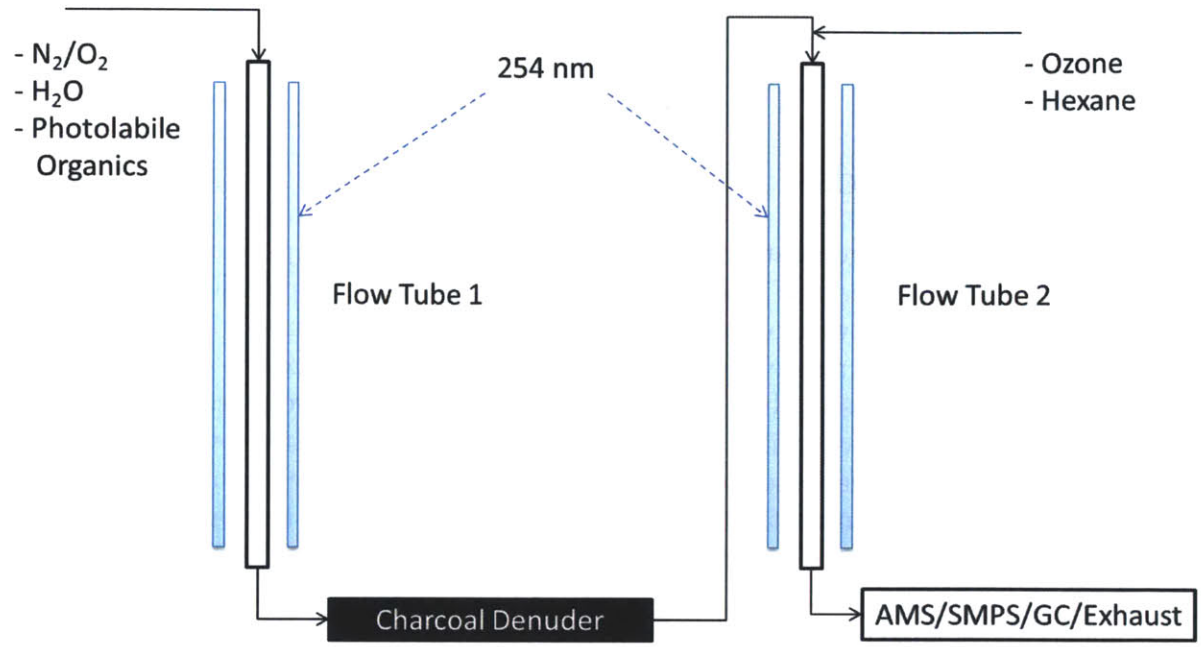

Figure 6.2: Experimental setup for the generation and aging of photolytic secondary organic aerosol.

an exposure of 4×10^{12} molecule s cm^{-3}, compared with a remainder of ~20% at much higher exposures in the erythritol and levoglucosan systems [26].

Figure 6.4 provides the changes in $\overline{OS}_C$ and the relative carbon abundance in the dodecyl iodide SOA upon reaction in the flow tube, both of which are superimposed upon the traces previously depicted in Figure 4.6. The rate of increase of the degree of oxidation is higher than for the pure compounds previously studied, and the rate of carbon loss is very rapid as well.

Lastly, as observed in Figure 6.5, the overall elemental composition of the system, as described by the O/C and H/C values, changes very dramatically over a relatively small range of oxidant exposures. The trajectory within the Van Krevelen space is very similar to the trajectory for the oxidation of squalane (the underlying set of gray points) and is consistent with the approximate one-to-one ratio of hydroxyl and carbonyl group addition to the carbon backbone, while the uptake rate appears to be within the same range as observed for squalane particles (0.3–0.5). By comparison, the same trajectory for the dodecane + OH experiment results in a much lower level of oxygen

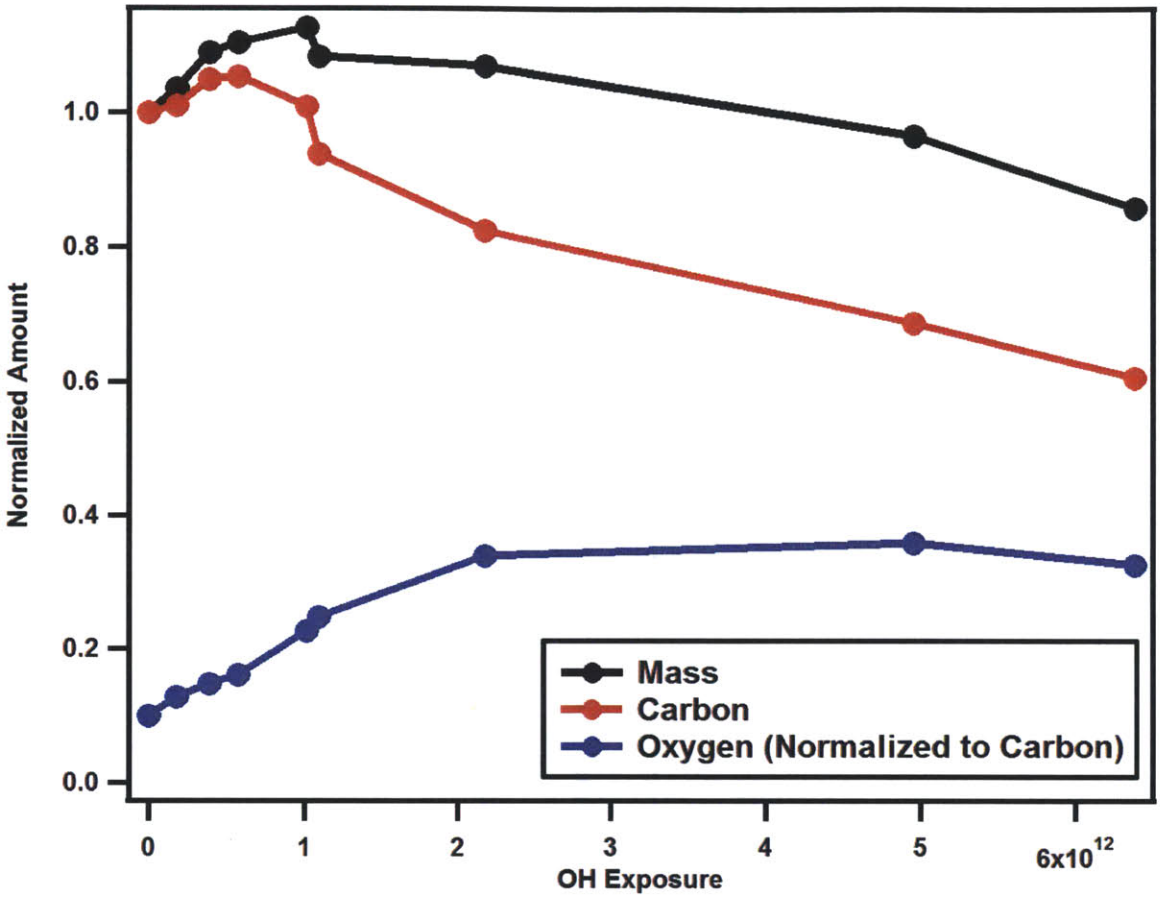

Figure 6.3: Normalized amount of carbon and oxygen detected in the C_{12}-derived organic aerosol.

addition, even at comparable levels of OH exposure.

Several possible explanations, both physical and chemical, could account for the discrepancy between the photolytic and traditional SOA systems in regards to aging by hydroxyl radicals. Because photolysis of dodecyl iodide yields exclusively a primary dodecyl radical—whereas abstraction of a hydrogen atom from dodecane is most likely to yield a mixture of secondary radicals—the range of condensed phase products may be significantly different between the two types of aerosol (This finding has been suggested by personal communication from others in the group, which have produced varying aerosol yields from alkoxy radicals at the primary and secondary carbon positions). Additionally, because gas-phase reactions are likely to be much faster than

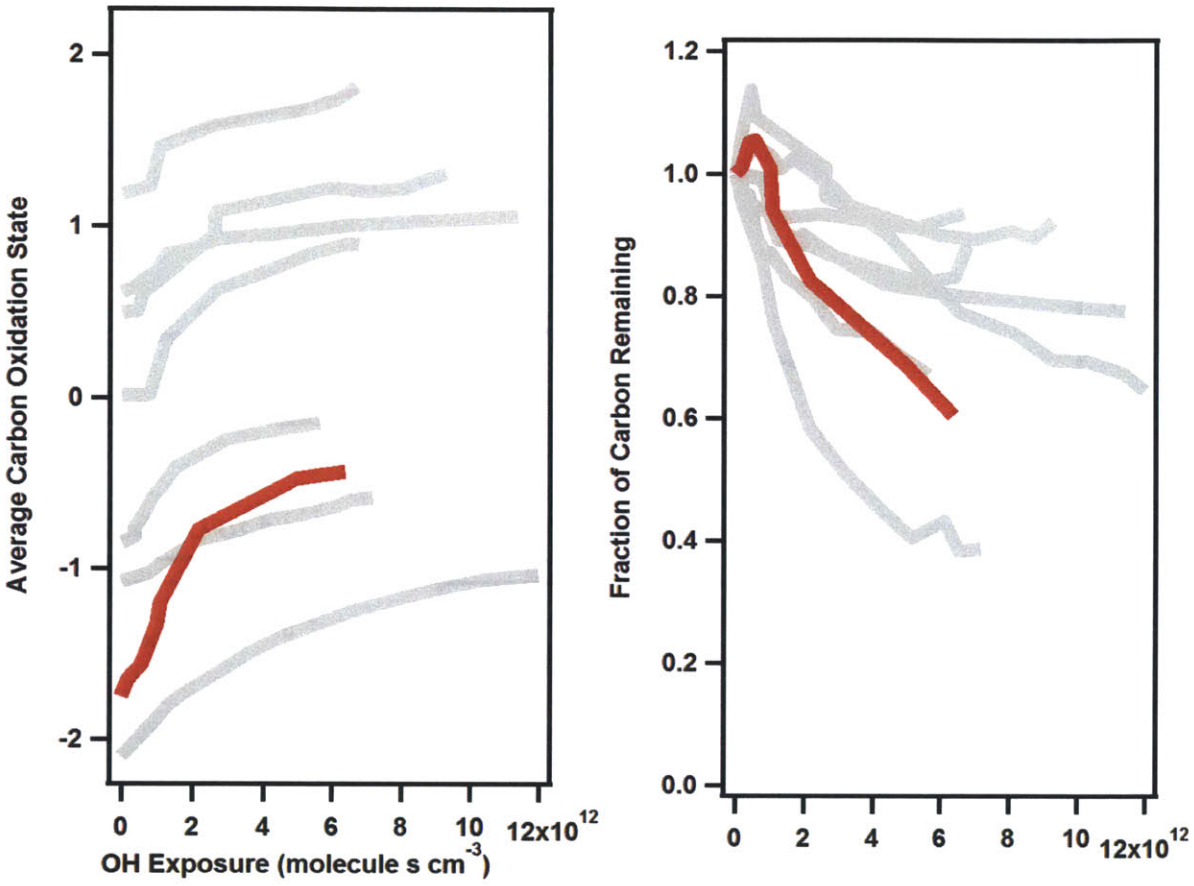

Figure 6.4: Summary plots of the changing average carbon oxidation state (left) and normalized particulate carbon mass (right) for the aging of dodecyliodide SOA (red) as compared with all previous heterogeneous oxidation experiments (gray).

condensed-phase reactions, rapid oxidation of gas-phase dodecane may lead to heavy fragmentation before the oxidized compounds have sufficient time to condense onto particle surfaces. Lastly, the phase in which the oxidation reactions themselves occur may affect the types of products from any given step (whether through solvation effects or via secondary reactions between organic species), such that heterogeneous reactions lead more quickly to the formation of OOA.

We therefore have evidence that the photolytically generated SOA is aged more readily than other model systems, representing both primary and secondary sources, in part because the compounds contained in the particle phase have relatively high hydrogen content, and partly because the phase of the particles themselves may be more liquid-like in the formation of SOA, thereby leading to greater uptake of OH.

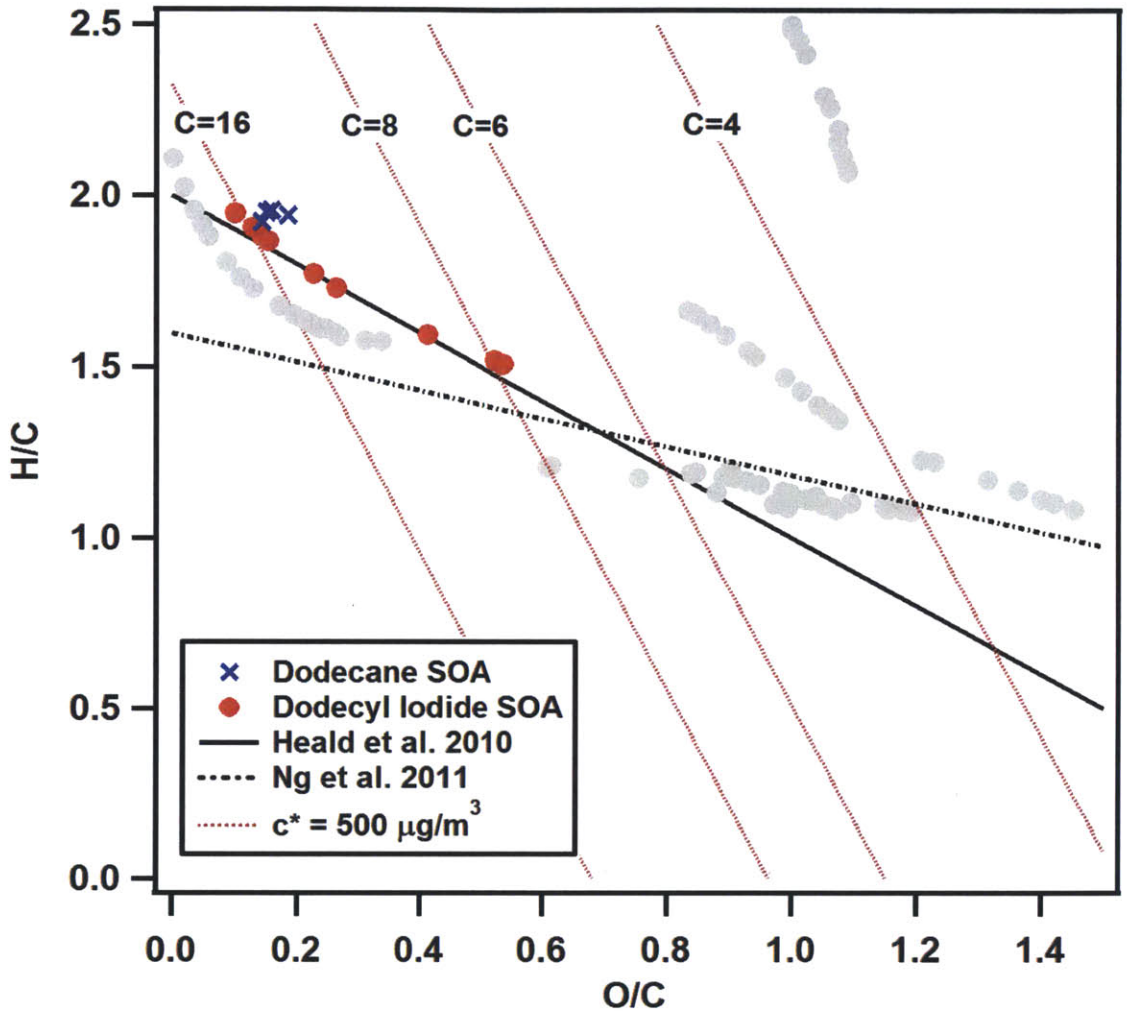

Figure 6.5: Van Krevelen plot of C_{12} photolytic SOA at increasing levels of oxidation. As exposure increases, the oxidation trajectory follows the same path as other alkanes, as well as several field observations, consistent with the equal addition of hydroxyl and carbonyl functional groups to the molecule, which are expected from RO_2 + RO_2 reactions in the condensed phase. Additionally, the degree of change of both O:C and H:C is greater than what has been observed for most other systems, even for only mild OH exposure levels, suggesting that the photolytic SOA is more readily aged.

Chapter 7

Conclusions and Outlook

This work has discussed multiple experiments in which organic aerosol particles were oxidized rapidly by interaction with gas-phase hydroxyl radicals in order to simulate the effects of several weeks' worth of chemical aging in the atmosphere. A major takeaway point has been the observation that heterogeneous oxidation—rarely included in atmospheric models—occurs on time-scales commensurate with depositional losses of particles [5], and that the resulting chemical transformation of the aerosol can have a significant effect on the physical and chemical properties of the particles, even if overall concentration does not change by a significant degree.

Chapters 5 and 6 have also demonstrated the possible experimental utility of gas-phase direct photolysis of organic compounds as a mechanism for generating secondary organic aerosol. This method provides the primary benefit of an experimental system by which oxidation chemistry can be studied directly, with a limited number of steps, in order to examine individual chemical steps that lead to the formation of SOA. The aerosol formed by this method can, as an additional benefit, be introduced to subsequent analysis techniques, such as heterogeneous oxidation or cloud condensation nucleus (CCN) counting, as an alternative to existing methods of particle generation (chamber SOA, atomization, nucleation, etc. [18, 26, 13]).

In order to tie these experiments into a broader atmospheric context, it will be necessary to examine their implications for future experiments and the information that they can provide toward making improved predictions about the atmospheric behavior of oxidized low-volatility organic species.

7.1 Experiment

One major concern of all flow-tube oxidation experiments, which combine short residence times and high oxidant concentrations in order to achieve roughly the same overall oxidant exposure as with several weeks' time spent in the atmosphere, is that any chemistry found to deviate from the second-order reaction of organic compound + OH might indicate a substantial discrepency between experimental results and environmental reality. For instance, if the initial reaction with the hydroxyl radical is not the rate-limiting step, as is typically assumed of the production of RO_2, then reactions in the flow tube will tend to under-report the apparent rates of reaction, especially as the oxidant concentration is increased to its highest levels. As a result, further experiments intended to examine identical reactions across an array of experimental apparatus are suggested. In particular, future experiments should evaluate the effects of varying the flow rate through a tube of known geometry, in addition to comparing flow tubes of differing volumes and various chambers. The efficacy of using a single "oxidant exposure" metric, calculated from the same technique across all experimental platforms, can then be evaluated, and the most atmospherically relevant parameters can be separated from the apparatus-specific parameters (including those dealing with wall loss [105] or secondary chemical effects [103]).

We have so far compared the reactivity of photolytic SOA when aged by heterogeneous oxidation by hydroxyl radicals (using dodecyl iodide as an SOA precursor) with the aging of dodecane by high concentrations of OH. However, in order to better establish the comparison between the two systems—and the observation that heterogeneous oxidation of the photolytic SOA yields more oxidized aerosol products—the experiment must be tailored more closely to a narrower interpretation of the possible causes for the discrepencies mentioned.

In particular, the possible differences between primary- and secondary-carbon alkyl radicals (with the former the dominant intermediate species for dodecyl iodide photolysis and the latter the major expected intermediate of the dodecane + OH reaction) should be examined in the context of aging, particularly since other experiments in this laboratory have demonstrated differences in aerosol yield when comparing primary and secondary radicals. Additionally, a more careful process for aging the dodecane SOA should involve removing the gas-phase components of the aerosol mixture using a charcoal denuder in order to examine the differences between the gas-phase reactions that dominate in a system at equilibrium and the heterogeneous oxidation that dominates in

a denuded mixture. Because the time scale for evaporation in the flow tube is much more than 15 times the residence time in the reactor [48, 106], we can safely assume that effectively no partitioning takes place during this time. The results of these experiments may well help to elucidate the relative importance of the two phases in the atmospheric aging that leads to OOA [57], and it may also inform the design of future photolysis experiments intended to better replicate specific aspects of SOA formation in the atmosphere or in larger chamber studies.

Additionally, we ideally want to know more about predicting aerosol properties beyond loading and elemental ratios. For that reason, an examination of the cloud-condensing nuclei (CCN) activity and refractive properties of SOA formed from gas-phase photolabile species may be useful, both for the general purpose of furthering our understanding of the physicochemical properties of organic aerosol and for an additional point of comparison between our narrow laboratory standard for SOA and actual atmospheric SOA.

7.2 Modeling

Although further experimental results are likely to provide even greater understanding of the exact nature of chemical evolution through heterogeneous oxidation, we also want to be able to make some sort of predictions about how that chemical evolution will affect the broader global picture. To that extent, we must examine current modeling practices and how these results may aid in the expansion of the predictive capabilities of state-of-the-art global transport models.

Typical models used to make predictions of atmospheric behavior of chemical species have focused either on long-range chemical transport of a limited number of species within a three-dimensional system (using programs such as GEOS-Chem [107]) or on the detailed kinetic mechanisms of a very specific set of compounds (as with the Master Chemical Mechanism, MCM [108, 109]). Additionally, recent efforts have attempted to achieve improved model efficiency by introducing random selection of species during initial self-generation of the model in question [110] and through traditional model reduction techniques [111]. These methods have had reasonable success in allowing portability of several kinetic systems to global transport models, but they remain limited by the need to generate a full description of the reactions involved

every time a new species is introduced, and the ability to accurately predict aerosol loadings and properties remains severely limited [112].

There have been several recent attempts toward remaking the framework in which aerosol formation and aging are evaluated, most notably by Donahue et al. and by Daumit et al. [74, 12]. In such an accounting, the total organic mixture is viewed, not as a sum of uncountably many individual species, but rather as a distribution of total mass (or, equivalently, of carbon mass) across a low-dimensionality range, in which properties of the aerosol components are limited to generic descriptions of the elemental composition in place of specific molecular structures. Donahue et al. propose a two-dimensional Volatility Basis Set (VBS) that uses $\overline{OS}_C$ and C^* as the dimensions of interest [22, 74], while our group suggests an alternative three-dimensional view that combines Van Krevelen space (O/C and H/C) with carbon number (n_C) to describe aerosol properties [12, 26, 27]. The former method has the advantage of using more directly measureable quantities as aerosol descriptors and of requiring a smaller number of effective "species" (i.e. bins within the two-dimensional space)—necessary for incorporation into a global three-dimensional transport model of sufficient resolution. The latter method, meanwhile, provides both greater predictive power by the inclusion of an additional chemical dimension (H/C) and also a more straightforward framework for predicting the chemical evolution of organic species (in which the average carbon oxidation state, $\overline{OS}_C$, and the vapor pressure, C^*, are treated as physical properties, which are functions of the intrinsic variables and are not themselves treated as intrinsic variables).

In order to apply the results of the analysis in this thesis to such a model framework, we must first restrict the analysis to a narrow view of those compounds with sufficiently high carbon number and degree of oxygenation (or, equivalently, sufficiently low volatility) to effectively halt gas-phase oxidation under typical ambient conditions (i.e. loadings in the range of 0.1–10μg m^{-3} and low relative humidity). The results discussed previously have demonstrated that although heterogeneous oxidation is several orders of magnitude slower than gas-phase oxidation, even for semi-volatile species, condensed-phase reactions begin to dominate as the volatility of organic species drops, while remaining competitive with other sources and sinks of OA. Thus, for models that intend to represent accurately the formation of the most highly oxygenated aspects of OA (which in turn have the largest impact on properties such as hygroscopicity and light scattering), it is necessary to choose rate parameters that correctly replicate the results of these experiments.

7.3 Atmospheric Implications

As mentioned previously, when we observe organic aerosol in the atmosphere, we wish primarily to understand the processes that lead to the concentrations (loadings) observed through particle detection techniques, in addition to the physical properties that determine how those particles interact with other atmospheric effects (e.g. water, light). In many cases, these properties tend to be dominated by the most highly oxygenated fraction of the aerosol. In this work, we have demonstrated a viable pathway by which so-called low-volatility oxygenated organic aerosol (LV-OOA) can be formed on time scales that compete with other atmospheric processes, although some question remains as to whether faster aging processes (on the order of one or two days) can similarly produce LV-OOA as observed in the field [12]. Although some models have recently had greater success at predicting organic aerosol loadings, they tend to produce inaccurate estimates of the degree of oxidation [112], such that better predictions of broader global effects, such as the impact on climate and on human health, are often precluded. As a result, assessments that aim to link the effects of climate and industrial policy to quantifiable environmental effects tend to see the largest uncertainties through aerosol-related channels [3].

More broadly, the work undertaken in this thesis aims to correct the view of the atmospheric condensed organic phase as a chemically inert mixture, as evidenced by the much heavier emphasis placed on both gas-phase [103, 65] and aqueous-phase [113] processes. Where many previous studies [7, 9, 18] have considered the reactions of organic compounds to be "finished" at the point of particle formation, this work promotes a modified view of organic aerosol not just as a reservoir for low-volatility species, but also as a reactive phase in which significant chemical transformations may occur. The evidence provided in directly comparing gas- and particle-phase aging has demonstrated that the reactions involved are sufficiently different from each other to merit the explicit modeling of the processes occuring within each phase and the interactions between them.

Bibliography

[1] Francine Laden, Joel Schwartz, Frank E Speizer, and Douglas W Dockery. Reduction in fine particulate air pollution and mortality extended follow-up of the Harvard six cities study. *American Journal of Respiratory and Critical Care Medicine*, 173(6):667–672, 2006.

[2] JL Jimenez, MR Canagaratna, NM Donahue, ASH Prevot, Qi Zhang, Jesse H Kroll, Peter F DeCarlo, James D Allan, H Coe, NL Ng, et al. Evolution of organic aerosols in the atmosphere. *Science*, 326(5959):1525–1529, 2009.

[3] Susan Solomon. *Climate change 2007—the physical science basis: Working group I contribution to the fourth assessment report of the IPCC*, volume 4. Cambridge University Press, 2007.

[4] Allen H Goldstein and Ian E Galbally. Known and unexplored organic constituents in the Earth's atmosphere. *Environmental Science & Technology*, 41(5):1514–1521, 2007.

[5] M Kanakidou, JH Seinfeld, SN Pandis, I Barnes, FJ Dentener, MC Facchini, R Van Dingenen, B Ervens, ANCJSE Nenes, CJ Nielsen, et al. Organic aerosol and global climate modelling: a review. *Atmospheric Chemistry and Physics*, 5(4):1053–1123, 2005.

[6] Qi Zhang, JL Jimenez, MR Canagaratna, JD Allan, H Coe, I Ulbrich, MR Alfarra, A Takami, AM Middlebrook, YL Sun, et al. Ubiquity and dominance of oxygenated species in organic aerosols in anthropogenically-influenced Northern Hemisphere midlatitudes. *Geophysical Research Letters*, 34(13):L13801, 2007.

[7] Colette L Heald, Daniel J Jacob, Rokjin J Park, Lynn M Russell, Barry J Huebert, John H Seinfeld, Hong Liao, and Rodney J Weber. A large organic aerosol source in the free troposphere missing from current models. *Geophysical Research Letters*, 32(18):L18809, 2005.

[8] JA De Gouw, AM Middlebrook, C Warneke, PD Goldan, WC Kuster, JM Roberts, FC Fehsenfeld, DR Worsnop, MR Canagaratna, AAP Pszenny, et al. Budget of organic carbon in a polluted atmosphere: Results from the new england air quality study in 2002. *Journal of geophysical research*, 110(D16):D16305, 2005.

[9] Rainer Volkamer, Jose L Jimenez, Federico San Martini, Katja Dzepina, Qi Zhang, Dara Salcedo, Luisa T Molina, Douglas R Worsnop, and Mario J Molina. Secondary organic aerosol formation from anthropogenic air pollution: Rapid and higher than expected. *Geophysical Research Letters*, 33(17):L17811, 2006.

[10] IM Ulbrich, MR Canagaratna, Q Zhang, DR Worsnop, and JL Jimenez. Interpretation of organic components from Positive Matrix Factorization of aerosol mass spectrometric data. *Atmos. Chem. Phys*, 9(9):2891–2918, 2009.

[11] Christopher D Cappa, Daphne L Che, Sean H Kessler, Jesse H Kroll, and Kevin R Wilson. Variations in organic aerosol optical and hygroscopic properties upon heterogeneous OH oxidation. *Journal of Geophysical Research*, 116(D15):D15204, 2011.

[12] Kelly E Daumit, Sean H Kessler, and Jesse H Kroll. Average chemical properties and potential formation pathways of highly oxidized organic aerosol. *Faraday Discussions (In Review)*, 2013.

[13] Jesse H Kroll, Jared D Smith, Dung L Che, Sean H Kessler, Douglas R Worsnop, and Kevin R Wilson. Measurement of fragmentation and functionalization pathways in the heterogeneous oxidation of oxidized organic aerosol. *Physical Chemistry Chemical Physics*, 11(36):8005–8014, 2009.

[14] JD Smith, JH Kroll, CD Cappa, DL Che, CL Liu, M Ahmed, SR Leone, DR Worsnop, and KR Wilson. The heterogeneous reaction of hydroxyl radicals with sub-micron squalane particles: a model system for understanding the oxidative aging of ambient aerosols. *Atmos. Chem. Phys*, 9(9):3209–3222, 2009.

[15] JF Pankow, WE Asher, et al. SIMPOL. 1: a simple group contribution method for predicting vapor pressures and enthalpies of vaporization of multifunctional organic compounds. *Atmospheric Chemistry and Physics*, 8(10):2773–2796, 2008.

[16] Jesse H Kroll and John H Seinfeld. Chemistry of secondary organic aerosol: Formation and evolution of low-volatility organics in the atmosphere. *Atmospheric Environment*, 42(16):3593–3624, 2008.

[17] Jay R Odum, Thorsten Hoffmann, Frank Bowman, Don Collins, Richard C Flagan, and John H Seinfeld. Gas/particle partitioning and secondary organic aerosol yields. *Environmental Science & Technology*, 30(8):2580–2585, 1996.

[18] Robert J Griffin, David R Cocker, Richard C Flagan, and John H Seinfeld. Organic aerosol formation from the oxidation of biogenic hydrocarbons. *Journal of Geophysical Research*, 104(D3):3555–3567, 1999.

[19] John H Seinfeld and James F Pankow. Organic atmospheric particulate material. *Annual Review of Physical Chemistry*, 54(1):121–140, 2003.

[20] Nga L Ng, Jesse H Kroll, Melita D Keywood, Roya Bahreini, Varuntida Varutbangkul, Richard C Flagan, John H Seinfeld, Anita Lee, and Allen H Goldstein. Contribution of first-versus second-generation products to secondary organic aerosols formed in the oxidation of biogenic hydrocarbons. *Environmental science & technology*, 40(7):2283–2297, 2006.

[21] Jesse H Kroll, Nga L Ng, Shane M Murphy, Richard C Flagan, and John H Seinfeld. Secondary organic aerosol formation from isoprene photooxidation. *Environmental science & technology*, 40(6):1869–1877, 2006.

[22] NM Donahue, AL Robinson, CO Stanier, and SN Pandis. Coupled partitioning, dilution, and chemical aging of semivolatile organics. *Environmental science & technology*, 40(8):2635–2643, 2006.

[23] IJ George, A Vlasenko, JG Slowik, K Broekhuizen, JPD Abbatt, et al. Heterogeneous oxidation of saturated organic aerosols by hydroxyl radicals: uptake kinetics, condensed-phase products, and particle size change. *Atmospheric Chemistry and Physics*, 7(16):4187–4201, 2007.

[24] AT Lambe, AT Ahern, LR Williams, JG Slowik, JPS Wong, JPD Abbatt, WH Brune, NL Ng, JP Wright, DR Croasdale, et al. Characterization of aerosol photooxidation flow reactors: heterogeneous oxidation, secondary organic aerosol formation and cloud condensation nuclei activity measurements. *Atmos. Meas. Tech*, 4(3):445–461, 2011.

[25] AT Lambe, TB Onasch, P Massoli, DR Croasdale, JP Wright, AT Ahern, LR Williams, DR Worsnop, WH Brune, and P Davidovits. Laboratory studies of the chemical composition and cloud condensation nuclei (CCN) activity of secondary organic aerosol (SOA) and oxidized primary organic aerosol (OPOA). *Atmos. Chem. Phys*, 11(17):8913–8928, 2011.

[26] Sean H Kessler, Jared D Smith, Dung L Che, Douglas R Worsnop, Kevin R Wilson, and Jesse H Kroll. Chemical sinks of organic aerosol: kinetics and products of the heterogeneous oxidation of erythritol and levoglucosan. *Environmental Sciecne & Technology*, 2010.

[27] Sean H Kessler, Theodora Nah, Kelly E Daumit, Jared D Smith, Stephen R Leone, Charles E Kolb, Douglas R Worsnop, Kevin R Wilson, and Jesse H Kroll. OH-initiated heterogeneous aging of highly oxidized organic aerosol. *The Journal of Physical Chemistry A*, 116(24):6358–6365, 2012.

[28] Peter F DeCarlo, Joel R Kimmel, Achim Trimborn, Megan J Northway, John T Jayne, Allison C Aiken, Marc Gonin, Katrin Fuhrer, Thomas Horvath, Kenneth S Docherty, et al. Field-deployable, high-resolution, time-of-flight aerosol mass spectrometer. *Analytical Chemistry*, 78(24):8281–8289, 2006.

[29] Allison C Aiken, Peter F DeCarlo, and Jose L Jimenez. Elemental analysis of organic species with electron ionization high-resolution mass spectrometry. *Analytical chemistry*, 79(21):8350–8358, 2007.

[30] Allison C Aiken, Peter F DeCarlo, Jesse H Kroll, Douglas R Worsnop, J Alex Huffman, Kenneth S Docherty, Ingrid M Ulbrich, Claudia Mohr, Joel R Kimmel, Donna Sueper, et al. O/C and OM/OC ratios of primary, secondary, and ambient organic aerosols with high-resolution time-of-flight aerosol mass spectrometry. *Environmental science & technology*, 42(12):4478–4485, 2008.

[31] MJ Northway, JT Jayne, DW Toohey, MR Canagaratna, A Trimborn, KI Akiyama, A Shimono, JL Jimenez, PF DeCarlo, KR Wilson, et al. Demonstration of a vuv lamp photoionization source for improved organic speciation in an aerosol mass spectrometer. *Aerosol Science and Technology*, 41(9):828–839, 2007.

[32] NL Ng, MR Canagaratna, JL Jimenez, Q Zhang, IM Ulbrich, and DR Worsnop. Real-time methods for estimating organic component mass

concentrations from aerosol mass spectrometer data. *Environmental science & technology*, 45(3):910–916, 2010.

[33] RYW Chang, JG Slowik, NC Shantz, A Vlasenko, J Liggio, SJ Sjostedt, WR Leaitch, and JPD Abbatt. The hygroscopicity parameter of ambient organic aerosol at a field site subject to biogenic and anthropogenic influences: relationship to degree of aerosol oxidation. *Atmos. Chem. Phys*, 10(11):5047–5064, 2010.

[34] IJ George and JPD Abbatt. Chemical evolution of secondary organic aerosol from OH-initiated heterogeneous oxidation. *Atmos. Chem. Phys*, 10(12):5551–5563, 2010.

[35] P Massoli, AT Lambe, AT Ahern, LR Williams, M Ehn, J Mikkilä, MR Canagaratna, WH Brune, TB Onasch, JT Jayne, et al. Relationship between aerosol oxidation level and hygroscopic properties of laboratory generated secondary organic aerosol (SOA) particles. *Geophysical Research Letters*, 37(24):L24801, 2010.

[36] Ari Setyan, Qi Zhang, Maik Merkel, W Berk Knighton, Yele Sun, Chen Song, John E Shilling, Timothy B Onasch, Scott C Herndon, Douglas R Worsnop, et al. Characterization of submicron particles influenced by mixed biogenic and anthropogenic emissions using high-resolution aerosol mass spectrometry: results from cares. *Atmospheric Chemistry and Physics*, 12(17):8131–8156, 2012.

[37] John D. Hearn, Lindsay H. Renbaum, Xi Wang, and Geoffrey D. Smith. Kinetics and products from reaction of Cl radicals with dioctyl sebacate (DOS) particles in O2: a model for radical-initiated oxidation of organic aerosols. *Phys. Chem. Chem. Phys.*, 9:4803–4813, 2007.

[38] Magda Claeys, Bim Graham, Gyorgy Vas, Wu Wang, Reinhilde Vermeylen, Vlada Pashynska, Jan Cafmeyer, Pascal Guyon, Meinrat O Andreae, Paulo Artaxo, et al. Formation of secondary organic aerosols through photooxidation of isoprene. *Science*, 303(5661):1173–1176, 2004.

[39] Jason D Surratt, Shane M Murphy, Jesse H Kroll, Nga L Ng, Lea Hildebrandt, Armin Sorooshian, Rafal Szmigielski, Reinhilde Vermeylen, Willy Maenhaut, Magda Claeys, et al. Chemical composition of secondary organic aerosol formed from the photooxidation of isoprene. *The Journal of Physical Chemistry A*, 110(31):9665–9690, 2006.

[40] Bernd RT Simoneit, James J Schauer, CG Nolte, Daniel R Oros, Vladimir O Elias, MP Fraser, WF Rogge, and Glen R Cass. Levoglucosan, a tracer for cellulose in biomass burning and atmospheric particles. *Atmospheric Environment*, 33(2):173–182, 1999.

[41] Christopher J Hennigan, Amy P Sullivan, Jeffrey L Collett Jr, and Allen L Robinson. Levoglucosan stability in biomass burning particles exposed to hydroxyl radicals. *Geophysical Research Letters*, 37(9):L09806, 2010.

[42] D Hoffmann, A Tilgner, Y Iinuma, and H Herrmann. Atmospheric stability of levoglucosan: A detailed laboratory and modeling study. *Environmental science & technology*, 44(2):694–699, 2009.

[43] Dirk Hoffmann, Barbara Weigert, Paolo Barzaghi, and Hartmut Herrmann. Reactivity of poly-alcohols towards OH, NO3 and SO4- in aqueous solution. *Physical Chemistry Chemical Physics*, 11(41):9351–9363, 2009.

[44] Tadeusz E Kleindienst, Mohammed Jaoui, Michael Lewandowski, John H Offenberg, Charles W Lewis, Prakash V Bhave, and Edward O Edney. Estimates of the contributions of biogenic and anthropogenic hydrocarbons to secondary organic aerosol at a southeastern US location. *Atmospheric Environment*, 41(37):8288–8300, 2007.

[45] MJ Molina, AV Ivanov, S Trakhtenberg, and LT Molina. Atmospheric evolution of organic aerosol. *Geophys. Res. Lett*, 31(22):4325–4334, 2004.

[46] TA Rissman, V Varutbangkul, JD Surratt, DO Topping, G McFiggans, RC Flagan, and JH Seinfeld. Cloud condensation nucleus (CCN) behavior of organic aerosol particles generated by atomization of water and methanol solutions. *Atmospheric Chemistry and Physics*, 7(11):2949–2971, 2007.

[47] Roy W Dixon and Gregor Baltzell. Determination of levoglucosan in atmospheric aerosols using high performance liquid chromatography with aerosol charge detection. *Journal of chromatography. A*, 1109(2):214–221, 2006.

[48] Timothy D Vaden, Dan Imre, Josef Beránek, Manish Shrivastava, and Alla Zelenyuk. Evaporation kinetics and phase of laboratory and ambient secondary organic aerosol. *Proceedings of the National Academy of Sciences*, 108(6):2190–2195, 2011.

[49] Peter F DeCarlo, Jay G Slowik, Douglas R Worsnop, Paul Davidovits, and Jose L Jimenez. Particle morphology and density characterization by combined mobility and aerodynamic diameter measurements. Part 1: Theory. *Aerosol Science and Technology*, 38(12):1185–1205, 2004.

[50] AC Aiken, D Salcedo, MJ Cubison, JA Huffman, PF DeCarlo, IM Ulbrich, KS Docherty, D Sueper, JR Kimmel, DR Worsnop, et al. Mexico City aerosol analysis during MILAGRO using high resolution aerosol mass spectrometry at the urban supersite (T0)–Part 1: Fine particle composition and organic source apportionment. *Atmos. Chem. Phys*, 9(17):6633–6653, 2009.

[51] NA Fuchs and AG Sutugin. High-dispersed aerosols. *Topics in current aerosol research*, 2:35, 1970.

[52] IJ George and JPD Abbatt. Heterogeneous oxidation of atmospheric aerosol particles by gas-phase radicals. *Nature chemistry*, 2(9):713–722, 2010.

[53] Heidi L Bethel, Roger Atkinson, and Janet Arey. Hydroxycarbonyl products of the reactions of selected diols with the OH radical. *The Journal of Physical Chemistry A*, 107(32):6200–6205, 2003.

[54] CL Heald, JH Kroll, JL Jimenez, KS Docherty, PF DeCarlo, AC Aiken, Q Chen, ST Martin, DK Farmer, and P Artaxo. A simplified description of the evolution of organic aerosol composition in the atmosphere. 2010.

[55] Maggie L Walser, Yury Desyaterik, Julia Laskin, Alexander Laskin, and Sergey A Nizkorodov. High-resolution mass spectrometric analysis of secondary organic aerosol produced by ozonation of limonene. *Physical Chemistry Chemical Physics*, 10(7):1009–1022, 2008.

[56] VF McNeill, RLN Yatavelli, JA Thornton, CB Stipe, and O Landgrebe. Heterogeneous OH oxidation of palmitic acid in single component and internally mixed aerosol particles: vaporization and the role of particle phase. *Atmos. Chem. Phys*, 8:5465–5476, 2008.

[57] Yinon Rudich, Neil M Donahue, and Thomas F Mentel. Aging of organic aerosol: Bridging the gap between laboratory and field studies. *Annu. Rev. Phys. Chem.*, 58:321–352, 2007.

[58] Jesse H Kroll, Neil M Donahue, Jose L Jimenez, Sean H Kessler, Manjula R Canagaratna, Kevin R Wilson, Katye E Altieri, Lynn R Mazzoleni, Andrew S Wozniak, Hendrik Bluhm, et al. Carbon oxidation state as a metric for describing the chemistry of atmospheric organic aerosol. *Nature Chemistry*, 3(2):133–139, 2011.

[59] CD Cappa and JL Jimenez. Quantitative estimates of the volatility of ambient organic aerosol. *Atmospheric Chemistry and Physics*, 10(12):5409–5424, 2010.

[60] JA Huffman, KS Docherty, C Mohr, MJ Cubison, IM Ulbrich, PJ Ziemann, TB Onasch, and JL Jimenez. Chemically-resolved volatility measurements of organic aerosol from different sources. *Environmental science & technology*, 43(14):5351–5357, 2009.

[61] JA Huffman, KS Docherty, AC Aiken, MJ Cubison, IM Ulbrich, PF DeCarlo, D Sueper, JT Jayne, DR Worsnop, PJ Ziemann, et al. Chemically-resolved aerosol volatility measurements from two megacity field studies. *Atmos. Chem. Phys*, 9(18):7161–7182, 2009.

[62] Jacques Buffle, France L Greter, and Werner Haerdi. Measurement of complexation properties of humic and fulvic acids in natural waters with lead and copper ion-selective electrodes. *Analytical Chemistry*, 49(2):216–222, 1977.

[63] S Fuzzi, S Decesari, MC Facchini, E Matta, M Mircea, and E Tagliavini. A simplified model of the water soluble organic component of atmospheric aerosols. *Geophys. Res. Lett*, 28(21):4079–4082, 2001.

[64] H Su, D Rose, YF Cheng, SS Gunthe, A Massling, M Stock, A Wiedensohler, MO Andreae, and U Pöschl. Hygroscopicity distribution concept for measurement data analysis and modeling of aerosol particle mixing state with regard to hygroscopic growth and CCN activation. *Atmospheric Chemistry and Physics*, 10(15):7489–7503, 2010.

[65] R Atkinson, DL Baulch, RA Cox, RF Hampson Jr, JA Kerr, MJ Rossi, and J Troe. Evaluated kinetic and photochemical data for atmospheric chemistry, organic species: Supplement VII. *Journal of Physical and chemical reference Data*, 28:191, 1999.

[66] Changgeng Peng, Man Nin Chan, and Chak K Chan. The hygroscopic properties of dicarboxylic and multifunctional acids: Measurements and

UNIFAC predictions. *Environmental science & technology*, 35(22):4495–4501, 2001.

[67] Changgeng Peng, Albert HL Chow, and Chak K Chan. Hygroscopic study of glucose, citric acid, and sorbitol using an electrodynamic balance: Comparison with UNIFAC predictions. *Aerosol Science & Technology*, 35(3):753–758, 2001.

[68] Man Yee Choi and Chak K Chan. The effects of organic species on the hygroscopic behaviors of inorganic aerosols. *Environmental science & technology*, 36(11):2422–2428, 2002.

[69] Celia N Cruz and Spyros N Pandis. Deliquescence and hygroscopic growth of mixed inorganic-organic atmospheric aerosol. *Environmental science & technology*, 34(20):4313–4319, 2000.

[70] John D Hearn and Geoffrey D Smith. Measuring rates of reaction in supercooled organic particles with implications for atmospheric aerosol. *Phys. Chem. Chem. Phys.*, 7(13):2549–2551, 2005.

[71] Lindsay H Renbaum and Geoffrey D Smith. The importance of phase in the radical-initiated oxidation of model organic aerosols: reactions of solid and liquid brassidic acid particles. *Phys. Chem. Chem. Phys.*, 11(14):2441–2451, 2009.

[72] LH Renbaum and GD Smith. Artifacts in measuring aerosol uptake kinetics: the roles of time, concentration and adsorption. *Atmospheric Chemistry and Physics*, 11(14):6881–6893, 2011.

[73] Alexander Vlasenko, Ingrid J George, and Jonathan PD Abbatt. Formation of volatile organic compounds in the heterogeneous oxidation of condensed-phase organic films by gas-phase OH. *The Journal of Physical Chemistry A*, 112(7):1552–1560, 2008.

[74] NM Donahue, SA Epstein, SN Pandis, and AL Robinson. A two-dimensional volatility basis set: 1. organic-aerosol mixing thermodynamics. *Atmos. Chem. Phys*, 11(7):3303–3318, 2011.

[75] NL Ng, MR Canagaratna, JL Jimenez, PS Chhabra, JH Seinfeld, and DR Worsnop. Changes in organic aerosol composition with aging inferred from aerosol mass spectra. *Atmospheric Chemistry and Physics*, 11(13):6465–6474, 2011.

[76] Roger Atkinson. Atmospheric chemistry of VOCs and NOx. *Atmospheric Environment*, 34(12):2063–2101, 2000.

[77] Annele Virtanen, Jorma Joutsensaari, Thomas Koop, Jonna Kannosto, Pasi Yli-Pirilä, Jani Leskinen, Jyrki M Mäkelä, Jarmo K Holopainen, Ulrich Pöschl, Markku Kulmala, et al. An amorphous solid state of biogenic secondary organic aerosol particles. *Nature*, 467(7317):824–827, 2010.

[78] G Capes, B Johnson, G McFiggans, PI Williams, J Haywood, and H Coe. Aging of biomass burning aerosols over West Africa: Aircraft measurements of chemical composition, microphysical properties, and emission ratios. *Journal of Geophysical Research*, 113(D23):D00C15, 2008.

[79] PF DeCarlo, EJ Dunlea, JR Kimmel, AC Aiken, D Sueper, J Crounse, PO Wennberg, L Emmons, Y Shinozuka, A Clarke, et al. Fast airborne aerosol size and chemistry measurements above Mexico City and Central Mexico during the MILAGRO campaign. *Atmospheric Chemistry & Physics*, 8:4027–4048, 2008.

[80] EJ Dunlea, PF DeCarlo, AC Aiken, JR Kimmel, RE Peltier, RJ Weber, J Tomlinson, DR Collins, Y Shinozuka, CS McNaughton, et al. Evolution of Asian aerosols during transpacific transport in INTEX-B. *Atmos. Chem. Phys*, 9(19):7257–7287, 2009.

[81] B Ervens, BJ Turpin, and RJ Weber. Secondary organic aerosol formation in cloud droplets and aqueous particles (aqSOA): a review of laboratory, field and model studies. *Atmos. Chem. Phys*, 11:11069–11102, 2011.

[82] N Basco, DGL James, and RD Suart. A quantitative study of alkyl radical reactions by kinetic spectroscopy. Part I. Mutual combination of methyl radicals and combination of methyl radicals with nitric oxide. *International Journal of Chemical Kinetics*, 2(3):215–234, 1970.

[83] Sidney William Benson. *Thermochemical kinetics: methods for the estimation of thermochemical data and rate parameters.* Wiley New York, 1976.

[84] Coleen M Roehl, James B Burkholder, Geert K Moortgat, AR Ravishankara, and Paul J Crutzen. Temperature dependence of UV absorption cross sections and atmospheric implications of several alkyl iodides. *Journal of geophysical research*, 102(D11):12819–12, 1997.

[85] James CM Li and Frederick D Rossini. Vapor pressures and boiling points of the l-fluoroalkanes, l-chloroalkanes, l-bromoalkanes, and l-iodoalkanes, C1 to C20. *Journal of Chemical and Engineering Data*, 6(2):268–270, 1961.

[86] Yong Bin Lim and Paul J Ziemann. Products and mechanism of secondary organic aerosol formation from reactions of n-alkanes with OH radicals in the presence of NOx. *Environmental science & technology*, 39(23):9229–9236, 2005.

[87] Allen L Robinson, Neil M Donahue, Manish K Shrivastava, Emily A Weitkamp, Amy M Sage, Andrew P Grieshop, Timothy E Lane, Jeffrey R Pierce, and Spyros N Pandis. Rethinking organic aerosols: Semivolatile emissions and photochemical aging. *Science*, 315(5816):1259–1262, 2007.

[88] Jose L Jimenez, Roya Bahreini, David R Cocker III, Hong Zhuang, Varuntida Varutbangkul, Richard C Flagan, John H Seinfeld, Colin D O'Dowd, and Thorsten Hoffmann. New particle formation from photooxidation of diiodomethane (CH2I2). *Journal of geophysical research*, 108(D10):4318, 2003.

[89] Arthur Rose, B Papahronis, and E Williams. Experimental measurement of vapor-liquid equilibria for octanol-decanol and decanol-dodecanol binaries. *Industrial & Engineering Chemistry Chemical and Engineering Data Series*, 3(2):216–219, 1958.

[90] Eric Gloaguen, Erin R Mysak, Stephen R Leone, Musahid Ahmed, and Kevin R Wilson. Investigating the chemical composition of mixed organic-inorganic particles by soft vacuum ultraviolet photoionization: The reaction of ozone with anthracene on sodium chloride particles. *International Journal of Mass Spectrometry*, 258(1):74–85, 2006.

[91] Erin R Mysak, Kevin R Wilson, Michael Jimenez-Cruz, Musahid Ahmed, and Tomas Baer. Synchrotron radiation based aerosol time-of-flight mass spectrometry for organic constituents. *Analytical chemistry*, 77(18):5953–5960, 2005.

[92] Nicholas S Shuman, Andras Bodi, and Tomas Baer. Heats of formation of t-butyl peroxy radical and t-butyl diazyl ion: RRKM vs SSACM rate theories in systems with kinetic and competitive shifts. *The Journal of Physical Chemistry A*, 114(1):232–240, 2009.

[93] Paul J Ziemann. Evidence for low-volatility diacyl peroxides as a nucleating agent and major component of aerosol formed from reactions of O3 with cyclohexene and homologous compounds. *The Journal of Physical Chemistry A*, 106(17):4390–4402, 2002.

[94] NL Ng, AJ Kwan, JD Surratt, AWH Chan, PS Chhabra, A Sorooshian, HOT Pye, JD Crounse, PO Wennberg, RC Flagan, et al. Secondary organic aerosol (SOA) formation from reaction of isoprene with nitrate radicals (NO3). *Atmospheric Chemistry and Physics*, 8(14):4117–4140, 2008.

[95] AC Noell, LS Alconcel, DJ Robichaud, M Okumura, and SP Sander. Near-infrared kinetic spectroscopy of the HO2 and C2H5O2 self-reactions and cross reactions. *The Journal of Physical Chemistry A*, 114(26):6983–6995, 2010.

[96] Herbert J Tobias and Paul J Ziemann. Kinetics of the gas-phase reactions of alcohols, aldehydes, carboxylic acids, and water with the c13 stabilized criegee intermediate formed from ozonolysis of 1-tetradecene. *The Journal of Physical Chemistry A*, 105(25):6129–6135, 2001.

[97] K Yoshino, DE Freeman, JR Esmond, and WH Parkinson. Absolute absorption cross-section measurements of ozone in the wavelength region 238–335 nm and the temperature dependence. *Planetary and space science*, 36(4):395–398, 1988.

[98] Askar Fahr, Akshaya K Nayak, and Michael J Kurylo. The ultraviolet absorption cross sections of CH3I temperature dependent gas and liquid phase measurements. *Chemical physics*, 197(2):195–203, 1995.

[99] James A Franz, Bruce A Bushaw, and Mikhail S Alnajjar. Absolute rate expressions for the abstraction of hydrogen by primary, secondary, and tertiary alkyl radicals from thiophenol. *Journal of the American Chemical Society*, 111(1):268–275, 1989.

[100] Nicholas J Kuprowicz, Jamie S Ervin, and Steven Zabarnick. Modeling the liquid-phase oxidation of hydrocarbons over a range of temperatures and dissolved oxygen concentrations with pseudo-detailed chemical kinetics. *Fuel*, 83(13):1795–1801, 2004.

[101] Jurg Eberhard, Claudia Muller, David W Stocker, and J A Kerr. Isomerization of alkoxy radicals under atmospheric conditions. *Environmental science & technology*, 29(1):232–241, 1995.

[102] Ghanshyam L Vaghjiani and AR Ravishankara. Absorption cross sections of CH3OOH, H2O2, and D2O2 vapors between 210 and 365 nm at 297 K. *Journal of Geophysical Research: Atmospheres (1984–2012)*, 94(D3):3487–3492, 1989.

[103] R Atkinson, DL Baulch, RA Cox, RF Hampson Jr, JA Kerr, MJ Rossi, and J Troe. Evaluated kinetic and photochemical data for atmospheric chemistry, organic species: Supplement V. *Journal of Physical and chemical reference Data*, 26:521, 1997.

[104] CL Lin, NK Rohatgi, and WB DeMore. Ultraviolet absorption cross sections of hydrogen peroxide. *Geophysical Research Letters*, 5(2):113–115, 1978.

[105] Peter H McMurry and Daniel Grosjean. Gas and aerosol wall losses in Teflon film smog chambers. *Environmental science & technology*, 19(12):1176–1182, 1985.

[106] Andrew P Grieshop, Neil M Donahue, and Allen L Robinson. Is the gas-particle partitioning in alpha-pinene secondary organic aerosol reversible? *Geophysical Research Letters*, 34(14), 2007.

[107] DK Henze, A Hakami, JH Seinfeld, et al. Development of the adjoint of GEOS-Chem. *Atmospheric Chemistry and Physics*, 7(9):2413–2433, 2007.

[108] SM Saunders, ME Jenkin, RG Derwent, and MJ Pilling. World Wide Web site of a Master Chemical Mechanism (MCM) for use in tropospheric chemistry models. *Atmospheric Environment*, 31(8):1249–1250, 1997.

[109] SM Saunders, ME Jenkin, RG Derwent, MJ Pilling, et al. Protocol for the development of the Master Chemical Mechanism, MCM v3 (Part A): tropospheric degradation of nonaromatic volatile organic compounds. *Atmos. Chem. Phys*, 3(1):161–180, 2003.

[110] B Aumont, S Szopa, S Madronich, et al. Modelling the evolution of organic carbon during its gas-phase tropospheric oxidation: development of an explicit model based on a self generating approach. *Atmos. Chem. Phys*, 5(9):2497–2517, 2005.

[111] S Szopa, B Aumont, S Madronich, et al. Assessment of the reduction methods used to develop chemical schemes: building of a new chemical

scheme for VOC oxidation suited to threedimensional multiscale HOx-NOx-VOC chemistry simulations. *Atmos. Chem. Phys*, 5(9):2519–2538, 2005.

[112] AP Grieshop, JM Logue, NM Donahue, and AL Robinson. Laboratory investigation of photochemical oxidation of organic aerosol from wood fires 1: measurement and simulation of organic aerosol evolution. *Atmos. Chem. Phys*, 9(4):1263–1277, 2009.

[113] John Liggio, Shao-Meng Li, and Robert McLaren. Reactive uptake of glyoxal by particulate matter. *Journal of Geophysical Research: Atmospheres (1984–2012)*, 110(D10), 2005.

Appendix A

Estimation of Volatility Properties in Van Krevelen Space

The approximate carbon number of organic aerosol can be estimated from its volatility (C^* using structure-activity relationships (SARs) for determining vapor pressure. This thesis uses SIMPOL [15], which allows for the direct determination of C^* from n_C and the functional group abundance, as described below. Chapters 3–6 focus on partitioning only into the condensed organic phase, as described by C^*. Partitioning into liquid water could also be included using this general approach, but it would require use of a SAR for estimating the volatility over water (i.e. the Henry's law constant), which is beyond the scope of this work.

Key inputs for SIMPOL (and most other SARs for estimating vapor pressures) are the abundances of different functional groups in the molecule [15]. In order to determine these from our values for n_C, H/C, and O/C, we make two assumptions. The first is that functional groups in the molecule are limited to carbonyls, hydroxyls, or some combination of the two (e.g. carboxylic acids). Since each functional group contains only one oxygen atom, their abundances can be related to the oxygen number of the molecule:

$$n_0 = \frac{O}{C} n_C = n_{\text{-OH}} + n_{=\text{O}} \tag{A.1}$$

where n_O, n_C, and O/C are as defined above, and $n_{\text{-OH}}$ and $n_{=\text{O}}$ are the number of hydroxyl groups and carbonyl groups in the molecule, respectively. While other functional groups are also likely to be present in organic aerosol,

several groups can be approximated using this simple treatment.

The second assumption is that all sites of unsaturation (double bond equivalents, DBE) in the molecule arise from carbonyl groups:

$$n_{=\mathrm{O}} = n_{\mathrm{DBE}} = 1 + n_C \left(1 - \frac{1}{2}\frac{H}{C}\right) \tag{A.2}$$

We therefore assume that our target contains no carbon-carbon double bonds or rings. While this is reasonable for C=C bonds, which are highly susceptible to oxidation and unlikely to survive significant atmospheric processing, cyclic structures may be present in highly oxidized OA. The effect of neglecting any rings present is to overestimate $n_{=\mathrm{O}}$ and underestimate $n_{\text{-OH}}$, thereby overestimating C^* somewhat.

The two assumptions above (Equations A.1 and A.2), combined with simple chemical bonding considerations, allow for the straightforward derivation of expressions relating elemental ratios, functional groups, volatility, and carbon number. The number of hydroxyl groups ($n_{\text{-OH}}$) can be determined by combining the first two equations directly:

$$\begin{aligned} n_{\text{-OH}} &= n_O - n_{=\mathrm{O}} = n_C\frac{O}{C} - \left[1 + n_C\left(1 - \frac{1}{2}\frac{H}{C}\right)\right] \\ &= -1 + n_C\left(\frac{O}{C} + \frac{1}{2}\frac{H}{C} - 1\right) \end{aligned} \tag{A.3}$$

The carbon number (n_C) and functional group abundances ($n_{\text{-OH}}$ and $n_{=\mathrm{O}}$) allow for the calculation of C^* (μg m^{-3}) using SIMPOL:

$$\begin{aligned} \log C^* &= \log(\alpha p^*) = \log\alpha + b_0 + b_C n_C + b_{=\mathrm{O}} n_{=\mathrm{O}} + b_{\text{-OH}} n_{\text{-OH}} \\ &= \log\alpha + b_0 + b_C n_C + b_{=\mathrm{O}}\left[1 + n_C\left(1 - \frac{1}{2}\frac{H}{C}\right)\right] \\ &\quad + b_{\text{-OH}}\left[-1 + n_C\left(\frac{O}{C} + \frac{1}{2}\frac{H}{C} - 1\right)\right] \end{aligned} \tag{A.4}$$

where p^* is the vapor pressure in atm, α is the conversion from p^* to $C*$, and the b_i terms are the different group contribution terms for quantifying the contribution of each chemical moiety to vapor pressure: b_0 is the zero order term, b_C is the carbon number term, $b_{=\mathrm{O}}$ is the carbonyl group term, and

$b_{\text{-OH}}$ is the hydroxyl group term, (at 293 K, equal to 1.79, -0.438, -0.935, and -2.23, respectively [15]). The conversion factor $\alpha = M_w/RT$ is 8.314×10^9 at 293 K, where M_w is the average molecular weight (g mol^{-1}) of the molecules making up the absorbing phase, R is the ideal gas constant (8.21×10^{-5} atm m^3 mol^{-1} K^{-1}), and T is the temperature in K. For these calculations we use an assumed M_w value of 200 g mol^{-1}; the actual value used has little effect on the results. Rearranging Equation A.4 to solve for carbon number, and substituting in values of $n_{\text{-OH}}$ and $n_{=\text{O}}$ from Equations A.2 and A.3, we obtain

$$n_c = \frac{\log C^* - \log \alpha - b_0 - b_{=\text{O}} + b_{\text{-OH}}}{b_C + b_{=\text{O}}\left(1 - \frac{1}{2}\frac{H}{C}\right) + b_{\text{-OH}}\left(\frac{O}{C} + \frac{1}{2}\frac{H}{C} - 1\right)} \tag{A.5}$$

Equation A.5 allows for the determination of carbon number from elemental (H/C, O/C) and volatility (C^*) data. This approach is similar to that of Donahue et al [74] for estimating carbon number from $\overline{OS}_C$ (or O/C) and C^* alone; that approach, however, required specific assumptions about functional group distribution (specifically that $n_{\text{-OH}} = n_{=\text{O}}$). With the explicit inclusion of H/C, we gain a more accurate estimation of n_C.

Appendix B

MATLAB and Igor Scripts

B.1 Evaluating Chemical Diversity of Organic Compounds

The first set of code, "oxid_calc_n_alkane.m", uses a simple combinatorial formula (with modifications for symmetrical compounds) to estimate the number of possible compounds at each value of n_c and $\overline{OS}_C$:

```
%Function(s) to determine the number of possible molecules at each
%oxidative state of a linear alkane
%
%Written by: Sean Kessler (plith@mit.edu) on 21 July 2009
%Last Modified: Never
%
%Inputs:    num_C = number of carbons in molecule
%Outputs:   ox_state = vector of possible oxidative states ((2O-H)/C)
%           num_mol = number of molecules in each ox. state
%

function [ox_state, num_mol] = oxid_calc_n_alkane(num_C)

%Sanitize; only accepts integer values of C >= 2
n = max(2,round(num_C));

%All possible oxidative states for the molecule described
ox_state = (((-2*(n+1)):2:(2*(n+1)))/n)';
```

```
%Initialize number of molecules
num_mol = zeros(length(ox_state),1);

%No acids:
num0 = oxid_calc(n,0,1,num_mol);

%Acid on one end (no longer symmetrical); one carbon less being considered
%because one carbon at the end is already spoken for
num1 = oxid_calc(n-1,1,0,num_mol);

%Diacid (symmetry back)
num2 = oxid_calc(n-2,2,1,num_mol);

%Add all possibilities together
num_mol = num0 + num1 + num2;

%Display results graphically
bar(ox_state,num_mol);
xlabel('Level of oxidation');ylabel('Number of molecules');

return;

%Function to do the actual calculations
%Written by: Sean Kessler (plith@mit.edu) on 21 July 2009
%Last Modified: Never
%
%Inputs:    n = number of carbons looked at
%           num_carboxyl = number of carboxyl groups present (for acids)
%           sym = 1 if molecule may possibly be symmetrical (not
%               possible for monoacids)
%           num_mol = blank vector for placing numbers of molecules
%Outputs:   nums = number of molecules at each oxidative state given its
%               level of acidity
%           num_excl = number of molecules excluded due to having too many
%               carbonyls in a row
%
function [nums num_excl] = oxid_calc(n,num_carboxyl,sym,num_mol)

%Initialize with zero vectors
```

```
nums = num_mol;
num_excl = num_mol;

%Two loops for the number of carbonyls and hydroxyls to be added, no more
%than the total number of sites to which they can add
for num_carbonyl = 0:n
    for num_hydroxyl = 0:(n-num_carbonyl)
        %Calculate spot in vector where calculated value will go
        oxnum = 3*num_carboxyl + 2*num_carbonyl + num_hydroxyl + 1;

        %Combination of two possibilities
        tempnum = factorial(n)/(factorial(num_carbonyl)*...
            factorial(num_hydroxyl)*...
            factorial(n-num_carbonyl-num_hydroxyl));
        %Check whether symmetrical molecules are possible
        if sym == 1
            if ((mod(num_carbonyl,2) == 0) && (mod(num_hydroxyl,2) == 0)...
                    || ((mod(n,2) == 1) && (mod(num_carbonyl+num_hydroxyl,2) == 1
                n_new = floor(n/2);
                n_h = floor(num_hydroxyl/2);
                n_c = floor(num_carbonyl/2);
                num_sym = factorial(n_new)/(factorial(n_h)*...
                    factorial(n_c)*factorial(n_new-n_c-n_h));
                tempnum = tempnum + num_sym;
            end
            %Now divide by 2 to account for double-counting
            nums(oxnum) = nums(oxnum) + (tempnum/2);
        else
            %If no symmetry possible, no double counting
            nums(oxnum) = nums(oxnum) + tempnum;
        end
    end
end
```

The second set of code, "oxid_calc_long.m", walks through all possible permutations of compounds at a given carbon length and removes instances for which the number of carbonyl groups in a row exceeds a preset maximum:

```
function [ox_state num_mol] = oxid_calc_long(C_num,carb_max)

%Sanitize; only accepts integer values of C >= 2
n = max(2,round(C_num));
%Only take carb_max >= 1
carb_max = max(1,round(carb_max));

%All possible oxidative states for the molecule described
ox_state = (((-2*(n+1)):2:(2*(n+1)))/n)';

%Initialize number of molecules
num_mol = zeros(length(ox_state),1);

%No acids:
num0 = oxid_calc(n,0,num_mol,carb_max);

%Acid on one end (no longer symmetrical); one carbon less being considered
%because one carbon at the end is already spoken for
num1 = oxid_calc(n,1,num_mol,carb_max);

%Diacid (symmetry back)
num2 = oxid_calc(n,2,num_mol,carb_max);

%Add all possibilities together
num_mol = num0 + num1 + num2;

C_nums = C_num*ones(size(num_mol));
disp(C_nums);
disp(ox_state);
disp(num_mol);

%Display results graphically
% bar(ox_state,num_mol);
% xlabel('Level of oxidation');ylabel('Number of molecules');

return;

function nums = oxid_calc(n_C,n_acid,num_mol,carb_max)

newC = n_C - n_acid;
```

```
molecule = zeros(newC);
finished = 0;

nums = num_mol;

if(newC == 0)
    finished = 1;
    if(carb_max == 1)
        nums(7) = 0;
    else
        nums(7) = 1;
    end
end

halfC = floor(newC/2);
if(n_acid >= 1)
    minval = 2;
else
    minval = 1;
end

while(finished == 0)
    num_temp = 1;
    does_break = 0;

    %Check whether symmetry is a concern; a non-symmetrical molecule is
    %worth half as much in this case, because it will be counted twice in
    %the process.
    if(n_acid ~= 1)
        for idex = 1:halfC
            if(molecule(idex) ~= molecule(newC + 1 - idex))
                num_temp = 0.5;
                break;
            end
        end
    end

    %Searching through the molecule to determine whether to add it to the
    %pile (i.e., does it have more carbonyls in a row than are permitted?)
    if((n_acid == 2))
```

```
    does_break = 1;
    for idex = 1:carb_max
        if(molecule(newC + 1 - idex) ~= 2)
            does_break = 0;
            break;
        end
    end
    if(does_break == 1)
        num_temp = 0;
    end
end
if((n_acid >= 1) && (does_break == 0))
    does_break = 1;
    for m_idex = 1:carb_max
        if(molecule(m_idex) ~= 2)
            does_break = 0;
            break;
        end
    end
    if(does_break == 1)
        num_temp = 0;
    end
end
if(does_break == 0)
    for idex = minval:(newC - carb_max)
        does_break = 1;
        for m_idex = 0:carb_max
            if(molecule(idex + m_idex) ~= 2)
                does_break = 0;
                break;
            end
        end
        if(does_break == 1)
            num_temp = 0;
            break;
        end
    end
end

nums((3*n_acid)+sum(sum(molecule))+1) = ...
```

```
        nums((3*n_acid)+sum(sum(molecule))+1) + num_temp;

    %Building the next molecule to examine
    %Search through the vector and increase Ox state of the first C atom
    %that is not already oxidized to carbonyl; all carbonyls encountered
    %along the way are reset
    for idex=1:newC
        if(molecule(idex) < 2)
            molecule(idex) = molecule(idex) + 1;
            break;
        else
            if(idex == newC)
                finished = 1;
            else
                molecule(idex) = 0;
            end
        end
    end
end

return;
```

B.2 Formation of Oxidation State Distributions from High-Resolution Mass Spectra

```
//Function to take as input a text wave describing the chemical formulas
 of the fragment ions fitted in Pika
//Outputs waves that interpret the formulae to record the number of
 C, H, and O in each fragment
Function FindCHO(formulas,prefix)
wave/z/t formulas
string prefix

variable num = numpnts(formulas)

//Make 4 new vector waves. The first three describe the number of
 C, H, and O in each fragment ion. The fourth is the
//average carbon oxidation state, given by OSc = (2*O - H)/C.
make/n=(num)/o $(prefix+"Fragment_C")
make/n=(num)/o $(prefix+"Fragment_H")
make/n=(num)/o $(prefix+"Fragment_O")
make/n=(num)/o $(prefix+"Fragment_Deg_Ox")
wave/z frag_C = $(prefix+"Fragment_C")
wave/z frag_H = $(prefix+"Fragment_H")
wave/z frag_O = $(prefix+"Fragment_O")
wave/z degox = $(prefix+"Fragment_Deg_Ox")

//Index variable, temporary storage locations for C/H/O numbers,
 and string values to help us parse the input text wave
variable idex
variable C_temp, O_temp, H_temp
string Fragment, str1, str2, str3
variable charPos, numAfterElement

for(idex = 0; idex < num; idex += 1)
C_temp = 0
O_temp = 0
H_temp = 0
Fragment = formulas[idex]
```

```
//Step 1: Parse out isotopes of C/N/O/etc. We don't care if the
 mass is different; we just want total numbers
if(strsearch(Fragment,"j",0,2) >= 0)
splitstring/E="(j|J)(\\d{1,3})([CNOS])" Fragment, str1, str2, str3
if(strsearch(str3,"C",0)>=0)
C_temp += 1
elseif(strsearch(str3,"O",0)>=0)
O_temp += 1
endif
Fragment = ReplaceString(str1+str2+str3,Fragment,"")
endif

//Step 2: How much C? (Pilfered from Elemental Analysis procedure file)
charPos = strsearch(Fragment, "C", 0)
if (charPos>=0 && !grepstring(Fragment[charPos+1], "a|u|l|r|o")  )
// changed to include o for Cobalt in 1.04A
splitstring/E="(C)(\\d{1,3})" Fragment, str1, str2
if (strlen(str2) ==0) //we do not have numbers after the letter
numAfterElement = 1
else
numAfterElement = str2num(str2)
endif
C_temp += numAfterElement
endif

//Step 3: How much O?
charPos = strsearch(Fragment, "O", 0)
if (charPos>=0)
splitstring/E="(O)(\\d{1,3})" Fragment, str1, str2
if (strlen(str2) ==0) //we do not have numbers after the letter
numAfterElement = 1
else
numAfterElement = str2num(str2)
endif
O_temp += numAfterElement
endif

//Step 4: How much H?
charPos = strsearch(Fragment, "H", 0)
if(charPos >= 0)
```

```
splitstring/E="(H)(\\d{1,3})" Fragment, str1, str2
if (strlen(str2) ==0) //we do not have numbers after the letter
numAfterElement = 1
else
numAfterElement = str2num(str2)
endif
H_temp += numAfterElement
endif

//Assign the temporary variables to the correct location in the wave.
frag_C[idex] = C_temp
frag_H[idex] = H_temp
frag_O[idex] = O_temp
degox[idex] = ((2*O_temp) - H_temp)/C_temp
endfor

End


Function GetTodoNums(todo_names,prefix)
wave/z/t todo_names
string prefix

variable numrows = numpnts(todo_names)
variable idex

make/n=(numrows)/o $(prefix+"todo_nums")
wave/z todo_nums = $(prefix+"todo_nums")

for(idex = 0; idex < numrows; idex += 1)
todo_nums[idex] = numpnts($(todo_names[idex]))
endfor

End


//Function to reduce an MxR matrix to an MxS matrix, where R is the number
 of runs (ignoring NaN columns)
// in the todo wave used to generate the Org matrix. S is the number of
 individual samples desired, with 'r' runs
```

```
// in each sample. "todo_nums" is the vector wave of the 'r' values that
 correspond to each sample, while
// "inmat" is the MxR matrix. Make sure before you start that R is equal
 to the sum of all values in todo_nums.
// Don't worry about deleting blank columns; this script will ignore
 them anyway.
Function GetAvgRuns(todo_nums,inmat,prefix)
wave/z todo_nums, inmat
string prefix

//Get the desired number of rows and columns in the output matrix
variable numrows = dimSize(inmat,0)
variable numcols = numpnts(todo_nums)

//c_idex tells us which column we're working on in the output mat.
variable c_idex

//Counter to determine where in the input matrix we are
variable counter = 0
variable t_count = 0

//Make a wave to store temporary data (summed)
make/n=(numrows)/o temp_amounts

//Matrix to store final values (averaged, rather than summed)
make/n=(numrows,numcols)/o $(prefix+"Fragment_Amounts")
wave/z amts = $(prefix+"Fragment_Amounts")

for(c_idex = 0; c_idex < numcols; c_idex += 1)
temp_amounts = 0
t_count = 0

//A while loop to keep searching until it finds the determined 'r'
 many non-NaN columns
do
//Sanity check; if the counter exceeds the dimensions of the matrix,
 we abort.
if(counter > dimSize(inmat,1))
abort "Error: End of fragment matrix reached without obtaining
 all indicated values."
```

```
endif

//Check whether we have a NaN at the top of the current column;
 if we do, we skip.
if(numType(inmat[0][counter]) == 2)

else
//If there's no NaN (i.e. the values in the column are real),
 we add it to the temp wave
t_count += 1
temp_amounts += inmat[p][counter]
endif
counter += 1
while(t_count < todo_nums[c_idex])

amts[][c_idex] = temp_amounts[p] / todo_nums[c_idex]
endfor
killwaves temp_amounts
End

//Function to take the MxS matrix from before and weight the values of
 each fragment by the
//M_per_part value (the average mass of a particle, relative to starting
 mass)
Function GetWeightedRuns(mwave,xwave,prefix)
wave/z mwave,xwave
string prefix

wave/z amt_mat = $(prefix+"Fragment_Amounts")
// display amt_mat[0][] vs xwave
duplicate/o amt_mat $(prefix+"Fragment_Norm")
wave/z norm_mat = $(prefix+"Fragment_Norm")
duplicate/o amt_mat $(prefix+"Fragment_W")
wave/z w_mat = $(prefix+"Fragment_W")

variable numrows = dimSize(amt_mat,0)
variable numcols = dimSize(amt_mat,1)
variable c_index, r_index

for(c_index = 0; c_index<numcols; c_index += 1)
```

```
norm_mat[][c_index] /= amt_mat[p][0]
w_mat[][c_index] *= mwave[c_index]/(mwave[0]*amt_mat[p][0])
endfor

display norm_mat[0][] vs xwave;
for(r_index = 1; r_index<numrows; r_index += 1)
appendtograph norm_mat[r_index][] vs xwave;
endfor

display w_mat[0][] vs xwave;
for(r_index = 1; r_index<numrows; r_index += 1)
appendtograph w_mat[r_index][] vs xwave;
endfor

End


//Function to take an M-by-S matrix and convert it to an N-by-S matrix,
 where M is the number of fragment
// ions obtained from Pika fits, and N is the number of oxidation-state
 "bins" described by the wave bin_nums.
// Make sure that all of the relevant waves have the same prefix in their
 names and suffixes that correspond to
// the lines below (i.e. if the prefix is kputsza, make sure you have
 waves called kputsza_Fragment_Deg_Ox,
// kputsza_Fragment_Amounts, and so on. If you've been using the same
 prefix in the above functions, this
// should not be a problem.
Function MakeOxHistogram(bin_nums,prefix,prefix_out,maxC)
wave/z bin_nums
variable maxC
string prefix, prefix_out

//Finds the desired waves in the current folder based on the given prefix.
wave/z ox_vals = $(prefix+"Fragment_Deg_Ox")
wave/z ion_amt = $(prefix+"Fragment_Amounts")
wave/z ion_mass = $(prefix+"Fragment_Mass")

//Index numbers, for keeping track of matrix dimensions
variable num = numpnts(bin_nums)
```

```
variable num_x = max(DimSize(ion_amt,1),1)
variable num_frags = DimSize(ion_amt,0)
variable idex,x_idex,f_idex

duplicate/o $(prefix+"Fragment_C") Cnums_temp
wave/z C_nums = Cnums_temp
if(maxC > 0)
for(f_idex = 0; f_idex < num_frags; f_idex += 1)
if(C_nums[f_idex] > maxC)
C_nums[f_idex] = 0
endif
endfor
endif

wave/z H_nums = $(prefix+"Fragment_H")
wave/z O_nums = $(prefix+"Fragment_O")

//Specifies that a bin at "0.5" will include all points greater
 than the average of 0.5 and the number
// before it and less than the average of 0.5 and the number
 following it. In other words, defines the
// width of each bin.
make/n=(num+1)/o bin_bounds
bin_bounds[0] = -10
bin_bounds[num+1] = 10
for(idex = 0; idex < (num-1); idex += 1)
bin_bounds[idex+1] = (bin_nums[idex] + bin_nums[idex+1])/2
endfor

//Make a pair of matrices, your so-called oxidation histograms.
 The first is simply mass-weighted; the latter
// is weighted by carbon number. We'll most likely be using the
 latter for most cases.
make/n=(num,num_x)/o $(prefix_out+"ox_hist")
wave/z ox_hist = $(prefix_out+"ox_hist")
make/n=(num,num_x)/o $(prefix_out+"C_hist")
wave/z C_hist = $(prefix_out+"C_hist")
//make/n=(num,num_x)/o $(prefix+"H_hist")
//wave/z H_hist = $(prefix+"H_hist")
//make/n=(num,num_x)/o $(prefix+"O_hist")
```

```
//wave/z O_hist = $(prefix+"O_hist")

//Initialize
ox_hist = 0; C_hist = 0;

//An "occurency" histogram tells us how many fragment ions
 from the given list can be found in each bin.
make/n=(num)/o $(prefix_out+"occ_hist")
wave/z occ_hist = $(prefix_out+"occ_hist")
occ_hist = 0

//A normalizing wave; temporarily stores the mass-weighted
 and C-weighted fragment distribution so we can
//later normalize each column of the output matrix so that
 it adds up to unity.
make/n=(num_frags)/o masses_at_x, C_at_x

for(x_idex = 0; x_idex < num_x; x_idex += 1)
for(idex = 0; idex < num; idex += 1)
masses_at_x = ion_amt[p][x_idex]
C_at_x = ion_amt[p][x_idex] * C_nums[p] / ion_mass[p]

for(f_idex = 0; f_idex < num_frags; f_idex += 1)
//If a fragment fits in the bin, we add it. Otherwise,
 we ignore it for now and most likely add it
// later, when we get to the proper bin.
if((ox_vals[f_idex] > bin_bounds[idex])
 && (ox_vals[f_idex] <= bin_bounds[idex+1]))
ox_hist[idex][x_idex] += ion_amt[f_idex][x_idex]
C_hist[idex][x_idex] += ion_amt[f_idex][x_idex]
 * C_nums[f_idex] / ion_mass[f_idex]
if(x_idex==0)
occ_hist[idex] += 1
endif
endif
endfor

//Normalize everything.
ox_hist[idex][x_idex] /= sum(masses_at_x)
C_hist[idex][x_idex] /= sum(C_at_x)
```

```
endfor
endfor

killwaves masses_at_x, bin_bounds

End


//Function to take an M-by-S matrix and convert it to an N-by-S
 matrix, where M is the number of fragment
// ions obtained from Pika fits, and N is the number of oxidation-
-state "bins" described by the wave bin_nums.
// Make sure that all of the relevant waves have the same prefix
 in their names and suffixes that correspond to
// the lines below (i.e. if the prefix is kputsza, make sure you
 have waves called kputsza_Fragment_Deg_Ox,
// kputsza_Fragment_Amounts, and so on. If you've been using the
 same prefix in the above functions, this
// should not be a problem.
Function MakeOxHistogramInt(prefix,prefix_out,maxC)

variable maxC
string prefix, prefix_out

//Finds the desired waves in the current folder based on the given prefix.
//wave/z ox_vals = $(prefix+"Fragment_Deg_Ox")
wave/z ion_amt = $(prefix+"Fragment_Amounts")
wave/z ion_mass = $(prefix+"Fragment_Mass")

make/n=7/o $(prefix_out+"OSc") = -3 + p
wave/z bin_nums = $(prefix_out+"OSc")

//Index numbers, for keeping track of matrix dimensions
variable num = numpnts(bin_nums)
variable num_x = max(DimSize(ion_amt,1),1)
variable num_frags = DimSize(ion_amt,0)
variable idex,x_idex,f_idex

//duplicate/o $(prefix+"Fragment_C") Cnums_temp
//wave/z C_nums = Cnums_temp
```

```
//if(maxC > 0)
// for(f_idex = 0; f_idex < num_frags; f_idex += 1)
// if(C_nums[f_idex] > maxC)
// C_nums[f_idex] = 0
// endif
// endfor
//endif

wave/z C_nums = $(prefix+"Fragment_C")
wave/z H_nums = $(prefix+"Fragment_H")
wave/z O_nums = $(prefix+"Fragment_O")


//Make a pair of matrices, your so-called oxidation histograms.
 The first is simply mass-weighted; the latter
// is weighted by carbon number. We'll most likely be using the
 latter for most cases.
make/n=(num,num_x)/o $(prefix_out+"ox_hist")
wave/z ox_hist = $(prefix_out+"ox_hist")
make/n=(num,num_x)/o $(prefix_out+"C_hist")
wave/z C_hist = $(prefix_out+"C_hist")
//make/n=(num,num_x)/o $(prefix+"H_hist")
//wave/z H_hist = $(prefix+"H_hist")
//make/n=(num,num_x)/o $(prefix+"O_hist")
//wave/z O_hist = $(prefix+"O_hist")

//Initialize
ox_hist = 0; C_hist = 0;

variable nO, nC, nH, osctemp, ntemp, dbe, pos_dbe, f_co2, idex_co2

//A normalizing wave; temporarily stores the mass-weighted
 and C-weighted fragment distribution so we can
//later normalize each column of the output matrix so that
 it adds up to unity.
make/n=(num_frags)/o masses_at_x, C_at_x
make/n=7/o normwave

for(f_idex = 0; f_idex < num_frags; f_idex += 1)
if((ion_mass[f_idex] > 43.989) && (ion_mass[f_idex] < 43.99))
```

```
idex_co2 = f_idex
break
endif
endfor

for(x_idex = 0; x_idex < num_x; x_idex += 1)
masses_at_x = ion_amt[p][x_idex]
C_at_x = ion_amt[p][x_idex] * C_nums[p] / ion_mass[p]
f_co2 = ion_amt[idex_co2][x_idex] / sum(masses_at_x)
C_hist[6][x_idex] = 5*f_co2*sum(C_at_x)

for(f_idex = 0; f_idex < num_frags; f_idex += 1)

nO = O_nums[f_idex]/0.75
nC = C_nums[f_idex]
nH = H_nums[f_idex]/0.91

if((nO*0.75) > nC)
//C_hist[6][x_idex] += ion_amt[f_idex][x_idex]
 * (nO/2) / ion_mass[f_idex]
//nC -= nO/2
//nH -= nO/2
//nO = 0
osctemp = ((2*nO) - nH)/nC
nC *= max(min((1 - (C_at_x[idex_co2]/C_at_x[f_idex])),1),0)
if(osctemp<-3)
C_hist[0][x_idex] += ion_amt[f_idex][x_idex] * nC
 / ion_mass[f_idex]
elseif(osctemp < -2)
ntemp = osctemp + 3
C_hist[1][x_idex] += ion_amt[f_idex][x_idex] * nC
 * ntemp / ion_mass[f_idex]
C_hist[0][x_idex] += ion_amt[f_idex][x_idex] * nC
 * (1 - ntemp) / ion_mass[f_idex]
elseif(osctemp < -1)
ntemp = osctemp + 2
C_hist[2][x_idex] += ion_amt[f_idex][x_idex] * nC
 * ntemp / ion_mass[f_idex]
C_hist[1][x_idex] += ion_amt[f_idex][x_idex] * nC
 * (1 - ntemp) / ion_mass[f_idex]
```

```
elseif(osctemp < 0)
ntemp = osctemp + 1
C_hist[3][x_idex] += ion_amt[f_idex][x_idex] * nC
 * ntemp / ion_mass[f_idex]
C_hist[2][x_idex] += ion_amt[f_idex][x_idex] * nC
 * (1 - ntemp) / ion_mass[f_idex]
elseif(osctemp < 1)
ntemp = osctemp
C_hist[4][x_idex] += ion_amt[f_idex][x_idex] * nC
 * ntemp / ion_mass[f_idex]
C_hist[3][x_idex] += ion_amt[f_idex][x_idex] * nC
 * (1 - ntemp) / ion_mass[f_idex]
elseif(osctemp < 2)
ntemp = osctemp - 1
C_hist[5][x_idex] += ion_amt[f_idex][x_idex] * nC
 * ntemp / ion_mass[f_idex]
C_hist[4][x_idex] += ion_amt[f_idex][x_idex] * nC
 * (1 - ntemp) / ion_mass[f_idex]
elseif(osctemp < 3)
ntemp = osctemp -2
C_hist[6][x_idex] += ion_amt[f_idex][x_idex] * nC
 * ntemp / ion_mass[f_idex]
C_hist[5][x_idex] += ion_amt[f_idex][x_idex] * nC
 * (1 - ntemp) / ion_mass[f_idex]
else
C_hist[6][x_idex] += ion_amt[f_idex][x_idex] * nC
 / ion_mass[f_idex]
endif
elseif(ion_mass[f_idex] > 30)
//nO/=0.75
//nH/=0.91
dbe = min(nO,max(0,nC + 1 - ((nH+2)/2)))
if(nO > 0)
pos_dbe = dbe/nO

if(pos_dbe < 0.5)
C_hist[3][x_idex] += ion_amt[f_idex][x_idex] * 2
 * (0.5 - pos_dbe) * nO / ion_mass[f_idex]
C_hist[4][x_idex] += ion_amt[f_idex][x_idex] * 2
 * (pos_dbe) * nO / ion_mass[f_idex]
```

```
else
C_hist[4][x_idex] += ion_amt[f_idex][x_idex] * 2
 * (1 - pos_dbe) * nO / ion_mass[f_idex]
C_hist[5][x_idex] += ion_amt[f_idex][x_idex] * 2
 * (pos_dbe - 0.5) * nO / ion_mass[f_idex]
endif
endif
nC -= nO
nH -= 2 * (nO - dbe)/0.91
nH = max(nH,0)

osctemp = -nH/nC
if(osctemp<-3)
C_hist[0][x_idex] += ion_amt[f_idex][x_idex] * nC
 / ion_mass[f_idex]
elseif(osctemp < -2)
ntemp = osctemp + 3
C_hist[1][x_idex] += ion_amt[f_idex][x_idex] * nC * ntemp
 / ion_mass[f_idex]
C_hist[0][x_idex] += ion_amt[f_idex][x_idex] * nC * (1 - ntemp)
 / ion_mass[f_idex]
elseif(osctemp < -1)
if((x_idex == 0) && nO > 0)
//print(f_idex)
//print(ion_amt[f_idex][x_idex] * nC * (1-ntemp)/ ion_mass[f_idex])
endif
ntemp = osctemp + 2
C_hist[2][x_idex] += ion_amt[f_idex][x_idex] * nC * ntemp
 / ion_mass[f_idex]
C_hist[1][x_idex] += ion_amt[f_idex][x_idex] * nC * (1 - ntemp)
 / ion_mass[f_idex]
elseif(osctemp < 0)
ntemp = osctemp + 1
C_hist[3][x_idex] += ion_amt[f_idex][x_idex] * nC * ntemp
 / ion_mass[f_idex]
C_hist[2][x_idex] += ion_amt[f_idex][x_idex] * nC * (1 - ntemp)
 / ion_mass[f_idex]
else
C_hist[3][x_idex] += ion_amt[f_idex][x_idex] * nC / ion_mass[f_idex]
endif
```

```
endif
endfor

normwave = C_hist[p][x_idex]

//Normalize everything.
//ox_hist[idex][x_idex] /= sum(masses_at_x)
C_hist[][x_idex] /= sum(normwave)
endfor

killwaves masses_at_x, C_at_x//, Cnums_temp

End
```

B.3 The Van Krevelen "Ellipse" for Elemental Ratios

The function "vk_ci.m" takes a range of O/C and H/C values and reports the mean value along with an ellipse which represents the 95% confidence region in Van Krevelen space. This ellipse is calculated from the covariance matrix of the elemental ratios.

```
function [oc_ellipse hc_ellipse] = vk_ci(oc_in,hc_in)

%%%%%%%%%%%%%%%%%%%%%%%%%%%%%%%%%%%%%%%%%%%%%%%%%%%%%%%%%%%%%%%%%%%%%%%
% Uncomment these two lines to use the "corrected" EA values %
%%%%%%%%%%%%%%%%%%%%%%%%%%%%%%%%%%%%%%%%%%%%%%%%%%%%%%%%%%%%%%%%%%%%%%%
% oc_in = 1.3*oc_in;
% hc_in = 1.1*hc_in;

%Averages
oc_av = mean(oc_in);
hc_av = mean(hc_in);

%Used to get the variance
diff_mat = [(oc_in - oc_av),(hc_in - hc_av)];
```

```
%Define the covariance matrix and scale it by 1.96 to establish the "95%
%confidence interval"
cov_mat = diff_mat'*diff_mat/(length(oc_in)-1);
cov_95_mat = (1.96^2)*cov_mat;

%Because covariance is designed to be symmetric, it Schur decomposition is
%equivalent to its eigenvalue decomposition (and the eigenvectors are at
%right angles to each other, of course!)
[Q_vk L_vk] = schur(cov_95_mat);

%The idea is that when we use the "rotated" variables as a coordinate
%system, the extremes of the confidence interval lie along the axes. It's a
%simple matter from there to rotate them into VK space with Q_vk
%The equation of the ellipse in rotated coordinates is simply
%1 = (q1^2)/L1 + (q2^2)/L2
%(See how easy it is!)
%We get the extremes of q1 by setting q2=0, then create a vector of points
%in between
%We get the corresponding values of q2 by solving the above equation
q1_half = linspace(-sqrt(L_vk(1,1)),sqrt(L_vk(1,1)),500);
q2_half = sqrt((1 - (q1_half.^2/(L_vk(1,1))))*L_vk(2,2));
%We double up the q1_half and q2_half vectors to account for the +/- sign
%that comes from solving quadratic equations
q_all = [[q1_half,-q1_half];[q2_half,-q2_half]];

%Rotating it back. We add "real()" just in case solving the equation near
%an extreme of q1 led to a rounding error and a minorly complex result
ea_all = real(Q_vk*q_all)';

%Pick out the newly rotated values (and add them to the average value,
%since they're just "differences" when computed from the covariance)
oc_ellipse = ea_all(:,1) + oc_av;
hc_ellipse = ea_all(:,2) + hc_av;

%Plot it!
figure(1)
clf reset
plot(oc_ellipse,hc_ellipse,'r-',oc_in,hc_in,'bx');
axis([0 1.2 0 2.5])
xlabel('O:C');ylabel('H:C');title('LV-OOA from many sites');
```

```
return
```

B.4 Calculation of Carbon Contours in Van Krevelen Space

The function "van_krev_plot3.m" takes a given value of n_C and C^* as inputs and in return outputs the corresponding values of $[O/C, H/C]$. The method can then be run for several different values of n_C (or of C^*) in order to create multiple contours, as in Figure 4.4.

```
function [oc_out hc_out] = van_krev_plot3(Cstar,nc)


oc_out = linspace(0,1.5,201);
hc_out = zeros(size(oc_out));

% nCH = 0;

b0 = 1.79;
b1 = -0.438;
% b5 = -0.105;
b7 = -2.23;
b9 = -0.935;

R = 0.0821e-3;  %m^3*atm/mol*K
T = 293.15;     %K
% pstar = Cstar*R*T/M;              %atm

opts = optimset('Display','off');

for ocn = 1:length(oc_out)
    o_c = oc_out(ocn);
    hcval = fsolve(@(h_c)...
        (log10(Cstar*R*T/(h_c+12+(16*o_c)))-6-log10(nc)-b0+b7-b9)/...
        (b1+(b7*((h_c/2)+o_c-1))+(b9*(1-(h_c/2)))) - nc,5,opts);
    %
```

```
    %          C = (log10(pstar)-b0+b7-b9)/...
    %              (b1+(b7*((h_c/2)+o_c-1))+(b9*(1-(h_c/2))));

    hc_out(ocn) = hcval;
end

return
```